Research & Development

2015

Mechanical Engineering Letters, Szent István University

Volume 12 (2015)
Release of

TRANS–TRIO SCIENCES
Gent •Gödöllő • Baia Mare

Contents

Dry sliding wear properties of Jute/polymer composites in high loading applications

Karthikeyan SUBRAMANIAN[1], Rajini NAGARAJAN[1],
Jacob SUKUMARAN[2], Winowlin THANGIAH[1], Patrick DE BAETS[2]

[1]Centre for Composite Materials, Department of Mechanical Engineering, Kalasalingam
University, Krishnankoil, Tamilnadu, India

[2]Department of Mechanical Construction and Production, Ghent University

Abstract

In the last few decades natural fiber composites has gained its importance due to its low cost and their availability as additives with minimal processing. Amongst the various natural sources the Jute fiber is chosen in the present research due to its fiber structure and good physical and mechanical properties. In this background natural fiber composites of unsaturated polyester were reinforced with jute fibers. While most research on green composites focuses on the structural characteristics, the present work investigates the suitability of the material to be used as a tribo-composite. Tailor made hybrid composites were made with chemically treated (NaOH) jute fiber and 2 wt % PTFE filler (tribo lubricant) to obtain the better tribological characteristics in high loading condition. Tribotests were performed on flat on flat configuration where 100Cr6 steel was used as counterface material. A pv limit of 400 MPa-mm/s (10KN and 100 mm/s) was attainedin a flat-on-flat configuration for studying the tribological properties. The static and dynamic coefficient of friction was found to be 0.15 and 0.07 respectively.An exponential increase in temperature was observed throughout the test. The material failure was observed within 500 m of sliding distance where pulverization of matrix due to thermal degradation is evident. Wear mechanisms such as fiber breakage, polymer degradation, fiber thinning and fiber separation was observed. From the present investigation the low cost Jute fabric composites havinglow frictional coefficient seemed to be a alternative to the bearing materials working at higher contact pressure and low velocity.

Keywords

Jute fiber, Taylor made hybrid composite, PTFE , NaOH treatment

1. Introduction

Customarilyall the equipment manufacturersare very often providing maintenance and replacement of moving components particularly bearings to avoid the tribologicalcatastrophe. Eventfully, it can only reduce the probability of failure

rather being eliminated thoroughly. So, the losses in terms of economic and energy [1], efficiency of equipment [2], time consumption ofmanufacturing process [3] are inevitable due to the lack of material design in tribo system. Hence, the development ofnew material system is always important to increase the life span and performance of the components.Polymeric tribo-compositeis the one which progress rapidly and find its suitability in many tribo-engineering applications due to itsinherent properties of self lubricity and resistance to impacts and shocks and anti corrosion [4, 5].

Nowadays, it is essential to compose the material withsufficient structural integrity in addition to the lubricating properties for designing the tribological components such as gears, cams, bearings and seals, etc., used in aerospace, automotive and chemical industries [6-8].In the new material design hybridization of both fibres and fillers (solid lubricants) in polymer matrix were demonstrated as a strong alternative material to be used in medium loading tribological applications [9-11]. Among various fibre orientations the weaving pattern of fabric reinforcement has shown better wear results [12, 13].Numerous works have been reported on glass [14, 15], carbon [16- 18], aramid fiber [19, 20] reinforced with differentpolymer system using various processingmethods to attain the betterment of friction and wear properties.Solid lubricants (SLs) such as poly (tetrafluoroethylene) (PTFE), graphite and molybdenum disulfide (MoS_2) were identified as a most filler in polymer matrix resulting significant reduction in friction and wear characteristics [21–23].

Recently, surface designing of composites exhibited the positive sign in the aspect of tribo-performance without appreciable compromising the strength of a composite [24]. In many of the situations, the tailor made composites have shown good sliding wear characteristics with the combination of high strength carbon fiber with PTFE, graphite and MoS_2 in various thermoplastic polymers [25-27]. However, the fabrication of these composites requires specialized chemical solvents, temperature, pressure and time consumption (curing cycle) and it extent the manufacturing process cost. At the same time, the reports on fibre reinforced tailor made composites using thermoset matrix are scanty and it also provides a scope to produce the composites with low cost hand lay-up technique.

Moreover, the reports from the World Commission on Environment & Development (U.N.) insist to develop the innovative research area of 'sustainable' or 'green' tribology, dealing with the energy conservation, ecological protection as well as significant increase in efficiency of products with quality and life.Hence, the usage of traditional man made reinforcement such as glass, carbon and aramid fibers need to be minimized with the suitable alternative posses green environmental impact. From the literature it is evident that only little published information available on the behavior of the jute fiber composite [28] as reinforcement in the degradable resin matrix system especially in the aspect of tribological application. Only few studies have been so far reported for thermoset polymer based composites and also the addition of SLs as a secondary reinforcement with jute fiber [29, 30]. However, this does not provides a full understanding of the lubricating mechanism and also the particle generation process. The present work mainly focused to develop the jute

fabric/polymer composite with polyester using cost effective hand lay-up method. The influence of Polytetrafluoroethylene (PTFE)fillers with 2 wt % of fillers on friction and wear resistance properties under dry sliding conditions was studied. Before the inclusion of tribo filler, the jute fibers was treated with NaOH alkali for the betterment of interfacial adhesion between the fiber and matrix of jute/polyester composites. To understand the effect of mechanical strength on tribological properties of composites the dry sliding wear study was carried out using heavy loading testing setup. The friction properties such as static and dynamic co-efficient of friction were studied under run in and steady state conditions. In this study though three materials will be selected for the mechanical characteristics the target material for tribological study will be chosen based on its mechanical characteristics.Hence the material with superior mechanical characteristics among the three will be tested for its tribological behavior.

2. Materials and Experiment Details

Materials used
The jute fiber in the form of bi-direction fabric was used as primary reinforcement for thermoset resin. The Polytetrafluoroethylene (PTFE) tribological filler was also used as secondary reinforcement which was obtained from Sigma Aldrich (P) Ltd, Bangalore, India. Unsaturated isophthalic polyester resin was used as resin, which was purchased from Vasivibala resins (P) Ltd, Chennai, India. For 100 grams of resin, approximately 1% of Methyl Ethyl Ketone Peroxide (MEKP) and Cobalt Naphthenate were mixed at room temperature curing.

Chemical treatment
Two different alkali chemical treatments were carried out on jute fibers to understand the interfacial adhesion between the fiber and matrix. The chemicals NaOH, calcium hydroxide powder were procured from Sigma Aldrich (P) Ltd, Bangalore, India. The untreated jute fibers were placed in a solution with 10 % NaOH concentrations. Prior to fabrication of composites, all the treated fibers were thoroughly washed with distilled water and dried in hot air oven at 80 °C for about 2 hrs.

Development of Hybrid Composite
In this work a cost effective fabrication method called hand layup technique was employed for fabricating the Taylor made jute/polyester composites. From the preliminary results the 30 weight percentage of fiber was found to be optimum fiber content which possess better mechanical properties [31]. Hence, in this work around 8 number fabric mat for the size of 200 X 150 was used for making the composites of thickness 7 mm. The hollow square of 200 X 150 mm^2 mold was prepared with the required thickness using thick asbestos sheet and it glued

over the plain aluminum sheet metal plate. At beginning, a thin layer of wax coating was provided over the aluminum plate for the easy removal of laminated plate after the fabrication of composites. Secondly, the fibers were subjected to pinned hole in such a way to facilitate the flow of matrix. Subsequently the polyester matrix was mixed with curing agent and spread over the fiber matsuntil the desired thickness is reached. Fig.1 shows the process of hand layup technique and fabricated jute/polyester composite plate within the mold cavity. In similar manner, the tailor made composites was also prepared byusing PTFE filled matrix at the surface of top layer. Finally, the compressed mold was allowed for curing at room temperature for another 24 hours. Then, the test specimens of the required size were cut from the fabricated composite plate. In the same manner, the alkali treated composites were developed by keeping the overall fiber content constant.
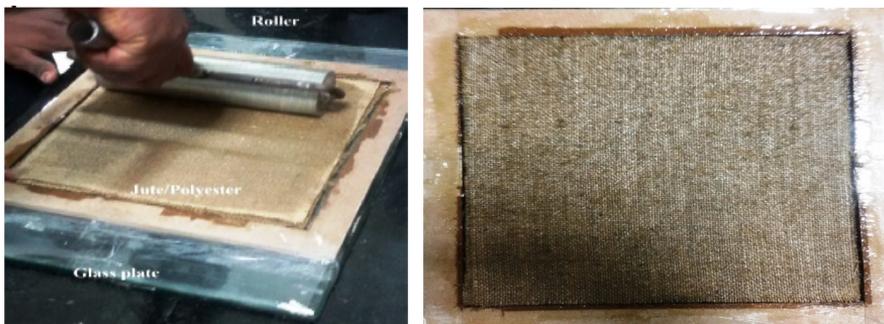
Figure 1. (a) Process of hand-layup technique (b) Jute/polyester composite laminate

Mechanical Testing
The fundamental mechanical properties such as tensile, three point bending and impact tests were performed in (Instron, Series-3382) a universal testing machine with respect to the ASTM – D 638, ASTM – D 790 and ASTM- D256 respectively. The rectangular shaped tensile specimens were prepared using a dynamic cutter machine with dimensions of 250 mm X 20 mm X 3mm. Three-point bending was carried at room temperature with the specimen size of 127 mm X 12.7 mm X 3mm. The cross head speed was selected as 5 mm/min. The Charpy-Impact test was performed to understand the impact strength of composites.

Dry sliding weartesting details
The dry sliding wear test of jute/PTFE filled polyester hybrid composites were performed using medium scale flat (MSF) testing machine, Laboratory Soete, Ghent University, Belgium. The specifications of the MSF machine was also presented in Table 1. A 100 chromium steel was used as a counter plate on both of the sides of vertical actuator. Two identical wear samples of size 50 X 50 mm^2 at 7 mm thickness as seen in Fig.2 were used on both sides of the sample

holders. A protruded length of 2 mm is the maximum allowable pre-defined thickness which can be removed in the wear testing. A k-type thermocouple was used at the rear side of the counter plate which was identified to be the place of maximum temperature accumulation.
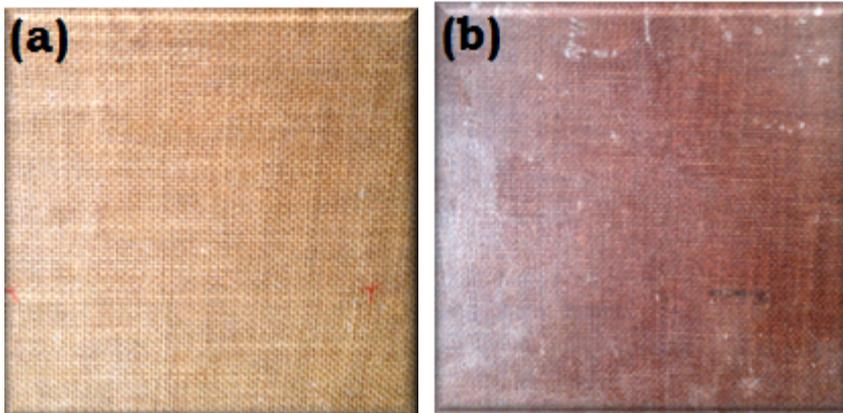
Figure 2. Contact surface of Jute/ polyester composites (a) Back side (b) Front side

The details of reinforcing fiber and filler and the matrix with the weight percentage of content are presented in Table1.

Table 1. Materials used for dry sliding wear testing

Type	Material	Content
Fiber Reinforcement	Alkali treated plain weave Jute fiber	30 wt %
Filler	PTFE ( )	2 wt %
Matrix	Unsaturated polyester	68 wt %

The addition of a filler in the form of a particulate or fibers in the matrix can offer more resistance to the wear loss of the composites. Wear tests of jute/ PTEF hybrid composites was carried out as per the tribologial testing conditions given in Table 2. The dry sliding properties such as wear, static and dynamic friction force and temperature at the counter plate were studied online. The wear data was performed at a constant load of 10kN for the NaOH treatedjute fiber /PTFE reinforced polyester hybrid composites, and it was selected based on the maximum surface area involved in the dry sliding. The counter surface disc was made of 100 chromium steel having dimensions of 200 mm length, 20 mm thick and surface roughness (Ra) of 0.1 - 0.2 μm. All the tests were conducted at ambient temperature. At least three tests with six samples of composites were subjected to the wear test and the average of the values is reported.

Table 2. Details of dry sliding wear testing conditions on MSF machine

Test Condition	Values
Stroke length	100 mm
Load	8 kN
Velocity	50 mm/ sec
Sliding distance	75 m

The data were recorded at the frequency of 500 Hz for friction force throughout the entire process. The static and dynamic coefficient were determined based on the formula used by Bonny [32] and is given in equation 1. The average value of 0.03 and 0.25 static and dynamic coefficient of friction was observed from the three repeated test with six samples.

$$F_{T,stat} = \frac{\left|F_{T,\min}\right| + \left|F_{T,\max}\right|}{2}$$

$$F_{T,dyn} = \sqrt{\frac{1}{T} \int_0^T (F_T(t))^2 \, dt}$$

3. Results and discussions

Mechanical Properties

Generally, in polymer composite the tribological characteristics mainly depends on the mechanical properties of composites [33]. Accordingly, the fundamental mechanical properties of tensile, flexural and impact strength was studied. For the fabrication of the jute fiber reinforcement was used under two different alkali treated conditions namely NaOH and CaOH2. The chemical treatment of natural fiber can remove contaminates and lead to the fibrillation process. A fibrillation is the process of separating fibril with a high aspect ratio due to the reduced diameter. This can increase the surface to contact area between the fiber and matrix and it also assist the enhancement of interfacial adhesion between the fiber and matrix. Table 3 shows the mechanical properties of untreated (UTC), alkali (ATC) and calcium hydroxide (CTC) treated jute/polyester composites. As expected, the untreated composites posses lower mechanical strength compared to chemically treated composites. Among the alkali treatment, the ATC exhibits maximum mechanical strength and it can be due to the improved interfacial adhesion between fibre and matrix. In case of CaOH2 treatment the individual fiber strength might have got reduced due to the weakening affect of fibers because of the deterioration of fibers. The maximum flexural strength of 45 MPa was observed in ATC and it shows around 45 % and 60 % of raise over the other two composites. The flexural strength is the combination of both shear and compression. The influence of compressive strength was found to be more

12

significant for getting the better tribological characteristics according to Klaus Friedrich et.al [22]. The removal of waxy layers over the fiber surface due to the alkali treatment can create the pores on surface and it facilitates the mechanical interlocking between the fiber and matrix. Hence, the possible combination of both chemical and mechanical bonding in the case of ATC serve as a crack arrester and take up more load effective stress transfer.

Table 3. Tensile, Flexural and Impact strength of untreated and treated
jute/polyester composites

Condition	Flexural Test		Tensile test			Impact Test
	Flexural Strength (MPa)	Strain (%)	Tensile Strength (MPa)	Strain (%)	Young's modulus (MPa)	Impact Strength (KJ/m^2)
UTC	15.79	13.7	25.12	2.77	1627.93	6.8
ATC	20.44	12.63	44.6	3.38	2176.82	11.38
CTC	18.6	11.56	36.72	2.79	2570.64	8.37

Tribological properties

In general, most of the physical, mechanical and tribological properties of the fiber reinforced polymer composites, depend on the interfacial adhesion between the fiber and the matrix [16,17]. And also, the tribological characteristics depend mainly on the fiber orientation, wt % of the fiber and interfacial adhesion [34-37] in fiber reinforced composites. In natural fiber reinforced composites, the presence of foreign impurities/substances that prevents the matrix from bonding firmly with the fibers, and the formation of strong a fiber/matrix interface. In the case of untreated jute fiber, this poor interfacial adhesion is the result of a waxy layer over the fibers and that leads to the poor interfacial bonding at the interface. Normally, the NaOH treatment is done for the removal of waxy layer and to create a rough surface over the fiber. It also lead to the formation of a strong interfacial bonding between the fiber and the matrix.

Knowing the superity in the mechanical characteristics of the ATC the tribologicalstudy was performed for alkali treated Jute/Polyester composite. In the aspect of achieving the better tribological characteristics into account, the tailor made composite was developed with the PTFE tribo-filler. Thereafter, the dry sliding wear test of alkali treated PTFE filled jute polyester hybrid composite was performedas per the testing conditions given in Table 2. The specific wear rate, static and dynamic friction force and temperature changes with respect to the sliding velocity of 50 mm/sec, are depicted in Figure 3. In both the cases the trend for the specific wear rate is to show a decrease with the velocity and chemical modification, respectively.

From Figure 3 it is seen that the variation of wear seems to be within the range and it shows the positive behavior of material towards wear resistance during start in condition. Similarly, static and dynamic coefficient of friction

were found to be consistent up to the distance of 65 m beyond that the up rapt changes in all the data was observed. The same was also reflected on the data of contact temperature also. But, throughout the testing conditions a continuous linear increment of temperature was noticed and it turns to up normal at nearer to the end of testing distance.
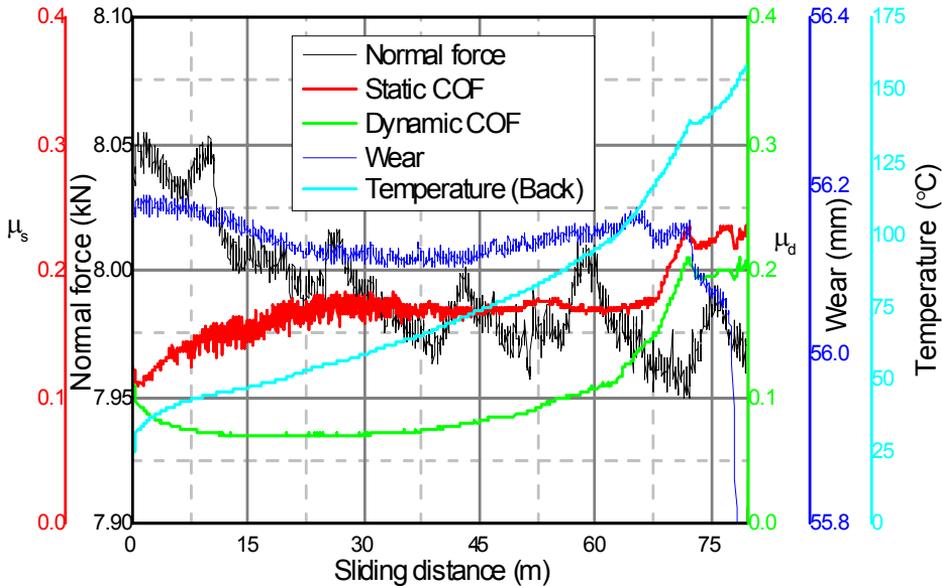
Figure 3. Tribological parameters of alkali treated jute/PTFE filled polyester hybrid composite

From Figure 3 it is seen that the variation of wear seems to be within the range and it shows the positive behavior of material towards wear resistance during start in condition. Similarly, static and dynamic coefficient of friction were found to be consistent up to the distance of 65 m beyond that the up rapt changes in all the data was observed. The same was also reflected on the data of contact temperature also. But, throughout the testing conditions a continuous linear increment of temperature was noticed and it turns to up normal at nearer to the end of testing distance.

Morphological Analysis of Worn out Surfaces
The photographs of the worn surfaces of jute/PTFE filled hybrid composites is shown in Fig.4 (a-d) with different wear failure mechanism. The images were taken using a digital camera with ring light illumination. Fig.4a. reveals that both fiber and matrix was damaged along the direction of wear track. The fiber delamination and batch of fiber separation, fiber pull out at boundaries and fiber fracture indicates the severe failure on fiber. The presence of pulverized white color debris shown in Fig.4b represents the crushed fibers. And it also highlights

14

the severe matrix failure due to thermal degradation. In Fig.4c, the separation of fibers and the thinning of fibers was also observed in the small circular patches. However, there is no crack propagation between the layers was found in the laminated composited, indicating the strong interfacial adhesion, as shown in Fig.4a.The effect, especially due to interfacial debonding, not seemed to be more pronounced for the composites, indicates the possibility of using this material in high loading condition. Moreover, the alkali treated jute fiber composites possessed a higher load-bearing capacity, which was probably due to their better stiffness and strength. From Fig. 4d, it can be seen that a fine powder was generated with combination of crushed PTFE, jute fiber and matrix. The formation of transfer layer was not observed in the worn out surface of the composites and this may be due to the lower content of PTFE filler.
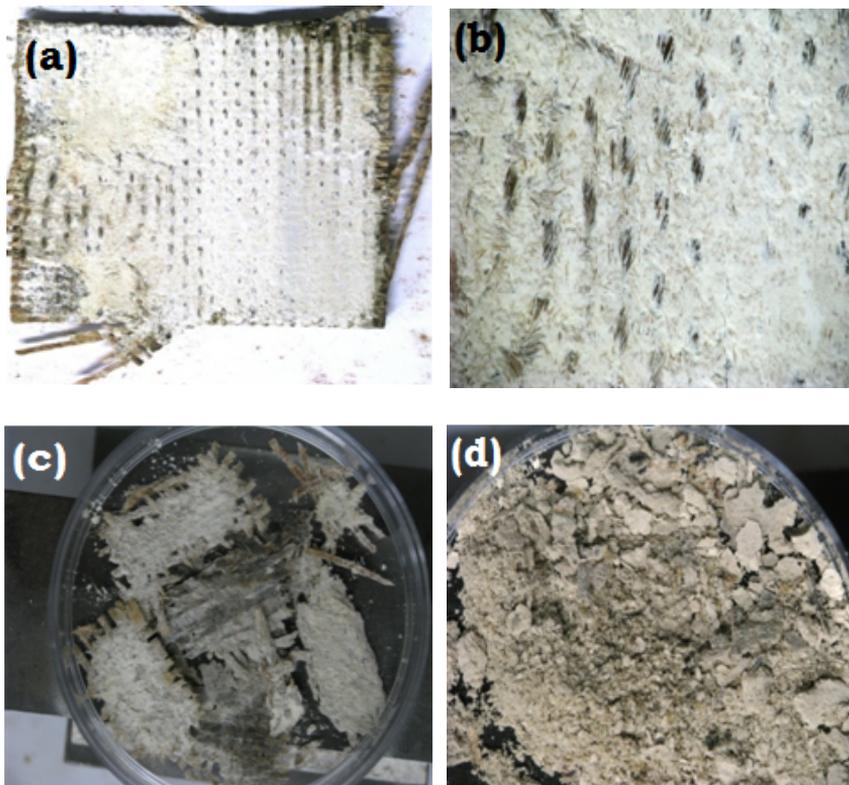
Figure 4. (a) Worn out surface of jute/polyester composite (b) Both fiber and matrix failure (c) Separated batch of fibers (d) Wear debris

Acknowledgements

Conclusions

In a first time approach the alkali treated Jute fibers reinforced composite was studied for its tribologicalproperties at lowvelocity high loading condition. A low cost method of hand layup technique was used for the successful fabrication of PTFE filled jute/polyester tailor made composites. The lower value of friction force was found up to sliding distance of 75 mm. A linear increase in temperature was observed throughout the sliding distance.Only a unsteady wear loss was noticed before the severe failure of matrix and fiber. The wear failure mechanisms like, fiber fracture, fiber thinning and wear debris due to the thermal degradation of matrix was found to be dominant just before the end of the test.

References

[1] JoakimScho¨n. Coefficient of friction of composite delamination surfaces, Wear 2000; 37:77–89.

[2] Herrington PD, Sabbaghian M. Factors affecting the friction coefficients between metallic washers and composite surfaces, Composites 1991; 22: 418–424.

[3] Zhou XH, Sun YS, Wang WS.Influences of carbon fabric/epoxy composites fabrication process on its friction and wear properties, Journal of Materials Processing Technology 2009; 209:4553–4557.

[4] S. Abarou, D. Play, Wear transition of self-lubricating composites used in dry oscillating applications, ASLE Trans. 30 (3) (1986) 269–281.

[5] P. Rehbein, J. Wallaschek, Friction and wear behavior ofpolymer/steel and alumina/alumina under high frequency fretting conditions, Wear 216 (1998) 97–105

[6] Sampathkumaran P, Seetharamu S, Murali A, Kumar RK. Dry sliding wear behavior of glass–epoxy composite. J ReinfPlast Compos 1999;18(1):55–62

[7] P. Samyn, G. Schoukens, F. Verpoort, J. Van Craenenbroeck, P. De Baets, Friction and wear mechanisms of sintered and thermoplastic polyimides under adhesive sliding, Macromolecular Materials and Engineering 292 (2007) 523–556.

[8] G. Zhao, I. Hussainova, M. Antonov, Q. Wang, T. Wang, Friction and wear of fiber reinforced polyimide composites, Wear 301 (2013) 122–129.

[9] Jacobs, O., Friedrich, K., Schulte, K.: Fretting fatigue of continuous carbon fibre reinforced polymer composites. Wear 145, 167–188 (1991).

[10] Q. Wang, Q. Xue, W. Liu, W. Shen, Tribological properties of micron silicon carbide filled poly(ether ether ketone). J. Appl. Polym. Sci., 74 (1999) 2611–2615.

[11] J. M. Durand, M.Vardavoulias, M. Jeandin, Role of reinforcing ceramic particles in the wear behavior of polymer-based model composites. Wear, 181–183 (1995) 833–839.

[12] Modi PB, Chou T, Friedrich K. Effect of testing conditions and microstructure on the sliding wear of graphite fibre /PEEK matrix composites. J Mater Sci 1988; 23:4319–30.

[13] Vishwanath B, Verma AP, Kameswara Rao CVS. Effect of reinforcement on friction and wear of fabric reinforced polymer composites. Wear 1993; 167:93– 9.

[14] M. Sumer, H. Unal, A. Mimaroglu. Evaluation of tribological behaviour of PEEK and glass fibre reinforced PEEK composite under dry sliding and water lubricated conditions, Wear 265 (2008) 1061–1065

[15] J. Bijwe and u. S. Tewari, p. Vasudevan. Friction and wear studies of a short glass-fibrereinforcedpolyetherimide composite. Wear, 132 (1989) 247 - 264 247.

[16] Zhang Z, Breidt C, Chang L, Haupert F, Friedrich K. Enhancement of the wear resistance of epoxy: short carbon fibre, graphite, PTFE and nano-TiO2. Composites Part A 2004; 35:1385–92.

[17] B.N. Ramesh a, B. Suresha. Optimization of tribological parameters in abrasive wear mode of carbon-epoxy hybrid composites. Materials and Design 59 (2014) 38–49.

[18] Z. Rasheva, G.Zhang, Th.Burkhart. A correlation between the tribological and mechanical properties of short carbon fibers reinforced PEEK materials with different fiber orientations.Tribology International 43 (2010) 1430–1437.

[19] Guijun Xia, Rolf Walter, Frank Haupert. Friction and wear of epoxy/TiO2 nanocomposites: Influence of additional short carbon fibers, Aramid and PTFE particles. Composites Science and Technology 66 (2006) 3199–3209.

[20] Ming Qiu, YanweiMiao, YingchunLi, JianjunLu. Film-forming mechanismsforself-lubricatingradialsphericalplain bearings withhybridPTFE/ aramidfabriclinersmodified byultrasonic. TribologyInternational87(2015)132–138.

[21] N. V. Klaas, K. Marcus, C. Kellock, The tribologicalbehaviour of glass filled polytetrafluoroethylene. Tribol. Int., 38 (2005) 824–833.

[22] K. Friedrich, Z. Lu, A.M. Hager. Recent advances in polymer composites tribology. Wear 190 (199.5) 139-144.

[23] Ye J,KhareHS,Burris DL. Transfer film evolution and its role in promoting ultra-low wear of a PTFE nanocomposite. Wear2013; 297(1-2):1095–102.

[24] Bijwe J, Hufenbach W, Kunze K, Langkamp A (2008) In:Friedrich K, Schlarb AK (eds) Tribology of polymeric nanocomposites. Elsevier, Amsterdam, p 483.

[25] Klaus Friedrich, Joachim Flöck, KárolyVáradi, Zoltán Néder. Experimental and numerical evaluation of the mechanical properties of compacted wear

debris layers formed between composite and steel surfaces in sliding contact. Wear 251 (2001) 1202–1212.

[26] L. Chang, Z. Zhang, Tribological properties of epoxy nanocomposites. Part II. A combinative effect of short carbon fibre with nano-TiO2. Wear, 260 (2006) 869–878.

[27] Xin-RuiZhang , Xian-Qiang Pei , Qi-Hua Wang, Friction and wear studies of polyimide composites filled with short carbon fibers and graphite and micro SiO2. Materials and Design 30 (2009) 4414–4420

[28] Reza Eslami-Farsani , S. Mohammad Reza Khalili , ZibaHedayatnasab , Neda Soleimani, Influence of thermal conditions on the tensile properties of basalt fiberreinforced polypropylene–clay nanocomposites. Materials and Design 53 (2014) 540–549.

[29] Xinrui Zhang, Xianqiang Pei and Qihua Wang, Friction and wear behavior of basalt-fabric-reinforced/solid-lubricant-filled phenolic composites, Journal of Applied Polymer Science, 117, (6), 3428–3433, 2010.

[30] BülentÖztürk, FazlıArslan and Sultan Öztürk , Hot wear properties of ceramic and basalt fiber reinforced hybrid friction materials, Tribology InternationalVol. 40, 1, 37-48 (2007)

[31] An investigation on Kerf Geometry for Abrasive Waterjet Cutting of Jute Fibre Reinforced Polyester Composite, International Journal of Applied Engineering Research, ISSN 0973-4562 Vol. 10 No.57 (2015)

[32] K. Bonny P. De Baets J. Vleugels S. Huang B. Lauwers, Dry Reciprocating Sliding Friction and Wear Response of WC–Ni Cemented Carbides, Tribol Lett (2008) 31:199–209

[33] Wetzel B, Haupert F, Friedrich K, et al. Impact and wear resistance of polymer nanocomposites at low filler content. PolymEngSci 2002; 42: 1919–1927.

[34] Tribology of natural fiber polymer composites, Karl Englund , Wood Materials and Engineering Lab, Washington State University, 2008 , Volume 12 (3).

[35] Chand N and Dwivedi UK. Influence of fiber orientation on high stress wear behavior of sisal fiber reinforced epoxy composites. Polym Compos 2008; 28:437–441.

[36] Yousif BF, Leong OB, Ong LK, et al. The effect of treatment on tribo-performance of CFRP composites. Recent Pat Mater Sci 2009; 2: 67–74.

[37] Chin CW and Yousif BF. Potential of kenaffibres as reinforcement for tribological applications. Wear 2009; 267: 1550–1557.

Abrasion test facilities – a review

Kannaki PONDICHERRY[1], Jacob SUKUMARAN[1],
Patrick DE BAETS[1], Róbert KERESZTES[2]

[1]Laboratory Soete, Department of Mechanical Construction and Production,
Ghent University Belgium
[2]Institute for Mechanical Engineering Technology, SZIE, Gödöllő

Abstract

Prediction of abrasion resistance with increased accuracy is essential to precisely estimate the operating life of a component. It has always been an intriguing challenge, as the wear results from laboratory testing and real time operations are widely mismatched, especially due to the dearth of suitable and reliable testers. There is a need to bridge this gap by developing apt testers with enhanced dependability and improved predictability. A concise review of over 100 papers was performed and testers based on the standards like ASTM G99, G132 or G65 were mostly used. The abrasion test facilities have been broadly classified into four categories based on the testing aspects viz., type of abrasion (two- / three-body), contact kinematics (sliding/rolling/reciprocating/impact), contact medium (dry/wet/slurry), and customized abrasion testers. The noteworthy observations to be mentioned are; firstly the existence of a number of standard, non-standard as well as customized testers. Secondly, only few standards prescribe the relevance of test facility to a particular end-application. Lastly, there exists a lack of clear understanding of the interdependencies between the test facilities and even if it exists, is inconclusive. The vital reflection from the study is the existence of a missing link in connecting the laboratory test parameters to the real operating conditions or vice versa. The task of development of this vital link is the fundamental foundation for the future work.

Keywords

Wear, abrasion tester, review

1. Introduction

It is a well-known fact that the most common causes for component failure are fracture, fatigue, wear and/or corrosion. Wear, among them, is a complex phenomenon to be modelled or predicted accurately (Hsu & Shen, 2005; Aronov, 1976). The complexity arises due to a plethora of factors such as e.g., material properties (composition, microstructure, hardness, yield strength, roughness), mechanical factors (load, speed, friction), operating environment (medium, temperature, humidity) making it a system-dependent phenomenon.

There are different mechanisms by which wear occur, further adding up to the complexity. A general classification of wear mechanisms include mechanical (abrasion, adhesion, flow, fatigue), chemical (corrosion) and thermal (melt or diffusive) type of wear (Kato & Adachi, 2000; Verbeek, 1979).

In any industry the abrasive wear is the most widely observed phenomenon and most rampant cause for mechanical failures. Machine components typically undergo mechanical wear among which 80- 90 % is due to abrasion, 8 % due to fatigue wear and the remaining due to the rest (Zmitrowicz, 2006). In an industrialized nation, the cost of abrasion is a significant contribution to the losses incurred, in terms of Gross Domestic Product (GDP) (ASM, 1992). Abrasive wear manifests itself in several ways: wear in abrasive processing equipments, wear of engaging machine components due to abrasive particle penetration, wear due to particle containing liquid/gaseous medium. Over the decades many laboratory scale as well as field investigations have been conducted to understand the phenomenon. However, almost all of these investigations were concentrated on studying a particular problem or application in isolation resulting in development of a range and variety of user specific abrasion test facilities. Hence an attempt has been made in the present study, to review various abrasion test facilities, their relevance and applicability in a broad perspective.

Critical assessment and applicability - abrasion testing
Most of the abrasion test facilities are designed as per the test standards. Several standards exist for wear testing viz., DIN, ASTM, JIS, ISO, etc. Test standard discusses the apparatus, test conditions, parameters, result analysis and interpretation, etc. to ensure reliability, repeatability and reproducibility of the test. However needs of every kind of tribosystem is not addressed by the standards (Blau & Budinski, 1999) which may affect the repeatability and reproducibility of such tribosystems, owing to non-standardization of test rig design guidelines, test procedure and parameters.

Most of the facilities are developed to study the effect of few parameters assuming that the effect of the remaining parameters can be cumulated. Nevertheless, the relationship between various parameters is neither simple nor established. It may also be due to the implausibility of including all the factors that affect wear in real time operating conditions into laboratory scale testing on account of; (i) wide range of parameters and (ii) cost and time of testing. The ranking of wear resistance of materials using a particular laboratory test sometimes may have little relevance during application on account of mismatch between in-service and test conditions; for example, a material showing highest wear resistance during testing may fail early during application and vice versa. The difficulty in specific test selection is further compounded by the customization of test equipments as per the individual application/test requirement over the years, which has culminated into an abundant number of test varieties without any specific guidelines for its usage. Hence it is imperative to be judicious in selection of the type of test and interpretation of test results with regard to their applicability to actual service conditions.

2. Review of test facilities

One of the earliest abrasive wear testing machines was developed by Charles Hatchett, during early 19th century (Dowson, 1979), for the purpose of investigating wear of gold coins. The first reported test facility for pin abrasion testing was reported in 1910 by Felix Robin who used a metal specimen sliding under pressure on papers covered with abrasive powder (Robin, 1910; Rosenberg, Sep 1930; Khruschov, 1974). Evolution of abrasion test facilities was largely governed by the necessity of ranking of wear resistance of materials for selection of engineering materials during system design. This led to the development of test facilities encompassing application specific abrasion conditions. The abrasion test facilities can broadly be classified based on the criterion, presented in Fig. 1.

Classification of abrasion test facilities
The abrasion test facilities have been classified into four categories based on; (i) type of abrasion, (ii) contact kinematics, (iii) contact medium, (iv) abrasive condition and (v) customized facilities. For the most common abrasion test facilities out of the categories, Table 1 enlists their salient features and area of application.
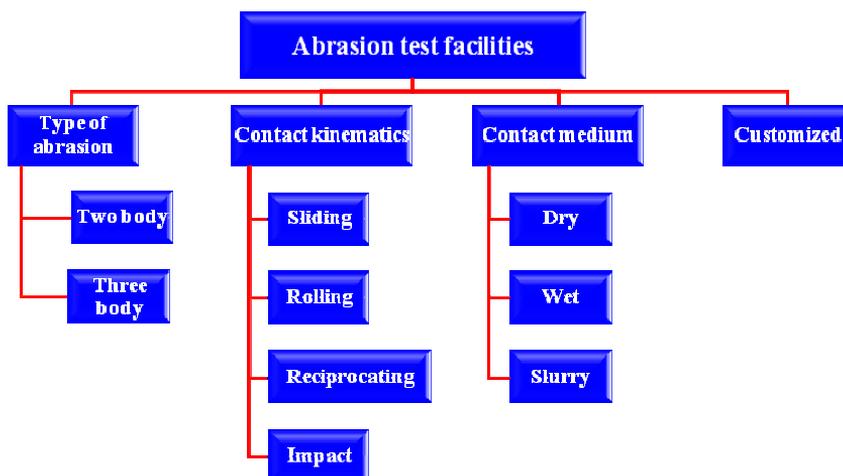
Figure1. Classification of abrasion test facilities.

Type of abrasion
Abrasive wear is defined as wear due to hard particles or hard protuberances forced against and moving along a solid surface (Bhushan, 2001). The most commonly used classification for abrasion is two-body and three-body abrasion. However, this classification of abrasive wear is not clearly defined (Gates,

1998). For the present discussion the definition of two-body abrasion would be restricted to the case where abrasive particles hitting a surface or two surfaces are in relative motion like a metal pin on an abrasive paper, as shown in **Figure (a)** and **(b)** respectively; whereas three-body abrasion is the case where an asperity between two surfaces is in relative motion, **Figure (c)**.
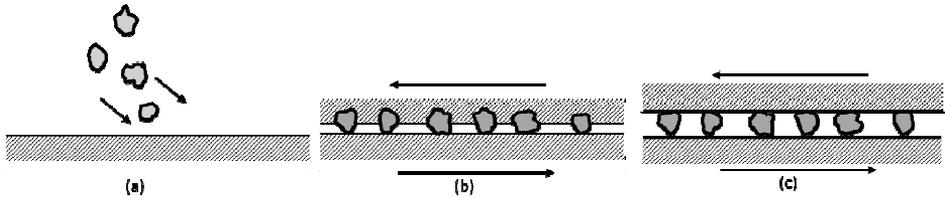

Figure 2. Types of abrasion. (a) Two-body abrasion - particles hitting a surface; (b) Two-body abrasion - two surfaces in relative motion with abrasive particles embedded on one surface; (c) Three body abrasion - asperities present between two surfaces in relative motion.

The two-body abrasion tests are the most commonly used abrasion test configurations and hence are available in plentiful of diverse designs. Most of the equipments for two-body abrasion tests (Khruschov, 1974; Larsen-Badse, 1968) are represented in either ASTM standard G 99 (pin-on-disk test) (ASTM, 2010) or G 132 (pin abrasion test) (ASTM, 2013), while few ball-on-disk type (Sexton & Fischer, 1984), and block-on-ring type (Shaw, 43) test rigs also have been reported which are included in ASTM G 99 / DIN 50324 (DIN50324, 1992) and ASTM G 77 (ASTM, 2010) standards respectively. Other two-body abrasion tester includes linearly reciprocating ball-on-flat sliding covered under ASTM G 133 standard (ASTM, 2010) and scratch hardness measurement using a diamond stylus (ASTM, 2009; Ivusic, 1981 - 1982). Still many of the adaptations reported in the literature have not been covered under any standards such as; Cross cylinder machine (Barwell, 1957 -1958), pin sliding along the thickness direction of disc (Eyre, et al., 1969), etc.

The most common and simplest method to study three-body abrasion is the dry sand rubber wheel test (DSRW test) or its adaptations (Mukhopadhyay, et al., 2014). R. D. Haworth first used the DSRW test in its present form (Jr., 1949) and which was later standardized and published under ASTM G 65 standard in 1980 (ASTM, 2010). While ASTM G 105 covers the test method for performing wet sand rubber wheel (WSRW test) abrasion tests (ASTM, 2007). In DSRW test, the load is applied to hold the specimen against the rubber wheel and the dry abrasive falls between the specimen and rubber wheel from nozzle at the top; whereas in WSRW test, the rubber wheel and specimen assembly is submerged in sand slurry container. Thus "low stress scratching abrasion" wear rates are measured where abrasive acts as a third body between the two dissimilar materials in contact. Similar to two-body abrasive testers, three-body abrasive test rigs were likewise adapted with changing requirements/applications; for

example abrasive between stationary and rotating metal specimen (Rabinowics, et al., 1961), abrasion with loose particles and no load condition (Budinski, 2011), loose abrasive particles under dead weight (Misra & Finnie, 1983), compression disc abrasive wear test (Olsson & Bay, 2009), etc.

Contact kinematics

The nature of motion during contact of two mating surfaces in relative motion can be used to classify the contact conditions during wear into four types, i.e. (i) sliding, (ii) rolling, (iii) reciprocating, and (iv) impact, (see Fig. 3). Most of the two-body abrasion configurations fall under the sliding contact category, see Fig. 2 (a), (b) and Fig. 3(a) where abrasive moves on a surface under scratching abrasion condition. In case of rolling contact kinematic condition, the abrasive rolls about its circumference while moving on a surface under an externally applied load, Fig. 3 (b). Sliding motion is the tangential motion to the contact surface whereas the other two i.e., rolling and impact are perpendicular to the surface. The severity of wear caused by sliding is much higher than that caused by rolling or impact for the same loading conditions (Bayer, 1994).
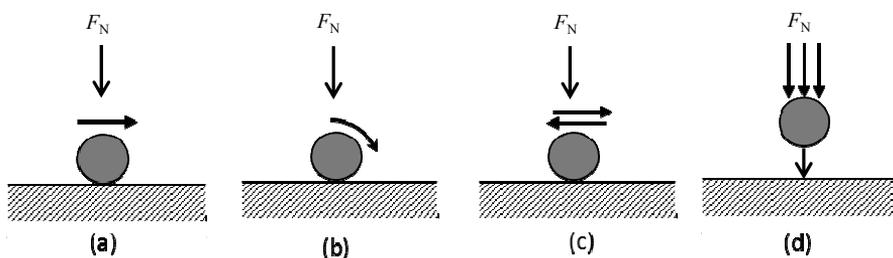
Figure 3. Different contact kinematic conditions; (a) sliding, (b) rolling, (c) reciprocating, and (d) impact.

Most of the sliding test rigs are published under ASTM G 99, 132, and 77; while its various adaptations are explained in previous section. The basic test configuration to study wear under rolling contact condition is a rolling ball-on-plate (RBOP) type test rig (Karger-Kocsis, et al., 2008). Rolling-sliding test rigs is another configuration which are in general use; such as cylindrical rolling surfaces (Gahr & Franze, 1987) or rotating twin discs forming a rectangular contact area (Lingard & Ng, 1989), either in lubricated, semi-lubricated or unlubricated condition.

Though unidirectional abrasion is the most studied phenomenon, reciprocating sliding wear damage is also observed in industrial applications. ASTM G 133 covers the linearly reciprocating sliding wear tester which is the most simplest of the configuration (Blau & Walukas, 2000). Other reciprocating test rig configuration includes rotating ring on a reciprocating flat surface (Galligan, et al., 1999), third abrasive body between the two

counter-bodies (Jones & Llewellyn, 2009), lubricated flat-on-flat sliding contacts (So & Lin, 1999), reciprocating pin-on-disk test rig with controlled atmosphere (Suh, 1973).

Impact contact kinematic conditions are present where the asperities/triboelements fall on specimen surface under the influence of their kinetic energy or an external force. In addition based on presence of sliding component during impact, which imparts the shearing action, the wear modes can be identified as *Normal impact wear* or *Compound impact wear* (in presence of sliding) (Lewis, 2007). The impact test rigs can further be categorized based on application of single or multiple asperities. Amongst the single asperity test rigs, a pivotal hammer type test rig is envisaged wherein a hinged hammer impacts a flat stationary or rotating plate to study either normal impact or compound impact respectively (Engel & Sirico, 1975). This test rig has been used to study the impact damage in soil-working agricultural tools.

One of the simplest tester configurations employing multiple asperities is paddle wear test equipment where a disc shaped paddle specimen is imparted low intensity impacts by small abrasive stones in a rotating drum (Kirchgaßner, et al., 2008). Some of the major test configurations standardized under ASTM are solid particle impingement using gas jets – ASTM G 76 (ASTM, 2013) and solid particle impingement at elevated temperature – ASTM G 211 (ASTM, 2014). The usual variations from these standards include orientation of specimen relative to the impinging stream (Islam & Farhat, 2014), high velocity impact test rigs for turbomachines (Zhong & Minemura, 1996), etc.

Contact medium
The abrasion testing facilities can similarly be classified on the basis of the abrasive contact media; (i) dry, (ii) wet and (iii) slurry. Single and multi-asperity two-body abrasion testers which includes sliding, rolling, reciprocating and impact test rigs, DSRW three-body abrasion test facilities and their respective adaptations which use abrasives in dry condition falls under the first category of this classification. Some of the industrial applications need introduction of abrasives in wet condition, e.g. Thakare et. al. (Thakare, et al., 2012) modified the ASTM G-65 test rig by feeding NaOH solution (pH: 11) along with the dry SiC abrasives in order to examine the abrasive wear performance of the WC-based hardmetals under corrosion condition. Such test rigs are classified under *Wet abrasive test rigs* category.

Many applications involve interaction of materials with abrasive slurry, e.g. oil sand and tailing carrying pipelines in offshore industry. Testing requirements and apparatus for such applications are published under ASTM G-105 (ASTM, 2007) and G-75 (ASTM, 2013), wherein the sample along with their holder and loading assemblies are submerged under slurry to investigate the slurry abrasivity. Adaptations of slurry abrasive test rigs include ball-cratering slurry abrasive tester (Stachowiak, et al., 2005), pin-on-disk slurry tester (Verspui, et al., 1995), etc.

Table 1. Most common abrasion test rigs with their attributes
and scope of application.

Test Rig	Configuration	Attributes	Scope of Application
Pin abrasion testing **(ASTM G-132)**		1 Relative motion between contacting pin of the test material and abrasive cloth / paper / plastic film 2 Possible configuration: pin-on-disk, pin-on-drum, pin-on-table, pin-on-belt 3 Test parameters: *Load, translational speed, rotational speed, track length.*	Two-body sliding abrasive wear when relative motion is caused between abrasive particles and material under varying load.
Pin-on-disk Apparatus **(ASTM G-99)**		1 Wear of a pair of materials during sliding 2 Possible configuration: pin-on-disk, ball-on-disk 3 Test parameters: *Load, sliding speed, sliding distance, temperature, atmosphere.*	Two-body sliding wear between a pair of materials when in relative motion under nominally non-abrasive condition
Block-on-ring Test **(ASTM G-77)**		1 Friction and wear testing using block and ring pair 2 Presence of lubricants, liquids or gaseous atmosphere possible for simulated testing 3 Test parameters: *Rotational speed, load.*	Two-body sliding friction and wear testing between a pair of materials when in relative motion, under simulated service conditions
Reciprocating ball-on-flat wear test **(ASTM G-133)**		1 Sliding wear testing in a linearly reciprocating ball-on-flat geometry 2 Test parameters: *Load, stroke length, frequency, type of oscillation, test duration, test temperature, lubrication, atmospheric conditions.*	Two-body sliding friction and wear testing of ceramics / metals / other wear-resistant materials, interacting in a linearly reciprocating fashion, under lubricated / unlubricated condition.
Dry sand/rubber wheel Apparatus **(ASTM G-65)**		1 Scratching abrasion testing by means of dry sand/rubber wheel 2 Test parameters: *Applicable test procedure, sand flow, lineal abrasion.*	Three-body scratching abrasion resistance of metallic materials to abrasive quartz sand
Wet sand/rubber wheel Abrasion Test **(ASTM G-105)**		Scratching abrasion resistance by means of wet sand/rubber wheel	Three-body scratching abrasion resistance of metallic materials to wet abrasive quartz sand
Slurry abrasion test **(ASTM G-75)**		Slurry abrasivity (Miller number) and slurry abrasion response of materials (SAR number) testing, using a reciprocating motion	Three-body scratching abrasion condition to test abrasivity of slurry on a standard specimen or rank abrasive response of materials in slurry
Solid particle impingement using gas jets **(ASTM G-76)**		Gas-mixed solid particle impingement on specimen, using jet-nozzle configuration erosive equiment	Two-body gas-entrained solid particle impact for ranking erosive wear resistance of materials in simulated service
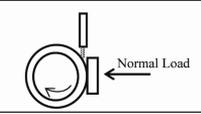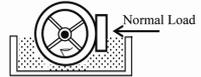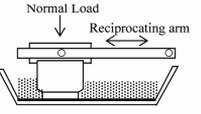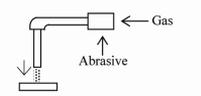
Customized test rigs

Customized wear test rigs are adaptations of the standardized and traditional test rigs with a view either to obtain very specific test outputs or to test very new wear conditions, e.g. erosion-corrosion, abrasion-corrosion. Lingard and Ng built an acoustic emission transducer coupled test rig wherein a relation could be observed

the acoustic emission and external tribological variables operative under dry sliding wear (Lingard & Ng, 1989). In a similar investigation, acoustic emission measurements were performed in a ball-on-cylinder test rig under lubricated condition (Boness & McBride, 1991). In an interesting abrasion-corrosion study, Yahagi and Mizutani redesigned a standard pin-on-disk test rig by introducing corrosive solution in contact with the abrading specimen and measured the corrosion current in order to investigate the interrelationship between corrosion and wear of carbon and austenitic stainless steels (Yahagi & Mizutani, 1986). Thus with the advent of new materials, applications and the necessity of ranking materials with regard to their wear resistance, abrasion test facilities are being continuously updated and redesigned to better serve the design engineers.

Summary

Numerous abrasion test facilities exist to cater to the needs of engineers to scrutinize behaviour of materials under abrasive conditions. The major hindrance or limitation faced by the wear test rigs is that they cannot take into consideration all possible aspects of the real time operating conditions. This drastically reduces their accuracy of prediction of wear behaviour as wear is a system dependent phenomenon. Hence even a small change in a simplest parameter of the system affects the results. Therefore, an attempt has been made to review various abrasion test facilities and classify them in order to assist the engineers in selecting a suitable test rig as per their testing requirement and further bring to notice the variability of customized test rigs, capable of even mapping material behaviour under multiple damage mechanisms.

References

[1] Aronov, V., 1976. Formation and destruction kinetics of transformed structuresof metals in frictional contact. *Wear,* Volume 310, p. 305.

[2] ASM, 1992. *ASM Metals Handbook; Friction, lubrication and wear technology.* s.l.:ASM International.

[3] ASTM, 2007. *G105 Standard test method for conducting wet sand/rubber wheel tests,* West conshohocken, PA: ASTM International.

[4] ASTM, 2009. *G171 Standard test method for scratch hardness of materials using a diamond stylus,* West conshohocken, PA: ASTM International.

[5] ASTM, 2010. *G133 Standard test method for linearly reciprocating ball-on-flat sliding wear.* West conshohocken, PA: ASTM International.

[6] ASTM, 2010. *G65 Standard test method for measuring abrasion using the dry sand/rubber wheel apparatus,* West conshohocken, PA: ASTM International.

[7] ASTM, 2010. *G77 Standard test method for ranking resistance of materials to sliding wear using block-on-ring wear test,* West conshohocken, PA: ASTM International.

[8] ASTM, 2010. *G99 Standard test method for wear testing with a pin-on-disk apparatus,* West conshohocken, PA: ASTM International.

[9] ASTM, 2013. *G132 Standard test method for pin abrasion testing,* West conshohocken, PA: ASTM International.

[10] ASTM, 2013. *G75 Standard test method for determination of slurry abrasivity (Miller number) and slurry abrasion response of materials (SAR number),* West conshohocken, PA: ASTM International.

[11] ASTM, 2013. *G76 Standard test method for conducting erosion tests by solid particle impingement using gas jets,* West conshohocken, PA: ASTM International.

[12] ASTM, 2014. *G211 Standard test method for conducting elevated temperature erosion tests by solid particle impingement using gas jets,* West conshohocken, PA: ASTM International.

[13] Barwell, F. T., 1957 -1958. Wear of metals. *Wear,* Volume 1, pp. 317 - 332.

[14] Bayer, R. G., 1994. *Fundamentals, Mechanical wear prediction and prevention.* New York: Marcel Dekker.

[15] Bhushan, B., ed., 2001. *Modern Tribology Handbook.* s.l.:CRC Press.

[16] Blau, P. J. & Budinski, K. G., 1999. Development and use of ASTM standards for wear testing. *Wear,* Volume 225-229, pp. 1159-1170.

[17] Blau, P. J. & Walukas, M., 2000. Sliding friction and wear of magnesium alloy AZ91D produced by two different methods. *Tribology Int.,* Volume 33, pp. 573-579.

[18] Boness, R. J. & McBride, S. L., 1991. Adhesive and abrasive wear studies using acoustic emission techniques. *Wear,* Volume 149, pp. 41-53.

[19] Budinski, K. G., 2011. Adhesive transfer to abrasive particles in abrasion testing. *Wear,* Volume 271, pp. 1258-1263.

[20] DIN50324, 1992. *Tribology; testing of friction and wear model test for sliding friction of solids (ball-on-disk system),* s.l.: DIN Standard.

[21] Dowson, D., 1979. *History of Tribology.* London: Longman.

[22] Engel, P. A. & Sirico, J. L., 1975. Impact wear study of lubricated contacts. *ASLE Trans.,* 18(4), pp. 279-289.

[23] Eyre, T. S., Iles, R. F. & Gasson, D. W., 1969. Wear characteristics of flake and nodular graphite cast iron. *Wear,* Volume 13, pp. 229 - 245.

[24] Gahr, K. H. Z. & Franze, H., 1987. Rolling-sliding wear on precipitation-hardened structures of an austenitic steel. *Wear,* Volume 119, pp. 261-275.

[25] Galligan, J., Torrance, A. A. & Liraut, G., 1999. A scuffing test for piston ring/bore combinations Part I. Stearic acid lubrication. *Wear,* Volume 236, pp. 199-209.

[26] Gates, J. D., 1998. Two-body and three-body abrasion: A critcal discussion. *Wear,* Volume 214, p. 139.

[27] Hsu, S. M. & Shen, M. C., 2005. Wear mapping of materials. In: G. W. Stachowiack, ed. *Wear - materials, mechanisms and practice.* Chichester, England: John Wiley & Sons Ltd, p. 369.

[28] Islam, M. A. & Farhat, Z. N., 2014. Effect of impact angle and velocity on erosion of API X42 pipeline steel under high abrasive feed rate. *Wear,* Volume 311, pp. 180-190.

[29] Ivusic, V., 1981 - 1982. Transition wear behaviour of an abrasion-resistant cast iron. *Wear,* Volume 74, pp. 307 - 314.

[30] Jones, L. & Llewellyn, R., 2009. Sliding abrasion resistance assessment of metallic materials for elevated temperature mineral processing conditions. *Wear,* Volume 267, pp. 2010 - 2017.

[31] Jr., R. D. H., 1949. The abrasion resistance of metals. *Trans. Am. Soc. Met.,* Volume 41, pp. 819-869.

[32] Karger-Kocsis, J., Felhos, D., Xu, D. & Schlarb, A. K., 2008. Unlubricated sliding and rolling wear of thermoplastic dynamic vulcanizates (Santoprene) against steel. *Wear,* Volume 265, pp. 292-300.

[33] Kato, K. & Adachi, K., 2000. Wear Mechanisms. In: B. Bhushan, ed. *Modern Tribology Handbook.* s.l.:CRC Press.

[34] Khruschov, M. M., 1974. Principles of abrasive wear. *Wear,* Volume 28, p. 69.

[35] Kirchgaßner, M., Badisch, E. & Franek, F., 2008. Behaviour of iron-based hardfacing alloys under abrasion and impact. *Wear,* Volume 265, pp. 772-779.

[36] Larsen-Badse, J., 1968. Influence of grit diameter and specimen size on wear during sliding abrasion. *Wear,* Volume 12, pp. 35-53.

[37] Lewis, R., 2007. A modelling technique for predicting compound impact wear. *Wear,* Volume 262, pp. 1516-1521.

[38] Lingard, S. & Ng, K. K., 1989. An investigation of acoustic emission in sliding friction and wear of metals. *Wear,* Volume 130, pp. 367-379.

[39] Misra, A. & Finnie, I., 1983. An experimental study of three-body abrasive wear. *Wear,* Volume 85, pp. 57 - 68.

[40] Mukhopadhyay, P., Kannaki, P. S., Srinivas, M. & Roy, M., 2014. Microstructural developments during abrasion of M50 bearing steel. *Wear,* Volume 315, pp. 31-37.

[41] Olsson, D. D. & Bay, N., 2009. *Simulative wear testing of tool materials for communion of hard ore material: Friction, Wear and Wear Protection.* Weinheim: Wiley-VCH.

[42] Rabinowics, E., Dunn, L. A. & Russel, P. G., 1961. A study of abrasive wear under three-body conditions. *Wear,* Volume 4, pp. 345 - 355.

[43] Robin, F., 1910. The wear of steels with abrasives. *Carnegie Scholarship Memoirs, Iron & Steel Inst., 2*, p. 6.

[44] Rosenberg, S. J., Sep 1930. The resistance of steels to abrasion by sand. *Bureau of Standards J of Research,* 5(3), pp. 553-574.

[45] Sexton, M. D. & Fischer, T. E., 1984. The mild wear of 52100 steel. *Wear,* Volume 96, pp. 17-30.

[46] Shaw, M. C., 43. Dimensional analysis for wear systems. *Wear,* Volume 43, pp. 263 - 266.

[47] So, H. & Lin, R. C., 1999. The combined effects of ZDDP, surface texture and hardness on the running-in of ferrous metals. *Tribology Int.,* Volume 32, pp. 243-253.

[48] Stachowiak, G., Stachowiak, G. & Celliers, O., 2005. Ball-cratering abrasion tests of high-Cr white cast irons. *Tribology International,* Volume 38, pp. 1076 - 1087.

[49] Suh, N. P., 1973. The delamination theory of wear. *Wear,* Volume 25, pp. 111-124.

[50] Thakare, M. R., J. A. Wharton, R. J. K. W. & Menger, C., 2012. Effect of abrasive particle size and the influence of microstructure on the wear mechanisms in wear-resistant materials. *Wear,* Volume 276 - 277, pp. 16 - 28.

[51] Verbeek, H. J., 1979. Tribological systems and wear factors. *Wear,* Volume 56, pp. 81-92.

[52] Verspui, M. A., With, G. d., Varst, P. G. T. v. d. & Buijs, M., 1995. Bed thickness and particle size distribution in three-body abrasion. *Wear,* Volume 188, pp. 102-107.

[53] Yahagi, Y. & Mizutani, Y., 1986. Corrosive wear of carbon and austenitic stainless steels in NaCl solution. *Wear,* Volume 110, pp. 401-408.

[54] Zhong, Y. & Minemura, K., 1996. Measurement of erosion due to particle impingement and numerical prediction of wear in pump casing. *Wear,* Volume 199, pp. 36-44.

[55] Zmitrowicz, A., 2006. Wear patterns and laws of wear - A review. *Journal of Theoretical and Applied Mechanics,* 44(2), p. 219.

The transitory regime of the electromechanical actuators in the modern industrial systems

Vasile NĂSUI, Radu COTEȚIU, Adriana COTEȚIU

Department of Engineering and Management Technologies
Technical University of Cluj-Napoca, North Univ. Center of Baia Mare,
Faculty of Engineering

Abstract

In our present paper we are going to show a few aspects concerning the transitory regime of functioning of electro mechanic actuators which has a heavy impact in their usage within the modern systems of pre-working or different process industries, within this contest new acting solutions referring to components and working parameters in difficult conditions. This paper aims at revising the main constructive characteristics in order to improve the functionality under the energetic and the dynamic aspect.

Keywords

Electro-mechanical linear actuator, virtual simulation, transitory regime, energetic efficiency

1. Introduction

Lately almost in all the technological processes and in the industrial production based on machine construction the issue of a high economic efficiency has always been raised. By studying critically the evolution of the actuators mechanism we notice the evolution directions of the improvements.

The taking into account that this negative effect of the insertion forces is higher, being in direct relationship of the increased functioning speeds of the actuators. In this context, the introduction of the electro mechanic actuators can be achieved only in the case of superior performances which have been achieved lately due to new solutions of actuator mechanism [1].

The main problem for the conceiving optimal transmissions that should lead to well performing machines and equipment which have an essential contribution to the achievement of qualitative constructive and functional parameters, including also the energetic efficiency.

The period of functioning, the high efficiency, the large regulating range of the movement parameters, the functioning security, the compact constructive simplicity, the high accuracy of positioning are closely together etc.. An actuator's function is to provide thrust and positioning in machines used for

production or testing. One type is the electromechanical actuator, which converts the torque of an electric rotary motor into linear mechanical thrust. The technical system of the linear actuator perfected through this method has a few basic characteristics expressed by particular indicators such as*: adjustable acting, high precision and efficiency portent capacity, a rank of high speeds, numerical control* etc. Although the actuators have a great functional and constructive variety, in general they must have the following characteristics: basic structure which consists of electric motor, drive mechanism for converting the rotary motion into a translation motion and its control system [3].

A new innovative and original structure of a type of linear actuator is presented in the Figure 1. In this structure the extension and the conversion of the energy are accompanied by the conversion of some informative signals. This offers the best solution to linear actions owing to the large flexibility, to the high efficiency, to the cinematic, dynamic and high precision capabilities [5] [7].

2. Mathematical Modeling of the Linear Actuator Dynamics

The optimum for the actuators is done starting from the auctioning time analysis, the imposed technological requirements [4].
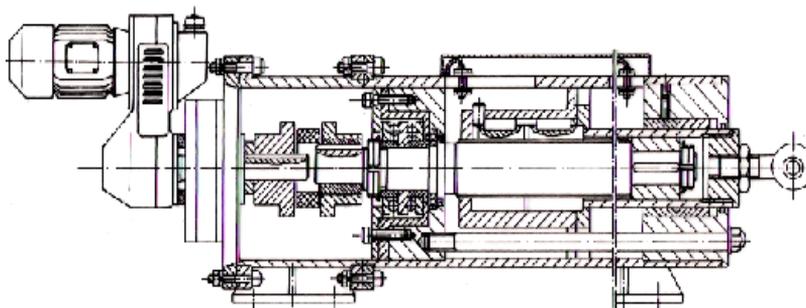
Figure 1. Units with rotating variator with broad belts

Once these parameters are established, it will be set the priorities, after that follows the synthesis of the mechanism of movement transformation.

In this synthesis, the input data are the above mentioned parameters and the output data are: *the dimension of the components, their dynamic behavior, the distribution of masses* etc.

The main dynamic criteria for the optimization of the mechanism of movement transformations, which are useful in assessing of the quality of the functioning of the actuator mechanism in working regime, are: *the mechanics average efficiency, the losses in kinematic couples, the multiplication coefficient of force, the non-uniformity of the working coefficient, the static and dynamic losses of balance* [5].

– The losses in kinematics couples, which represents the report between the instantaneous power of the friction forces in the kinematic couples (P_f) and the appropriate power of engine forces (P_m):

$$\psi = \frac{P_f}{P_m} \tag{1}$$

– The multiplication coefficient of the force is:

$$\xi = \frac{F_f}{F_m} \tag{2}$$

– The engine force F_c which acts upon the element led as a useful or technological resistance force.

By replacing within the relationship with the expressions of the power P_f and P_m and the velocities V_e and V_m will obtain:

$$\xi = \frac{1}{\eta} \cdot \frac{1}{i_{1n}} \tag{3}$$

– The average coefficient of the non-uniformity of the working is:

$$\delta = \frac{\Delta L_{max}}{J_{red}\omega^2_{med}} \tag{4}$$

where:

ω_{med} – is the average value of the speed.

– - The excedentary mechanic working L_{max} is:

$$\Delta L_{max} = \frac{1}{2}J_{red}\left(\omega^2_{max} - \omega^2_{min}\right) \tag{5}$$

The mathematical model belonging to the dynamic behavior of the actuator can be expressed as a differential equation of the movement, of some transfer functions or some frequency characteristics. The characteristics traced on the analysis of the dynamic behavior include: *index of velocity, acceleration and space, frequency characteristics etc*.

After the achievement of the mathematical model, the analysis of the dynamic behavior follows with the establishment of the major influence of the functional constructive parameters on the general characteristic parameters as well as the performances of the actuators. Digital simulation is required in order to determine the priority module where the functional - constructive parameters influence the parameters and the performances of the dynamic behavior.

The projection of those transmissions has to fulfill the stability requests, precision, transitory answer etc. resorting to a compromise between the accepted measure of the deviation, stationary and the desired degree of dynamic stability. The control of these parameters is done by "correction" using a net with appropriate configuration of parallel type, introduced in the reaction loop of the servo-system. Using this method of control of the movement leads frequently to multiple to loop systems, used especially for the electro mechanic actuators where the input signal is of alternative power.

The most used block scheme of a servo-system of control with the transfer functions of the composing elements for the electro mechanic actuator with position reaction and speed is presented in Figure 2.
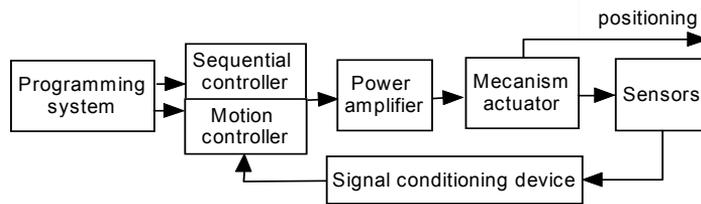

Figure 2. The structural mathematical model for actuators

For the transitory regimes of functioning, the efficiency can be calculate the two components of the moment of losses within the transmission according to the relation (6) including the dynamic moment. According to Newton's when the load S is coupled to the engine which leads by means of a gear mechanism, by combining and grouping the equations results the equations which describe the system:

$$J_{echiv.} \frac{d^2\theta_i}{dt^2} + B_{echiv.} \frac{d\theta_i}{dt} + k_{echiv.}\theta_i + M_s / i_r = M \qquad (6)$$

This equation shows the performances of the system as a function of a single variant, the input angle - θ.

An equivalent system is the one that has the inertia moment equivalent, damping and equivalent rigidity. The servo engine and gear is chosen in a way that creates the required pair M_s and the imposed acceleration ε_s, which should take the load to the required speed. The mathematic pattern reflected the parameters of the engine J_m and K_m at the output axis. The choice of the optimum transmission raises a complex problem in the case when it is imposed a minimal angular velocity to trace ω_s and ε_s.

3. The Optimum Working Regime

The parameters which characterize the economic regime are the training electric power and the efficiency of all the structural components. The basic problem in

order to obtain a profitable regime is to correctly establish the nominal power
according to the efficiency, the transmission report, the increase or decrease in
the speed and the cinematic moment. In the situation of the actuators, to
establish acting power is very important owing to the conditions of transitory
regime of work.

When calculating the overall efficiency of the actuator's transmission, we will
approximate it taking into account only the losses that occur due the friction
within the mechanism, neglecting among others like the degree of covering.
To take into account all the losses we can write the relation of the overall
efficiency according to the total / overall moment M_t with the constant ΔM_c and
variable ΔM_a for mechanical losses as it follows:

$$\eta_t = \frac{M_t}{M_t + \Delta M_c + \Delta M_a} \tag{7}$$

If we define: the loading coefficient, $K_i = M_t / M_n$ and the loss coefficient, $K_p = \Delta M_t / M_t$ using the relation (7) results:

$$\eta_t = \frac{\eta_n}{1 - \eta_n K_p \left(1 - \dfrac{1}{K_i}\right)} \tag{8}$$

For this, we make real assessment of the value of the efficiency of the actuator
transmission considering the overall of the power losses within the actuator and
for partial loading.

For the transitory regimes of functioning, the efficiency can be calculated by
the two components of the moment of losses within the transmission according
to the relation (6) including the dynamic moment.
Establishing the loading coefficient is necessary in view of the choice of the
acting engine and of the calculation of the overall efficiency of the mechanical
transmission of the actuator.

Summary and Conclusions

The research is of great importance for the present calculation algorithms
regarding the main dynamic parameters, the power and the mechanical efficiency.
The applicative and experimental researches and the industrial validation of these
which were tested on the theoretical patterns implemented in practice showing the
convergence of the ways of approaching to the problems to reality.

It results the great importance of the correct establishing of the functioning in
this regime by mathematical modeling of these influences.

The kinematic and dynamic analysis on synthetic pattern of the servo-analog
rapid control actuator type system has direct implications by deducted practical
recommendations to design the transmissions of mechatronic systems.

For the actuators included in machine tools with digital control or in the manufacturing centers, the dynamic stability is of utmost importance, fact that makes the study of the loading coefficient variation in a transitory regime when starting under loading welcome and trends.

Acknowledgement

References

[1]. Borangiu, Th.. (2003). Advanced Robot Motion Control. Editura AGIR, Editura Academiei Romane. Bucureşti

[2]. Ispas, C., Predencea, N., Ghionea, A Constantin, G (1998), Maşini-unelte. Editura Tehnică. Bucureşti

[3]. Măties, V., Mândru, D. (2000). Actuatori în mecatronică. Editura Mediamira Cluj-Napoca.

[4]. Mohora, C., Cotet, E., Pătraşcu, G. (2001). Simularea sistemelor de producţie. Editura Academiei Romane, Bucureşti.

[5]. Năsui, V. (2006). Actuatori liniari electromecanici. Editura Risoprint Cluj-Napoca.

[6]. Năsui, V. (2009) Actuator mecanism întinzator de bandă. Brevet de Inventie RO122347 B1.

[7]. Năsui, V., CoteŢiu, R., Ungureanu, N. (2010), Studies of the Performances of Dynamic Regimen for Electro Mechanic Actuators, Manufacturing Engineering, Vyrobne Inzinierstvo, cislo2, rocnik IX, 2010, pag 70-74.

[8]. Olaru, A. (2001). Dinamica roboşilor industriali. Editura Bren, Bucureşti

Detection of fretting fatigue crack initiation by thermography

Saosometh CHHITH, Wim DE WAELE, and Patrick DE BAETS

Department of Mechanical Construction and Production, Laboratory Soete,
Ghent University, Belgium

Abstract

Three fretting fatigue tests under partial slip conditions are monitored using an infrared camera to detect crack initiation of the fatigue samples prior to final failures. 10 thermal images per fatigue cycle are captured for a period longer than calculated number of cycles of crack propagation before failures. After failures, temperatures evolutions at maximum fatigue load of 4 zones of interest are analyzed during this period. The temperatures of all zones of interests reach a stabilization before a thermal indication of crack initiation.

Keywords

fretting fatigue tests, crack initiation, thermography, on-line inspection

1. Introduction

Fretting occurs when clamped components are subjected to vibration. Macroscopic relative displacement between the components cannot be observed, however at microscopic level, two sliding regimes which are partial slip and gross slip can be observed. Partial slip or mixed stick-slip is a regime where sticking appears at center of the contact area and slipping occurs at both sides of contact edges. Gross slip is a regime where the whole contact area slides relative to each other. Usually, cracking is evident as a dominant mechanism for failure in partial slip condition, but the wear is often observed for gross slip (Fouvry et al., 1996). Therefore, in this study, partial slip conditions are selected. Example installations and machine components that are cyclically loaded and prone to this type of damage are press-fitting, bolted connections, riveting lap joints, dovetail connections, etc.

   Like plain fatigue, fretting fatigue lifetime is divided into two proportions: crack initiation and crack propagation. For fretting fatigue, the latter part has been more or less solved based on linear fracture mechanics (Fouvry et al., 2008), (Nowell and Araújo, 1999). It is the former problem which continues to attract the attention of researchers (Hills and Nowell, 2014). Multi-axial fatigue models to predict crack initiation have been successfully implemented, which are validated by conventional microscopy (Nowell and Araújo, 2002),

(Proudhon et al., 2006), (Fouvry and Kubiak, 2009), (Fouvry et al., 2014). Off-line inspections lead to destruction of samples and in addition, if the samples are stopped, tests could not be restarted as contact conditions are hardly maintained. However, there have been very limited on-line techniques to validate these models. Only potential drop techniques were utilized by Kondo et al. (2005) and Meriaux et al. (2010) to measure crack initiation of fretting fatigue tests. In this work, thermography is used as an online tool to measure a crack initiation of a fretting fatigue test. The term crack initiation is defined that a crack depth is 1 mm as used by Szolwinski and Farris, (1998).

There are two approaches of thermography which are applied to investigate plain fatigue (Ummenhofer and Medgenberg, 2009), the first approach is analysis of temperature changes due to thermoelasticity or thermal stress analysis (TSA). The second one is an attempt to analyze mean temperature evolution to quantify the plastic dissipation. For the second approach, several methodologies have been used. Some of them measure mean temperature evolution at just the beginning of the test to predict fatigue limit of materials (Rosa and Risitano, 2000), (Luong, 1998), (Fan et al., 2012). This technique was also used to determine damage threshold of plain fretting (Berthel et al., 2014). On the other hand, fatigue tests are run until specimens failures and number of cycles to crack initiation is determined (Ranc et al., 2008) and (Plekhov et al., 2005). In this study, the latter technique is adopted to measure crack initiation in a fretting fatigue test.

2. Experiments
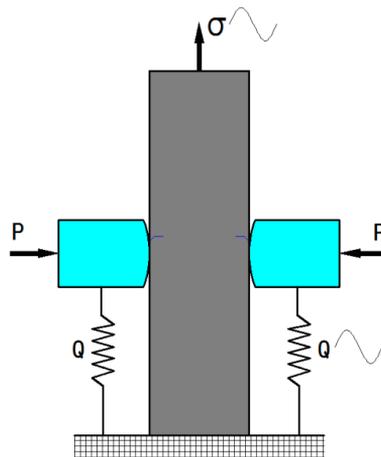
Figure 1. Schematic diagram of fretting fatigue test

Fretting fatigue tests
Materials and samples of Hojjati-talemi et al. (2014) are used in this study. Remote fatigue load (σ) is run with an amplitude of 175 MPa, a frequency of 10

Hz, and a fatigue ratio ($R=\sigma_{min}/\sigma_{max}$) of 0.1. A normal load (P) is kept constant at 600 N, while tangential force (Q) of 200 N is induced by a spring in-phase with the remote fatigue load. Loading conditions are to ensure that sliding regimes of fretting fatigue tests stay in partial slip conditions after steady state regime and global elasticity of materials are obtained. The fretting fatigue test set-up is shown schematically as in figure 1. Three fretting fatigue tests of identical loading conditions are repeated.
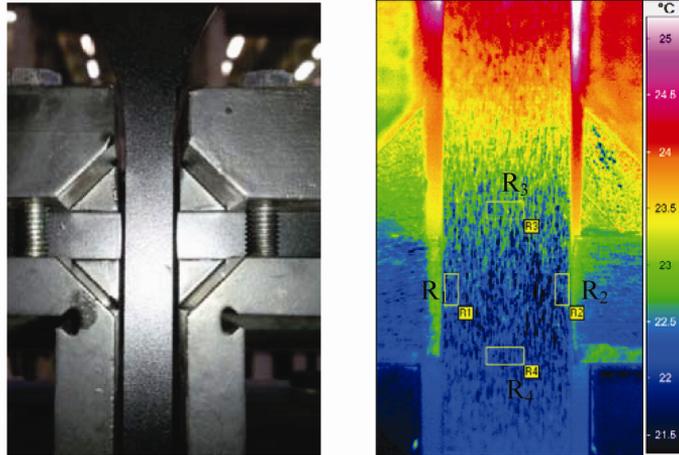
(a) Painted specimen in black   (b) Thermal image with 4 zones of interests

Figure 2. Painted specimen and corresponding thermal image

Infrared thermography

The infrared (IR) camera used in this study is InfraTec brand model 8300 series which has spectral range between 2-5µm and a resolution of 614 by 512 pixels. The detector in the scanner unit is indium antimonide (InSb) and cooled by a stirling cooler. The temperature sensitivity is 25mK at room temperature. The camera is used with default standard calibration for temperature ranges between 5-300°C. The lens is telephotolens with focal length of 50 mm. Specimens and pads of fretting fatigue tests are painted black (see figure 2a) to improve emissivity of the samples. Thermal images are captured with a frame rate of 100Hz for a period before final failure estimated by previous experimental results. This period must be longer than the duration for a crack depth of 1 mm to propagate until failure since the definition of crack initiation here is a crack depth of 1 mm. Therefore, there are 10 thermal images in a fatigue cycle. 4 zones of interests (R_1, R_2, R_3, and R_4) are selected as illustrated in figure 2b, two of which (R_1 and R_2) locate at the left and right contacts where cracks are likely to appear while R_3 and R_4 are used as references.

3. Experimental results and discussions

Thermal sources in fretting fatigue are combination of fretting friction and fatigue. Normally, fretting friction causes a sharp-risen temperature during running-in phase and reaches a stabilized value in steady-state regime due to environmental losses (conduction, convection and radiation). On the other hand, thermoelasticity-induced heat in fatigue loading (tension gives a drop of temperature while compression gives a rise of temperature) does not affect global change of temperature in materials within elastic ranges. In this sense, temperature evolution in fretting fatigue must reach a steady-state regime as well, which allows to detect a crack initiation if there is an increase of temperature after this steady-state period. Temperature evolutions at maximum fatigue load are analyzed after all the 3 fretting fatigue tests (see figures 3-5) since heat dissipation at this maximum fatigue load is also considered to be the largest within a cycle. In figure 3, temperatures evolutions of all zones of interests reach stabilization before the one of R_2 (right contact) deviate from others. This indicates crack initiation at the right contact. The size of the detectable crack is approximately 1mm depth based on the number of cycles of crack propagation calculated by formula of Szolwinski and Farris, (1998). In figure 4, no thermal indications of crack initiation exist as temperatures of all zones of interests stay together even though there is crack growth until the specimen fails. In figure 5, thermal indication of crack initiation at the right-side contact (R_2) appears very late at the end of the test.
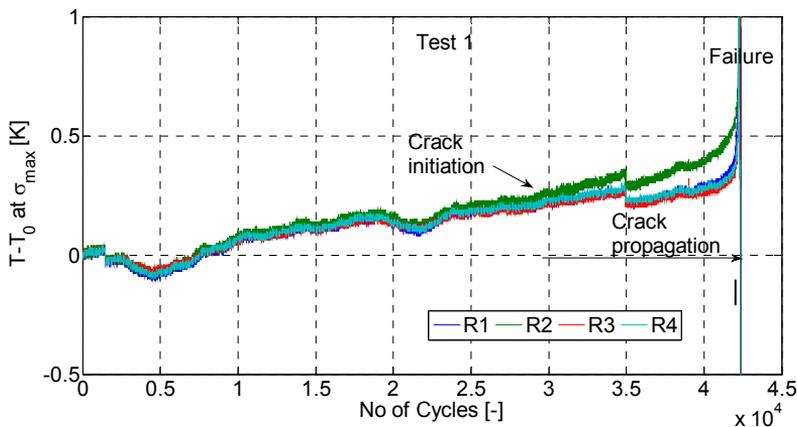
Figure 3. Temperature evolution at maximum fatigue load of test 1 before failure

To interpret the scattering of the above results of crack initiation detection, contact alignments are inspected as crack is always initiated at the trailing edge of the contact area. Only contacts at the right side are shown in figures 6 since in all tests crack is initiated from this side. In figure 6a, contact area locates at the

front of the specimen where the IR camera is installed so that clear thermal
indication of crack initiation occurs. In this case, crack can quickly reach the
front surface after the initiation.
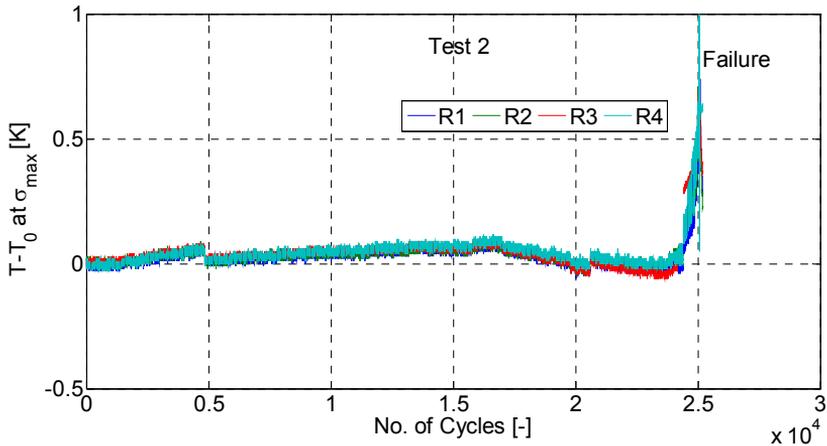
Figure 4. Temperature evolution at maximum fatigue load
of test 2 before failure
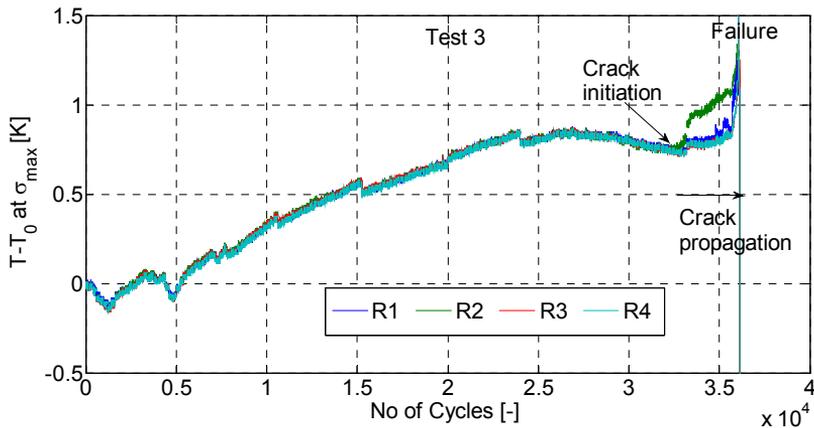
Figure 5. Temperature evolution at maximum fatigue load
of test 3 before failure

In figure 6b, contact area at the back of the sample does not allow any thermal
detection though the specimen fails. This can be because crack propagation to
final failure does not reach the front surface. In figure 6c, contact area which is
in the middle of the specimen also enables detection of crack initiation but at a
very small period before the failure. In this case, there can be a delay for a crack
to reach the front surface since it is initiated from the center of the specimen.

(a) Test 1   (b) Test 2   (c) Test 3
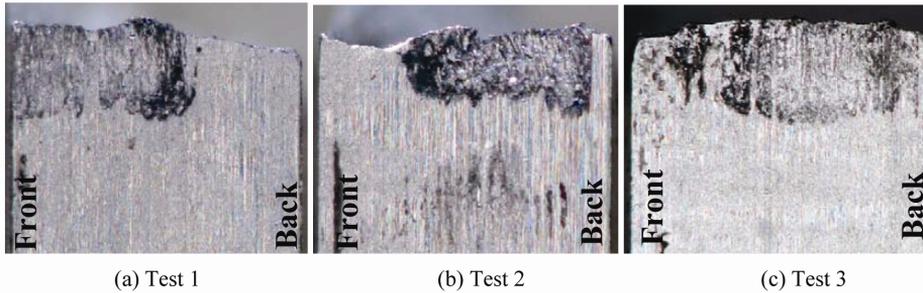
Figure 6. Right-side contacts of the specimens

Conclusions and future work

Contact alignment is a very important factor for this study. Detection of crack initiation seems to be feasible when cracks reach the front surface where the IR camera is installed. The detectable crack depth could be around 1mm. Modification of the test set-up is being made to achieve better line contact and repeatability of the contact alignment. Furthermore, a new post-processing technique of thermal images are also being conducted to detect subsurface cracks and smaller crack depth around 100 μm, and the technique is aimed at direct on-line inspection without running the fretting fatigue tests until failures of the specimens.

Acknowledgements

References

[1] Berthel, B., Moustafa, A.-R., Charkaluk, E., and Fouvry, S. (2014). Crack nucleation threshold under fretting loading by a thermal method. Tribology International, 76, 35–44.

[2] Fan, J., Guo, X., and Wu, C. (2012). A new application of the infrared thermography for fatigue evaluation and damage assessment. International Journal of Fatigue, 44, 1–7.

[3] Fouvry, S., Gallien, H., and Berthel, B. (2014). From uni- to multi-axial fretting-fatigue crack nucleation : Development of a stress-gradient-dependent critical distance approach. International Journal of Fatigue, 62, 194–209.

[4] Fouvry, S., Kapsa, P., and Vincent, L. (1996). Quantification of fretting damage. Wear, 200(1-2), 186–205.

[5] Fouvry, S., and Kubiak, K. (2009). Introduction of a fretting-fatigue mapping concept: Development of a dual crack nucleation – crack propagation approach to formalize fretting-fatigue damage. International Journal of Fatigue, 31(2), 250–262.

[6] Fouvry, S., Nowell, D., Kubiak, K., and Hills, D. a. (2008). Prediction of fretting crack propagation based on a short crack methodology. Engineering Fracture Mechanics, 75(6), 1605–1622.

[7] Hills, D. a., and Nowell, D. (2014). Mechanics of fretting fatigue—Oxford's contribution. Tribology International, 76, 1–5.

[8] Hojjati-talemi, R., Wahab, M. A., Pauw, J. De, and Baets, P. De. (2014). Tribology International Prediction of fretting fatigue crack initiation and propagation lifetime for cylindrical contact con fi guration. Tribiology International, 76, 73–91.

[9] Kondo, Y., Sakae, C., Kubota, M., and Yanagihara, K. (2005). Non-propagating crack behaviour at giga-cycle fretting fatigue limit. Fatigue Fracture of Engineering Materials and Structures, 28(6), 501–506.

[10] Luong, M. P. (1998). Fatigue limit evaluation of metals using an infrared thermographic technique. Mechanics of Materials, 28(1-4), 155–163.

[11] Meriaux, J., Boinet, M., Fouvry, S., and Lenain, J. C. (2010). Identification of fretting fatigue crack propagation mechanisms using acoustic emission. Tribology International, 43(11), 2166–2174.

[12] Nowell, D., and Araújo, J. A. (1999). Analysis of pad size effects in fretting fatigue using short crack arrest methodologies. International Journal of Fatigue, 21, 947–956.

[13] Nowell, D., and Araújo, J. A. (2002). The effect of rapidly varying contact stress fields on fretting fatigue. International Journal of Fatigue, 24, 763–775.

[14] Plekhov, O., Palin-Luc, T., Saintier, N., Uvarov, S., and Naimark, O. (2005). Fatigue crack initiation and growth in a 35CrMo4 steel investigated by infrared thermography. Fatigue Fract. Engng Mater. Struct, 28(1-2), 169–178.

[15] Proudhon, H., Fouvry, S., and Yantio, G. R. (2006). Determination and prediction of the fretting crack initiation: introduction of the (P, Q, N) representation and definition of a variable process volume. International Journal of Fatigue, 28(7), 707–713.

[16] Ranc, N., Wagner, D., and Paris, P. C. (2008). Study of thermal effects associated with crack propagation during very high cycle fatigue tests. Acta Materialia, 56(15), 4012–4021.

[17] Rosa, G. La, and Risitano, A. (2000). Thermographic methodology for rapid determination of the fatigue limit of materials and mechanical components ☆. International Journal of Fatigue, 22, 65–73.

[18] Szolwinski, M. P., and Farris, T. N. (1998). Observation, analysis and prediction of fretting fatigue in 2024-T351 aluminum alloy. Wear, 221(1), 24–36.

[19] Ummenhofer, T., and Medgenberg, J. (2009). On the use of infrared thermography for the analysis of fatigue damage processes in welded joints. International Journal of Fatigue, 31(1), 130–137.

Adhesion of polymer surfaces: brief review

Hayder AL-MALIKI[1], Gábor KALÁCSKA[1], Róbert KERESZTES[1],
Patrick DE BAETS[2]

[1]Institute for Mechanical Engineering Technology, SZIE, Gödöllő
Szent István University
[2]Laboratory Soete, University Gent, Belgium

Abstract

PhD research program is dedicated to study the adhesive behaviour of engineering polymers. Within the topic the modification of adhesive behaviour of the surfaces are highlighted concerning further adhesive bonding. The improved surface adhesion is important for e.g. mounting a gear on shaft or bearing bushing but packaging industry are also interested in enhanced surface adhesion. One of the potential methods for the surface modification is atmospheric cold plasma treatment. The PhD research program is focusing on natural and modified adhesive capabilities. This article gives a brief review about the basics of surface adhesion of polymeric materials.

Keywords

Adhesion, polymer, plasma treatment

1. Introduction

Basics of adhesion
Adhesion is the interatomic and intermolecular interaction at the interface of two surfaces [1]. It is a multi-disciplinary topic which includes surface chemistry, physics, rheology, polymer chemistry, stress analysis, polymer physics and fracture analysis. Describing the mechanism of adhesion in simple terms is difficult due to the complexity and evolving understanding of the subject [2]. The ultimate goal is to identify a single mechanism that explains adhesion phenomena [3,–4]. A range of adhesion mechanisms, based variously on diffusion, mechanical, molecular and chemical and thermodynamic adhesion phenomena, are currently the subject of debate in the literature.

Adhesion of polymer systems
The automotive and aerospace industries have been investigating adhesives and the associated adhesion mechanisms for more than 50 years. In recent times, the interest from the sector in adhesion has been directed towards polymers and epoxy resins due to their advantageous bulk and surface properties, low cost and good mechanical properties [5,–11]. Adhesion between the polymer surface and

the paint substrate layer, for example, is controlled by the chemical groups at or near the interface [12]. A common example of an adhesive system found in the automotive industry is the attachment of a paint coating to a polymer bumper bar. Such bumper bars are frequently made with polypropylene (PP); a material exhibiting poor surface adhesive properties in its native state.

2. Adhesion mechanisms

The recent adhesion literature contains studies of three main adhesion mechanisms: mechanical coupling, molecular bonding, and thermodynamic adhesion. These are considered in the following sections. A brief overview of the electrical, rheological and weak boundary adhesion mechanisms is also presented.

Mechanical coupling
The mechanical coupling or interlocking (hook and eye) adhesion mechanism is based on the adhesive keying into the surface of the substrate [9, 7, and 8]. This is similar to glue on wood, in that the glue locks into the rough irregularities on the surface of the wood [6] Fig.1 illustrates the interlocking concept. The current debate surrounding mechanical adhesion concerns the significance of interlocking in explaining surface adhesion. On one side of the argument, it is believed that mechanical interlocking provides higher adhesion strength. Other researchers believe that roughening of the surface is simply increasing the surface area for more molecular bonding interactions [10, 9]. In the following section, highlights from that debate are reported and practical examples are presented.
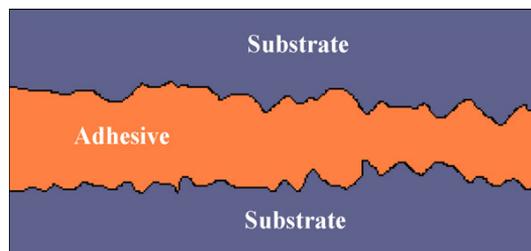
Figure 1. Illustration of mechanical coupling between two substrates.

Molecular bonding
Molecular bonding is the most widely accepted mechanism for explaining adhesion between two surfaces in close contact. It entails intermolecular forces between adhesive and substrate such as dipole-dipole interactions, van der Waals forces and chemical interactions (that is, ionic, covalent and metallic bonding). This mechanism describes the strength of the adhesive joints by interfacial forces and also by the presence of polar groups [6]. Molecular bonding

mechanisms require an intimate contact between the two substrates as shown in Fig. 2. However, intimate contact alone is often insufficient for good adhesion at the interface due to the presence of defects, cracks and air bubbles [3].
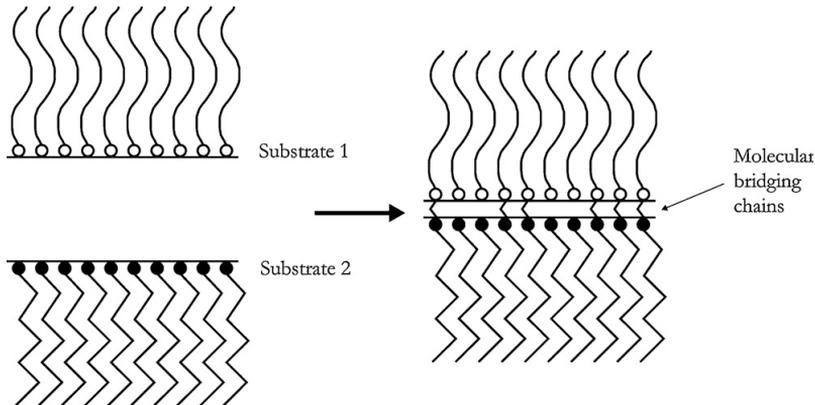
Figure 2. Schematic of the molecular bonding between substrates.

3. Evaluation of contact angle

In 1855, Young considered a liquid of known surface tension γL in contact with a simple solid, smooth, homogeneous, non-deformable and isotropic surface. The strength of adhesion for a simple system like the one displayed in Fig. 3 may be estimated through the work of adhesion (*Wa*)
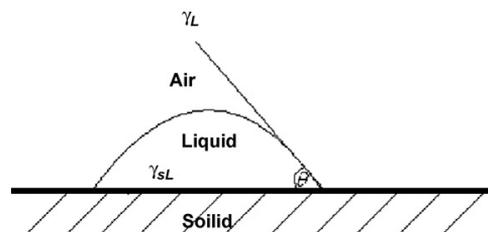
Figure 3. Sessile drop on a surface indicating the contact angle and surface tensions.

Which is defined as

$$Wa = \gamma S + \gamma L - \gamma SL \tag{1}$$

Where γS, γL and γSL represent the tensions of the solid/air, liquid/air and solid/liquid interfaces respectively. The challenge with this equation is that only γL can be measured with confidence as the surface tension of the solid can only be experimentally determined against a series of known liquids.

Young qualitatively described a relationship between these tensions, which may be stated algebraically as:

$$\gamma L \cos\Theta = \gamma S - \gamma SL \qquad (2)$$

Eq. (2) is commonly referred to as Young's equation. Defined work of adhesion (*Wa*) leading to the equation:

$$Wa = \gamma L \,(1 + \cos\Theta) \qquad (3)$$

In a real system, however, macroscopic surface roughness and surface chemical heterogeneity (non-uniform surface chemistry) may give rise to contact angle hysteresis; the advancing contact angle measured as the test fluid expands the sessile drop and advances of over new surface area is greater than the receding contact angle measured as the sessile drop retreats. This behavior introduces a measure of ambiguity in the determination of contact angle and is a source of conjecture in the application of Eqs. (2) and (3). Nevertheless, many theories have been introduced to describe and measure the surface tension of materials with applications to polymer systems [14].

4. Some materials, methods and results in literature

C. Mandolfino, E. Lertora, C. Gambaro [15] studied HDPE surfaces. Natural, primer treated (commercial product suggested before the use of Loctite 401 TM cyanoacrylate adhesive), and low pressure plasma treated surfaces.
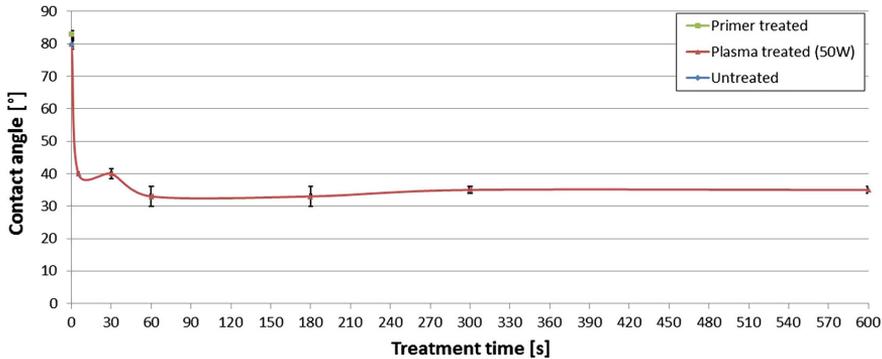
Figure 4. Variation of contact angle measured on polyethylene surface in terms of treatment time and kind of treatment

Figure 4. shows the variation of the demineralised water contact angle values of the low pressure plasma treated polyethylene as a function of treatment time (from 5 to 600 s). Contact angle of untreated and primer treated samples are also reported as a comparison. As it is easy to observe, the use of short exposure times (less than 60 s) is enough to obtain a significant decrease in contact angle

values, which means high wettability of the surface, while longer exposure times do not significantly improve wettability. This is due to the fact that the main act of the air plasma is surface activation by insertion of polar species.

This process occurs during the first seconds of the plasma treatment when the free radicals produced by the action of the plasma gas present high instability and reactivity.

Also here the researchers [15] found the following results when they used cold gas plasma to treating UHMWPE Comparing the effects of CAP-treatment with helium and helium /oxygen cold gas plasmas on medical grade UHMWPE surface properties and forces of adhesion. Results showed that CAP treatment decreased the asperity density of both treated samples by half that of the untreated UHMWPE; the treatment also reduced the height of these asperities due to plasma etching. However, the CAP-treatment did not affect the overall surface energy of the tested samples as there was little difference in the surface energy parameters, although a decrease in contact angle of water was noticed in the treated UHMWPE samples, thereby improving the hydrophilicity.

Polymer surfaces [16] can be modified by a plasma treatment in different ways (etching, cleaning, activation, cross-linking), for example to improve wetting properties, to enhance the adhesion of plasma-deposited coatings, or to reduce friction. However, the deposition of coatings is often beneficial to taylor the surface properties of polymers. PECVD of siloxane or fluorocarbon layers renders polymer surfaces hydrophobic. A hydrophilic treatment by the deposition of SiOx layers was found to be more permanent than a plasma treatment with non-film forming gases like N2 demonstrated on PC.
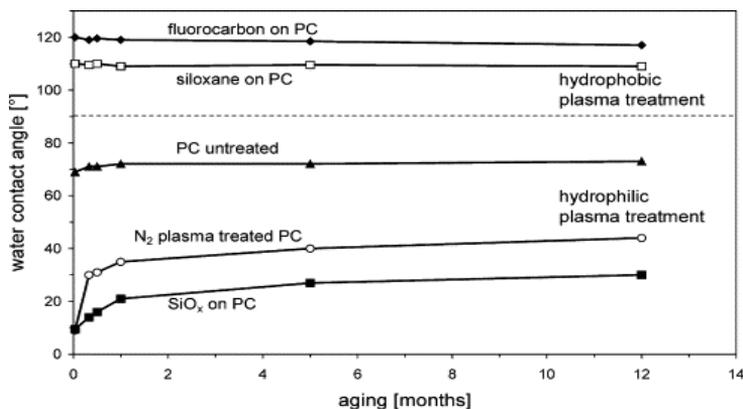
Figure 5. Aging of untreated, plasma treated and coated PC sheets. The polycarbonate surface can be rendered hydrophobic or hydrophilic.

Furthermore, lower friction coefficients of EPDM can be achieved with a-C: H or siloxane layers compared to the cross-linking effect of a He or Ar plasma. Nevertheless, plasma-deposited layers should strongly adhere to the polymers to avoid the rapid failure of stressed components. The deposition of graded layers

or ultra-thin films generally improves adhesion, whereby the plasma treatment should be adjusted for different polymers to minimize degradation and aging effects. Nevertheless, it should be kept in mind that all structures, in particular artificially modified surfaces, are subject to aging (Fig.5).

Chi et. al [17] studied the effect of atmospheric pressure N2 plasmas with low gas temperature below 60 °C on PP surface. This plasma is effective to improve the adhesion of polypropylene surface via providing chemical and physical changes on surface. Adhesion improvement is closely related with excited species in plasma determined by discharge parameter such as power dissipation in discharge. Main excited species in N2 plasma affecting the adhesion is N2* which can create the polymer excited states on polymer surface effectively. These polymer excited states result in the surface oxidation, favorable property to adhesion, through the reaction with O2 from air in the middle of or after plasma treatment. Finally they stated that optimal design of plasma generator is needed to create the reactive radical species effectively in plasmas for adhesion improvement of polymer surface.

Novak et. al [18] tested polyesther material treated by cold plasma in oxygen and nitrogen conditions. The modification of polyester by the SDBD plasma in either N_2 or O_2 results in an increase of roughness of the surface. AFM confirmed the creation of some heterogeneities on the PET surface due to the local melting. EPR measurements of the SDBD plasma modified polymer showed two main singlet signals, which resulted from the radical breakdown of the covalent bonds in the polymer. XPS analysis showed the increase in the oxygen and nitrogen contents in the PET surface layer treated by the SDBD plasma. The surface energy as well as the peel strength of PET significantly increased after modification by the SDBD plasma, and this increase was higher for treatment in O2 compared to N2 atmosphere.

Conclusion

- Working behaviour of sliding or bonded surfaces of engineering polymers show strong relation to the surface adhesion.
- Adhesive capability can be expressed by sessile drop test using contact angle evaluation.
- Cold plasma treatment performed surface energy improvements in many condition, thus it is worth to test with engineering polymers.
- Cold plasma settings e..g. etching time have to set by experiments for each engineering plastics.
- Timing after the plasma treatments is important factor concerning the surface energy. Long term properties of the surfaces have to be investigated.
- The present work highlighted some key elements of our broad research with engineering polymer surfaces, which are taken into account in OTKA K 113039.

Acknowledgement

Reference

[1] Poisson C, Hervais V, Lacrampe MF, Krawczak P. Journal of Applied Polymer Science 2006; 101(1):118–27.

[2] Qin R-Y, Schreiber HP. Colloids and Surfaces 1999; 156:85–93.

[3] Kinloch AJ. Journal of Material Science 1980; 15:2141–66.

[4] Puknszky B, Fekete E. Adhesion and surface modification. Mineral fillers in thermoplastics I; 1999. pp. 109–153.

[5] Sargent JP. International Journal of Adhesion and Adhesives 2005; 25(3):247–56.

[6] Sharpe LH. The Interfacial Interactions in Polymeric Composites 1993; 230:1–20.

[7] Georges F. Polymer Engineering & Science 1995; 35(12):957–67.

[8] Wake WC. Adhesion and the formulation of adhesives. 2nd. Essex: Applied Science Publishers Ltd.; 1982.

[9] Basin VE. Progress in Organic Coatings 1984; 12(3):213–50.

[10] Vasconcelos PV, Lino FJ, Neto RJL, Henrique P. Contribution of the phase–matrix interface to the behavior of aluminum filled epoxies. Materials Science Forum 2004; 455–456:635.

[11] Hutchinson AR, Iglauer S. International Journal of Adhesion and 2006; 26(7):555.

[12] Pijpers AP, Meier RJ. Journal of Electron Spectroscopy and Related Phenomena 2001; 121:299–313.

[13] Firas Awajaa,∗, Michael Gilbert b, Georgina Kellya, Bronwyn Foxa, Paul J. Pigramb Progress in Polymer Science 34 (2009) 948–968 Australia.

[14] C. Mandolfino • E. Lertora • C. Gambaro •M. Bruno Meccanica (2014) 49:2299–2306 Italy.

[15] Emily Callard Preedya, Emmanuel Brousseaub, Sam L. Evansb, Stefano Pernia, c, Polina Prokopovicha, b,c,∗ Colloids and Surfaces A: Physicochem. Eng. Aspects 460 (2014) 83–89 UK-USA.

[16] Dirk Hegemann *, Herwig Brunner, Christian Oehr Nuclear Instruments and Methods in Physics Research B 208 (2003) 281–286 Germany.

[17] Yoon-Ho Choia, Ji-Hun Kima, Kwang-Hyun Paekb, Won-Tae Jub, Y.S. Hwanga (2005): Characteristics of atmospheric pressure N_2 cold plasma torch using 60-Hz AC power and its application to polymer surface modification. Surface & Coatings Technology 193 (2005) 319– 324

[18] I. Novák, A. Popelka, A.S. Luyt, M.M. Chehimi, M. Špírková, I. Janigová, A. Kleinová, P. Stopka, M. Šlouf, V. Vanko, I. Chodák, M. Valentin (2013): Adhesive properties of polyester treated by cold plasma in oxygen and nitrogen atmospheres. Surface & Coatings Technology 235 (2013) 407–416

Positioning algorithms of pneumatic cylinders

László FÖLDI, Eszter SÁRKÖZI, László JÁNOSI

Department of Mechatronics, Institute for Mechanical Engineering Technology

Szent István University

Abstract

There are three main positioning algorithms of pneumatic cylinders: PID controller, status controller and sliding mode controller. Most commonly used method of them is the PID controller, which is simple and available in most industrial controllers, but it is working point-dependent. The status controller is based on the PD controller, where the derivative is in negative feedback. As it takes into consideration the moving parameters, such as velocity and acceleration, it works better in pneumatic actuators. The sliding mode controller is robust and working point-independent, but chattering can occur during the use of it. The aim of our research is to improve a selection method using this three algorithms, which can determine the optimal control algorithm in varying circumstances.

Keywords

Position Control, PID, Status controller, Sliding mode controller, Pneumatic cylinder

1. Introduction

In order to achieve linear motion, pneumatic, electromagnetic and hydraulic actuators are typically used. Due to their advantageous characteristics in position control applications the latter two are more widespread. Though using hydraulic actuators high velocity and great force is achievable, and their position control can also be relatively easily solved, a handicap is that the leaking of hydraulic fluids might contaminate the workpiece. Electromagnetic actuators on the other hand are clean and reliable in their operation but often require a mechanical transmission, both to convert high speed and low torque to a more useful combination and to convert rotary motion to linear motion. While linear motors overcome the need for transmission, they can be [Gyiveki, 2007].

Pneumatic actuators have several advantages: they are fast, cheap, have an outstanding power-to-weight ratio, are easily maintainable and they don't contaminate the work piece. The challenge to the use of pneumatic drives is that due to piston friction and the characteristics of compressed gas flow their behaviour is non-linear. As a result their industrial use is only widespread in applications which require linear motions between end positions.

In the last decade such industrial controllers became available which have adequate computing capacity for real-time usage. Thus there is now opportunity to develop pneumatic systems which don't require costly proportional valves for positioning and hence the usage of the more cost-efficient solenoid valves became possible (Figure 1.). These simple on/off valves are cheap and easily maintainable. Their drawback however is that as yet the required control method is not appropriately elaborate: the solutions offered in the scarce publications on the topic consist of applying conventional control methods (PID, sliding mode, fuzzy logic) or their hybrid versions, with varying success.

A review of the papers on the topic is given in Table 1, where the applied control methods, the number of required valves and the highest positioning accuracy is shown. Even though it is not indicated in the table, in some cases certain speed or force decreasing solutions (eg. throttle valve, reduced pressure) were used, which naturally may have an effect on the operating range of the positioning system and the steady-state error. The employed valve's switching time is also omitted from the table.

Table 1. A review of the papers on the topic

Authors	Control method	Number of required valves	Positioning accuracy
Thomas, M.B.; Maul, G.P.; Jayawiyanto, E.	Modified PD + PWM control	3	±0,1 mm
Ahn, K.; Yokota, S.	MPWM + neural network (LVQNN)	8	±0,2 mm
Parnichkun, M.; Ngaecharoenkul, C.	hybrid of fuzzy and PID + PWM control	1	±3,5 mm
Nguyen, T.; Leavitt, J.; Jabbari, F.; Bobrow, J.E.	Sliding mode control	4	±0,1 mm
Shih, M.-C.; Ma, M.-A.	Fuzzy + modified differential PWM control	2 + Prop. pressure valve	±0,075 mm
Messina, A.; Giannoccaro, N.I.; Gentile, A.	Individual control + PWM	2	±0,1 mm
Barth, E.J.; Zhang, J.; Goldfarb M.	Individual linear continuous + PWM	2	N/A
Akdağ, F.N.; Kuzucu, A.	Sliding mode control	2	±0,05 mm
van Varseveld, R.B.; Bone, G.M.	PID with friction compensation + PWM	2	±0,21 mm

2. Control methods

PID controller

Nowadays the PID controller (proportional-integral-derivative controller) algorithm is the most widely used in industrial control systems. It is able to

respond to the current control error, the past error and the future error. The past error is characterized by the integral of error, the future error by the derivative of the error. Accordingly, this algorithm modifies the error through three channels: via the proportional channel, the integral channel and the derivative channel. PID controller is popular because it is reliably able to fulfill the prescribed control requirements in most industrial applications despite of it's relatively simple structure. The algorithm calculates the control variable as a function of the difference of the process output and the setpoint [van Varseveld et al., 1997]. There are several designs of PID controllers due to the used channels (proportional, integral, derivative channels) in the controller, e.g. P, PD, PI, PID controllers.

The PID controller the effects of the three channels (proportional, integral, derivative). Accordingly the calculation of the control variable as a function of the error in continuous time domain is:

$$u(t) = K_P \cdot \left(e(t) + T_d \frac{de}{dt} + \frac{1}{T_i} \int_0^t e(\tau) d\tau \right), \quad K_P, T_i, T_d > 0 \tag{1}$$
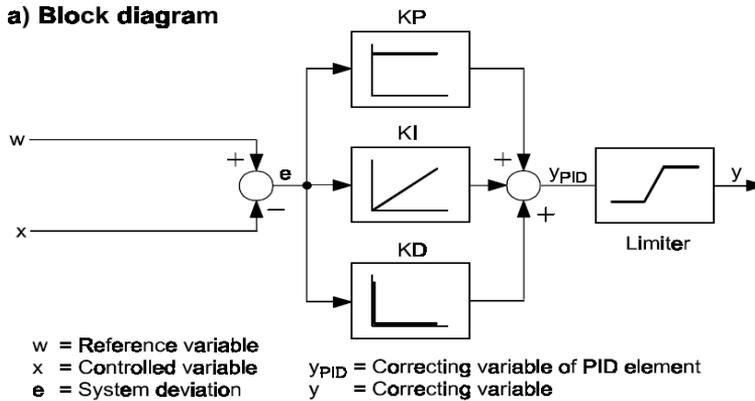
Figure 1. Block diagram of PID controller with limited output

In practice the designation of the proportional element is P or KP. The integral effect can be defined with the use of the integral gain or the integral time constant. Similarly, the derivative effect can be defined with the use of derivative gain or derivative time constant. The form which is used in practice is:

$$y_{PID} = K_P \cdot e + K_I \cdot e \cdot t + K_D \cdot \frac{de}{dt} \tag{2}$$
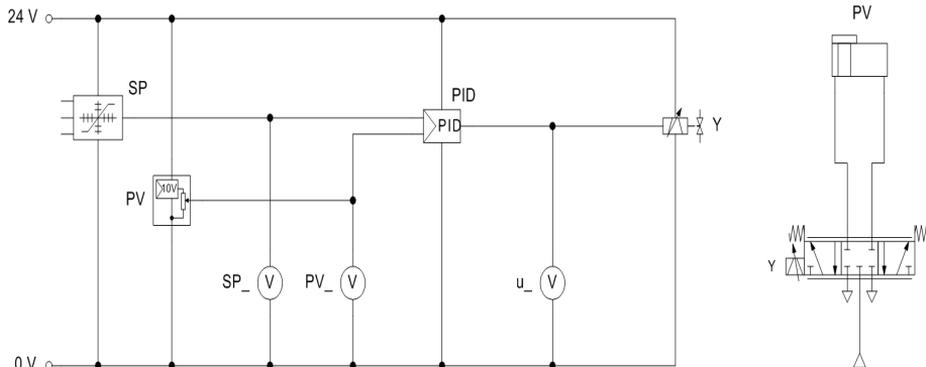
Figure 2. PID controller

Status controller

The status controller is based on the classic proportion controller with the addition that it takes into account the first and second derivative of the feedback signal. Typical field of application of the status controller is the positioning of pneumatic linear drives. In this case the controlled variable is the position. The first derivative is the velocity, the second derivative is the acceleration. So the status controller takes into consideration the motion parameters. In the block diagram (Fig. 3.) it can be also seen that the velocity and the acceleration have negative impact, so they are a dampings proportionally to the velocity and the acceleration.
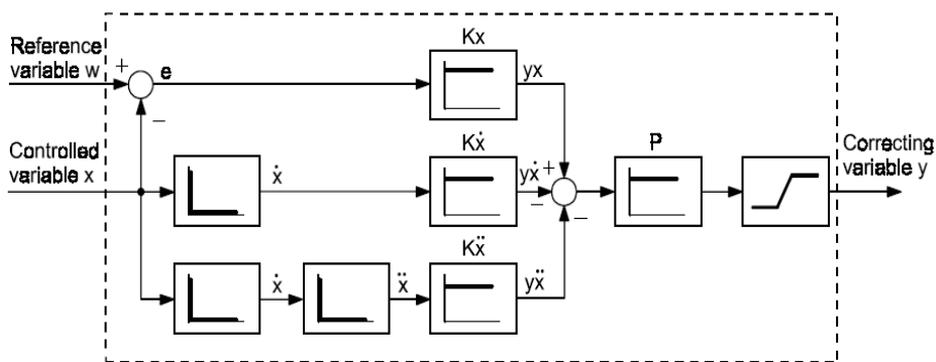
|		
e = Position variation	K_x = Position coefficient	y_x = Position correcting variable
$\dot{x}$ = Velocity	$K_{\dot{x}}$ = Velocity coefficient	$y_{\dot{x}}$ = Velocity correcting variable
$\ddot{x}$ = Acceleration	$K_{\ddot{x}}$ = Acceleration coefficient	$y_{\ddot{x}}$ = Acceleration correcting variable
	P = Total gain	

Figure 3. Block diagram of status controller

The gain proportional to the position error:

$$yx = Kx \cdot e \qquad (3)$$

Damping proportional to the velocity:

$$y\dot{x} = K\dot{x} \cdot \dot{x} \qquad (4)$$

Damping proportional to the acceleration:

$$y\ddot{x} = K\ddot{x} \cdot \ddot{x} \qquad (5)$$
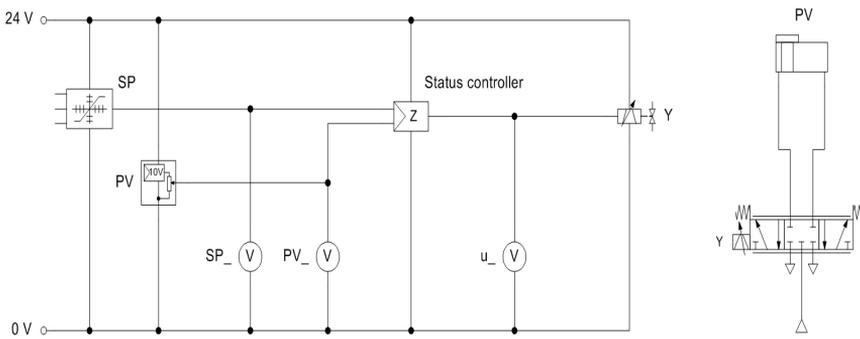
Figure 4. Status controller

Sliding mode controller

The theory of robust controller means the analyzing and designing of systems that are able to manage uncertainty, especially under such conditions in which exact mathematical modelling is not possible. Basically it can be divided into two branches, linear and non-linear robust controllers. One element of the non-linear controllers is the so-called sliding mode controller. In variable structure systems the sliding mode can occur only under certain conditions. The variable structure systems have got some interesting controlling characteristics. A variable structure system can also be asymptotically stable, if all the structures constituted by the variable structure system are itself unstable. Another important feature that the variable structure system –with appropriate controller-may get into such a status, in which the system dynamics can be described with a differential equation with reduced degrees of freedom compared with the origin state. In this state, the system is theoretically completely independent from changes in certain types of parameters and certain types of external disturbance effects. This state is called sliding mode. One great advantage of the variable system control is that it ensures robustness against the non-linearity of the controlled section, the changing of the parameters and the external interferences [Nguyen, 2007].

Another great advantage of this controller is that the exact model of the system is not needed. It is sufficient to know the limits of the noises and the parameter changing. The price of the noise insensitiveness is the infinite great switching frequency, so the rapid repeated intervention. Consequently there is no ideal sliding mode controller in the reality, but it can be approach properly the practical needs. The design of the sliding mode controller contains three main steps. The first step is the design of the sliding surface. The second step is to select a control law, which forces the trajectory of the state variables on the sliding surfaces and then keeps them there. The third is the most important step, it is the chattering free implementation [Gyiveki, 2007].

The design of the sliding surface
The first step is critical in the design of variable structure controller. It is important to define the surface properly, because the controlled section passes through this surface.

Selection of the control law
In the second step that switching controller is designed, which leads the controlled section to the sliding surface, then keeps it there if the trajectory of the controlled section intersects the surface. The simplest control element, that can achieve sliding mode control, is the relay.


$$u_i = u_{max} \cdot sign(s_i)$$
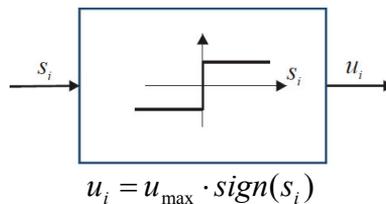
*Figure 5.* Relay as control element
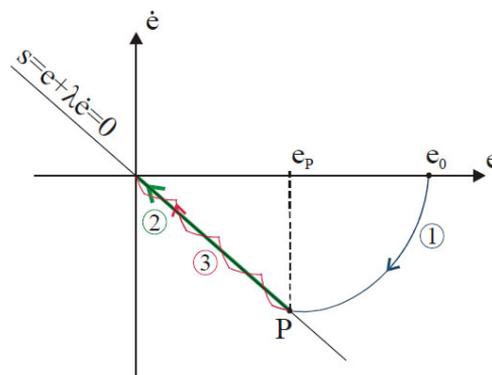
Figure 6. Linear sliding mode

55

The robustness of the sliding mode controller comes from the great (ideally infinite) loop gain. The relay provides this. It is important to note that in reality only a finite switching frequency can be achieved, which causes chattering. This means that the state trajectory of the controlled section perturbates near the sliding surface [Ahn, 2005].

Where (1) is the phase of approach, (2) is the ideal sliding mode and (3) is the chattering. Applying sliding mode controller it should be considered that the perturbation may cause undesirable phenomenon in the controlled section. In the approach phase the system is sensitive to parameter variations and external noises. When the system reaches the sliding mode, its dynamics is defined by the sliding surface, and then it becomes insensitive to parameter variations and external noises. During the design there are two contradictory aspects to consider, the trajectory of the system should reach the sliding surface in the shortest time period, and the chattering should be eliminated as much as possible [Nguyen, 2007].

Chattering free implementation

The chattering is an unplanned oscillation with finite-frequency and finite-amplitude, which is caused by the following: in the modelling process the actuators and sensors, which are considerably faster than the control loop, were neglected (non-modelled dynamics). As the ideal sliding mode controller is infinite fast, all dynamic elements should be taken into account. It is a very important issue to avoid the chattering in practical applications of sliding mode controllers. Fortunately, the accurate model of the loop is not necessary to ensure this. In the first step the sliding mode controller is designed as the loop would be ideal. Just in the second step of the design is dealt with the elimination of the chattering.

Application of boundary layer in order to eliminate the chattering

Instead of the discontinuous $u = u_{max} * sign(s)$ control signal, the use of

$$u = u_{max} \cdot sat(s) = \begin{cases} u_{max} \cdot sign(s) \\ \dfrac{u_{max}}{s_k} \cdot s \end{cases} \quad ha \quad \begin{matrix} |s| > s_k \\ |s| \leq s_k \end{matrix} \tag{6}$$

continuous function is recommended. Thus there is a 2 s_k width boundary layer is developed along the s=0 sliding line. If the current working point is far from the sliding line $(|s| > s_k)$ $sat(s) = sign(s)$, or close to the sliding line (at low s_k distance, boundary layer) a continuous sat(s)≠sign(s) transition is obtained (Fig. 7.).
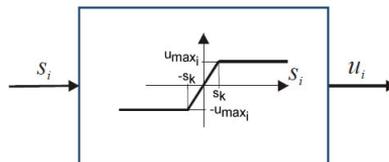

Figure 7. Boundary layer

The above described robust sliding mode controller with the application of boundary layer can be achieved with the use of two conventional PID controller. The dynamic behaviour is determined by three control parameters in case of sliding mode controller: the maximal value of the control signal (u_{max}), the gradient of the sliding line (λ) and the boundary layer measured from the sliding line (sk). The size of the boundary layer (u_{max}/s_k) can be adjusted with the P parameter of PID controller, while the gradient of the sliding line (λ) can be modified by the D parameter. There is no need for integrator in case of sliding mode controller, therefore I parameter is zero. The u_{max} control parameter can be adjusted by the minimal/maximal output parameter of the PID controller.
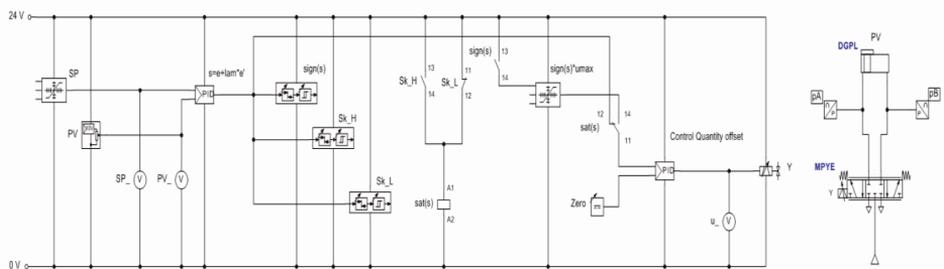
Figure 8. Chattering free sliding mode control with PID controller

3. Apparatus

The circuit diagram of the pneumatic positioning system is presented on figure number 8. As an actuator we applied a Festo DGPL-25-450-PPV-A-KF-B cylinder of 450mm stroke length, to which we attached a Festo MLO-POT-0450-TLF analogue displacement encoder, which has a 0,01 mm travel resolution. The applied encoder is a potentiometer which provides a voltage signal in proportion to the displacement. In order to move the cylinder we applied two MPYE-5-1/8-LF-010-B 5/3 proportional valve.

Figure 9. The experiment apparatus

The major elements of the electronic system are a 0-24 V direct current power supply (NI PS-15), an electronic instrument board (Festo), a NI CompactRIO™ (cRIO 9073) programmable automation controller and the already mentioned electro-pneumatic elements (displacement encoder, pressure sensors and proportional solenoid valve). The applied NI CompactRIO™ programmable automation controller is a modular system; out of its modules we used the analogue-to-digital converter (NI 9201), for a dual purpose. On the one hand we applied it in the controlling process to measure the voltage signal (which is in proportion to the displacement) provided by the displacement encoder. On the other hand we used it in collecting data about the voltage signals corresponding to pressure values (expressed in bars) provided by the analogue pressure sensors. We controlled the proportional solenoid valve with the help of the analog output module (NI 9472). The communication between the CompactRIO™ and the computer was ensured by an Ethernet connection. We realised the real-time control based on equation number (8) by applying the FPGAmodule of CompactRIO™ programming it in the LabVIEW 2009 software. Due to the relative high prices of FPGA systems, later on it would be advisable to elaborate embedded DSP electronics developped for this purpose.

4. Results

The testing of the compiled system was done by determining the quality factors of the control method. During this process we have determined the settling time for step responses from 100 mm to 400 mm, overshoots and steady-state error graphically based on measurement results. The moved load was m=2 kg, the value of supply pressure was 6 bar. The control setting parameters were P =1 [-], D = 400 [ms], based on previous experiences with the system the width of the tolerance band was set to be $s_k = \pm 2$ [-], we regarded the position as adequate within this range.
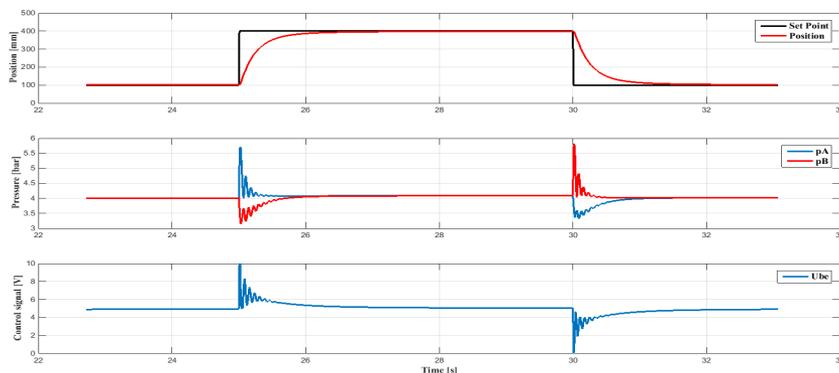

Figure 10. Step response - 100-400 and 400-100 mm, m = 2 kg

At the first measurement (Figure 10.) we have examined a displacement which is long compared to the stroke length of the cylinder by setting the reference signal at 400 mm. It is visible that in the case of large step size the control method is able to follow the dynamics of the cylinder, the overshoot is minimal while the settling time is 1 second. The steady-state error is again equivalent to the travel resolution of the displacement encoder. After this we examined the movement of the piston in the negative direction, namely when it moves backwards into the cylinder. We can see a displacement similarly great to the previous experiment, but in the negative direction. The overshoot is minimal, and the settling time is still under 2 seconds. The steady-state error is once again equivalent to the resolution of the displacement encoder.

The evaluation of the second test (figure 11) we changed the load of the cylinder m = 10 kg, the value of supply pressure was 6 bar.
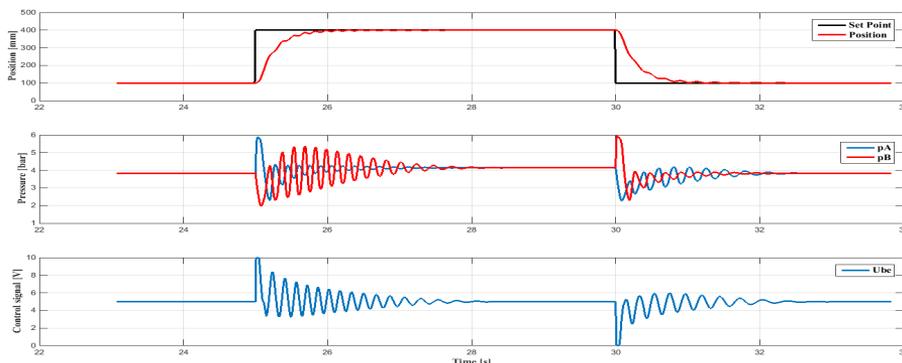
Figure 11. Step response - 100-400 and 400-100 mm, m = 10 kg

We have examined a displacement which is long compared to the stroke length of the cylinder by setting the reference signal at 400 mm. It is visible that in the case of large step size the control method is able to follow the dynamics of the cylinder, the overshoot is minimal while the settling time is 1 second. The steady-state error is again equivalent to the travel resolution of the displacement encoder.

Summary

There are three main positioning algorithms of pneumatic cylinders: PID controller, status controller and sliding mode controller. Most commonly used method of them is the PID controller, which is simple and available in most industrial controllers, but it is working point-dependent. The status controller is based on the PD controller, where the derivative is in negative feedback. As it

takes into consideration the moving parameters, such as velocity and acceleration, it works better in pneumatic actuators. The sliding mode controller is robust and working point-independent, but chattering can occur during the use of it. The aim of our research is to improve a selection method using this three algorithms, which can determine the optimal control algorithm in varying circumstances. In this paper the three algorithms were presented and we tested the sliding mode controller on pneumatic cylinder positioning.

References

[1] Ahn, K., Yokota, S., Intelligent switching control of pneumatic actuator using on/off solenoid valves, Mechatronics,15, 683–702, 2005.

[2] Akdağ, F.N., Kuzucu, A., Highly accurate pneumatic position control, Istanbul Technical University Mechanical Engineering Department, http://digital.ni.com/

[3] Barth, E.J., Zhang, J., Goldfarb, M., Control Design for Relative Stability in a PWM-Controlled Pneumatic System, Journal of Dynamic Systems, Measurement, and Control, 125, 504-508, 2003

[4] Gergely, Z., Judák, E. (2008): „Automatizált paprikaválogatás beágyazott alakfelismerő rendszerrel" Mezőgazdasági technika, XLIX. évf. 2008/11. HU ISSN: 0026-1890

[5] Gerhartz J.- Scholz, D. – Closed-Loop Pneumatics, Workbook TP111, Copyright by Festo Didactic GmbH & Co., D-73770 Denkendorf 2001

[6] Gyeviki János: „Szervopneumatikus pozícionálás pontosságának növelése DSP alapú csúszómód szabályozással", Debreceni Egyetem Mezőgazdaságtu-dományi Kar, Debrecen, 2007

[7] Messina, A., Giannoccaro, N.I., Gentile, A., Experimenting and modelling the dynamics of pneumatic actuators controlled by the pulse width modulation (PWM) technique, Mechatronics, 15, 859–881, 2005.

[8] Nguyen, T., Leavitt, J., Jabbari, F., Bobrow, J.E., Accurate Sliding-Mode Control of Pneumatic Systems Using Low-Cost Solenoid Valves, IEEE/ASME Transactions on mechatronics, 12(2), 216-219, 2007.

[9] Parnichkun, M., Ngaecharoenkul, C., Kinematics control of a pneumatic system by hybrid fuzzy PID, Mechatronics, 11, 1001-1023, 2001.

[10] Shih, M.-C., Ma, M.-A., Position control of a pneumatic cylinder using fuzzy PWM control method, Mechatronics, 8, 241-253, 1998.

[11] Thomas, M.B., Maul, G.P., Jayawiyanto, E., A Novel, Low-Cost Pneumatic Positioning System, Journal of Manufacturing Systems, 24(4), 377-387, 2005.

[12] van Varseveld, R.B., Bone, G.M., Accurate position control of a pneumatic actuator using on/off solenoid valves, IEEE/ASME Transactions on Mechatronics, 2(3), 195-204, 1997.

The effect of residual compressive stresses
on fretting fatigue lifetime

Jan DE PAUW, Wim DE WAELE and Patrick DE BAETS

Department of electrical energy, systems and automation, Ghent University

Abstract

Connection techniques such as lap joints, dovetail connections, spline connections, shaft connections, *etc.* can fail prematurely due to fretting fatigue. Understanding the fretting fatigue phenomenon and increasing the lifetime is needed and important for the concerning industries. This paper presents the experimental work to study the influence of residual compressive stress as a palliative for fretting fatigue. Two series of fretting fatigue experiments are performed: one baseline series with a virgin surface finish and one series with residual compressive stresses at the surface. The series with the residual compressive stress shows an significantly increased lifetime compared to the virgin series.

Keywords

Fretting fatigue, lifetime, palliative, residual compressive stresses, deep rolling

1. Introduction

The research field of fretting fatigue deals with the simultaneous interaction of the tribological fretting phenomenon and the mechanical fatigue phenomenon. Fretting fatigue failures are frequently seen in connection techniques which are dynamically loaded, see Fig. 1. Typical applications are bolted and riveted lap joints (Chakherlou, 2009), dovetail connections (Kermanpur, 2008), splined connections (Madge, 2008), shaft-hub connections (Großmann, 2007), *etc*.

To increase the lifetime of applications suffering fretting fatigue, palliatives can be applied. Palliatives can be classified on their acting mechanism: reducing coefficient of friction, increasing surface hardness, introducing residual compressive stresses, altering surface chemistry, altering surface topography. In this paper, the authors will focus on the introduction of residual compressive stresses at the surface. The residual compressive stresses at the surface of the material counteract the high tensile stresses at the surface due to fretting fatigue, see Fig. 2. The total stress state at the surface is hereby reduced, causing a slower crack initiation and a higher total lifetime.
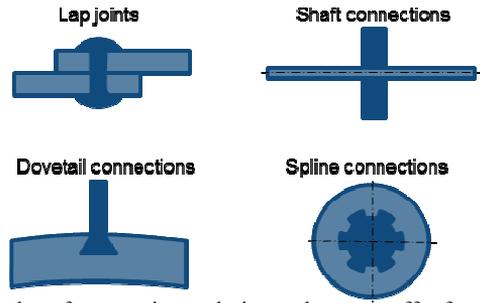
Figure 1. Examples of connection techniques that can suffer from fretting fatigue.
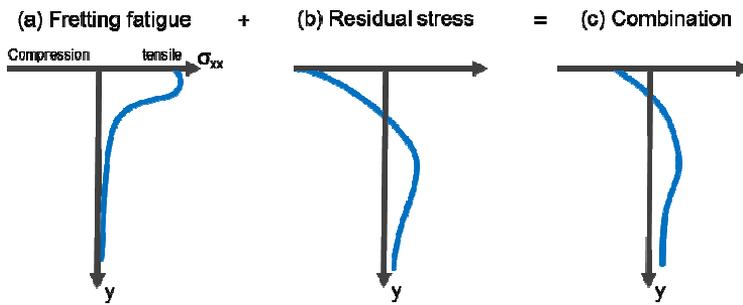
Figure 2. Typical stress distribution centrally under the contact:
(a) fretting fatigue contact, (b) residual compressive stress and
(c) combination of both.

2. Test samples

A fretting fatigue experiment is performed with one dogbone specimen and two identical indenter specimens - named pads. The geometry and the dimensions of the two types of specimens are given in *Fig*. 3. The dogbone specimen is flat and has a narrowed rectangular cross section of 10 x 4 mm². The pads are also flat and have an end side which is cylindrical with a radius of 50 mm. The roughness R_a on the surfaces where the contact should be is lower than 0.3 µm. The roughness R_a of the virgin surfaces is measured in longitudinal direction and is in the range of 0.24 ± 0.04 µm.
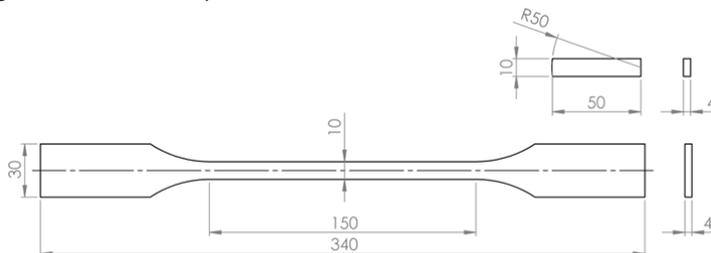
Figure 3. Fretting fatigue specimens geometry. Top: fretting pad; bottom: dogbone specimen.

All the tested specimens are milled out of one single sheet of aluminium, each in the rolling direction. The used aluminium 2024 T3 has a tensile strength σ_{UTS} of 506 ± 9 MPa and a yield strength σ_y of 383 ± 5 MPa. The average grain size is calculated according to the ASTM standard E112 and is 170 ± 83.2 µm. The material hardness is measured with a Leco vickers hardness tester. The hardness is measured at the middle thickness of the plates and is 139.37 ± 1.78 HV5.
Two different types of dogbones are used: one with a virgin surface finish and one where a residual compressive stress is applied at the surface. Introducing residual compressive stresses at the surface is one of the fretting fatigue palliative mechanisms. The residual compressive stresses will temper the high tensile stresses in a fretting fatigue contact, reducing the likelihood and speed of crack initiation and thus increase the lifetime.

Introducing residual compressive stresses at the surface is done by deep rolling. Deep rolling is a typical finishing step in the rolling sequence similar to a finishing pass or a skin pass. Deep rolling is a type of cold rolling with the emphasis at the introduction of a compressive residuals stress gradient more than just a thickness reduction. The deep rolling treatment is applied on the dogbone specimen at the locations of contact between the specimen and the pad. The deep rolled areas are 4 x 35 mm. The deep rolling process is repeated two times with equal normal force. The dogbone specimens are rolled with a rolling force of 2.77 kN and a roller diameter of 50 mm. The average Hertzian contact pressure between the specimen and the roller is 570 MPa.

3. Experimental setup

The fretting fatigue test set-up at Soete laboratory is based on a universal testing machine (UTM) to which a fretting fixture is mounted, see Fig.4. The UTM consists of a load frame (ESH testing) with one hydraulic actuator. The hydraulic cylinder is a dynamic through rod piston and is instrumented with a 100 kN loadcell and a displacement sensor. The actuator is controlled with a standalone MTS Flextest controller which also serves as data acquisition system. The test rig is powered by a hydraulic aggregate.

On the UTM is a fretting fixture installed to obtain a fretting fatigue test rig of the type 'single actuator test rig with adjustable compliance'. The fretting fixture is schematically shown in Fig 5. The fixture is used to clamp the pads (7), control the normal force F_N and generate the tangential force F_T. The fretting fixture consists of four sub-assemblies. First, the fretting fixture base. Second, the normal loading system. Third, the tangential loading system. And last, the pad holders.

The fretting fixture base stiffly connects the fretting fixture to the load frame. The base consists of two horizontal supports (1) and one base plate (2).

The normal loading system is designed to apply the normal load F_N to the pad(holders). Two opposite and equal forces are required for a fretting fatigue

experiment. This is achieved by using one hydraulic actuator (11) and a C-beam construction (4).

The third function of the fretting fixture is to generate the tangential force F_T. The fatigue force elongates the dogbone specimen and tangentially moves the line contact. As a result, the pads and pad holders move simultaneously since the contacts are in mixed stick slip regime i.e. without global slip. The pad holders displace one side of the leaf springs while the other side of the leaf springs is connected to the base plate. The deformation of the leaf springs generates the tangential reaction force F_T. It is clear that the generated tangential force and the applied fatigue force are proportional and in phase to each other. Also, during an experiment it is impossible to alter the ratio of tangential to fatigue force. However, the ratio can be altered by changing the stiffness of the leaf springs prior to an experiment.

The fourth and last function of the fretting fixture is to clamp a pad and initiate the normal and tangential forces in an appropriate way. This function is realised by the pad holder (6).
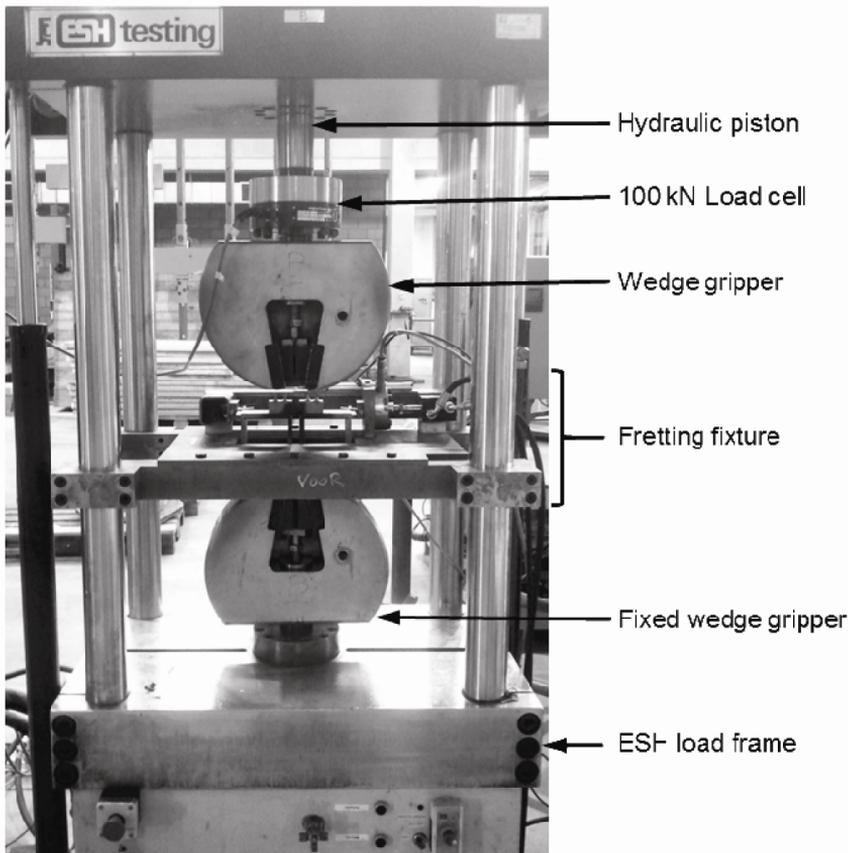

Figure 4. Overview of the fretting fatigue test rig.
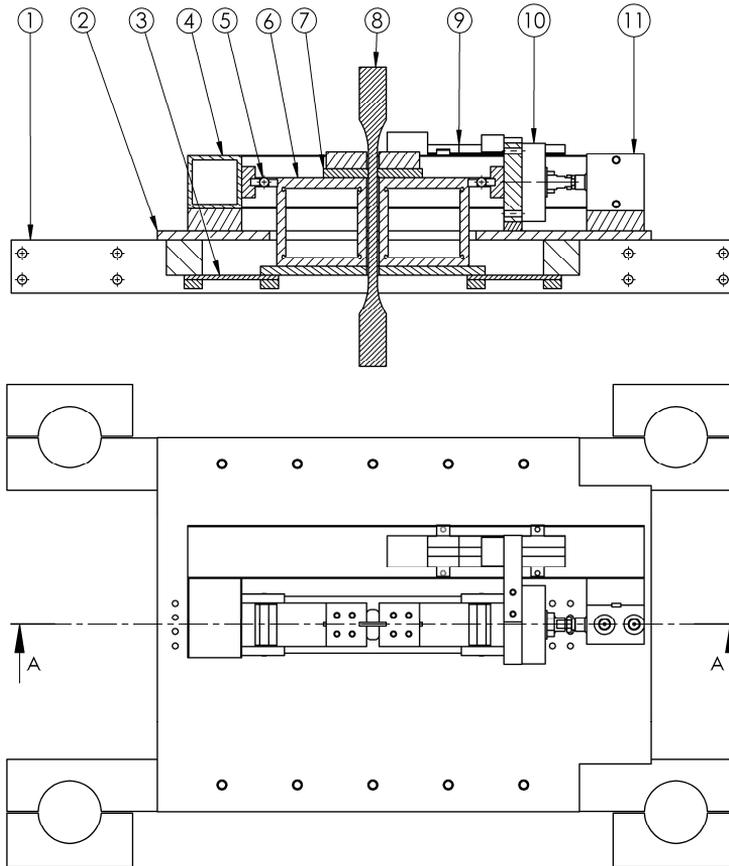
Figure 5. Section view and top view of the fretting fixture.
1. horizontal support, 2. base plate, 3. leaf springs, 4. C-beam, 5. roller bearing, 6. pad holder, 7. pad, 8. dogbone specimen, 9. displacement sensor, 10. load cell, 11. hydraulic actuator.

4. Test results

Eleven fretting fatigue experiments are conducted on coupon scale specimens with a virgin surface, see Table 1. The normal force is maintained constant at 543 N for all the experiments. The applied maximum fatigue force varies between 4 and 8.8 kN and the load ratio is kept at 0.1. All the experiments failed due to fretting fatigue. The dogbone specimen is broken in two parts at the location of contact with the pads.

Six fretting fatigue experiments are conducted on coupon scale specimens with a residual compressive stress, see Table 1. The normal force is maintained constant at 543 N for all the experiments. The applied maximum fatigue force varies between 4.6 and 8.8 kN and the load ratio is kept at 0.1. Five of the six experiments failed due to fretting fatigue, one experiment (at the lowest fatigue force) did not fail after three million cycles.

Surface damage is seen on the dogbone specimen and the pads at the location of contact and its proximity. A representative view of post mortem damage is shown in Fig. 6. The corresponding calculated local slip distribution (using finite element simulations) for the presented images is shown in Fig. 6, right. The damage pattern on the dogbone and the pad are almost identical which makes sense since they are generated together (damage on the following pad and dogbone specimen pictures are each other's mirror image). The damage pattern can be divided in four horizontal areas, reaching from the left hand side to the right hand side of the specimens.

The first area is a narrow strip at the edge of the contact located at the side of the fixed clamping (bottom side in Fig. 6.). In the area is a tiny amount of black oxidized aluminium particles found. Also, very short abrasion marks (< 1 µm) are observed in tangential (vertical) direction. From this one can conclude that in this area there has been a very small reciprocating slip between the surfaces. This corresponds with the mixed stick slip contact theory: at the remote side of the applied force is the smallest slip amplitude found.

The second area is adjacent to the first area. The surface topography is different from the initial surface but no accumulation of aluminium oxidized particles is seen. The original line pattern (from manufacturing) is transformed to an area with plastically deformed asperities. No abrasion marks are observed. In this area, the surfaces where sticking to each other (i.e. no slip) which is in line with the contact theory. The normal contact pressure (69 MPa < p(x) < 190 MPa) was everywhere in the area high enough to plastically deform the asperities.

The third area is positioned next to the second area and just like the first area characterised by accumulated debris particles and tangential abrasion marks. The main difference with the first area is the size. The third area shows considerably more debris accumulation, is significantly wider and displays longer abrasion marks compared to the first area. This is again in correspondence with the mixed stick slip contact theory. The width of the local slip area is wider and the slip amplitude is higher compared to the first area. In the transition of the second to the third area initiates the governing crack in the dogbone specimen which causes the latter to fail.

The fourth and last area is not directly related to the mixed stick slip contact condition but arises at the time of fracture. The forth area is adjacent to the third area at the side of the applied fatigue load. The area has a different aspect on the pad and specimen. On the pad are multiple deep and long abrasion marks seen in tangential (vertical) direction. On the dogbone specimen is the fourth area much narrower and less pronounced. The abrasion marks are the result of gross sliding between the (upper side of the) specimen and the stationary pad. After fracture of the dogbone specimen the upper part of the specimen moves upwards. During this large displacement is abrasion caused between the stationary pad (causing longer marks) and the moving dogbone (causing shorter marks).

The damage pattern is similar for the virgin samples and the samples where residual compressive stress is applied at the surface.
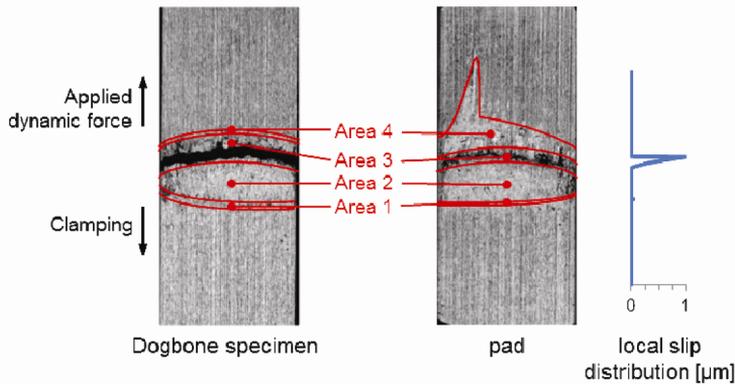
Figure 6. Different surface damage areas on a virgin dogbone
specimen and pad (σ_{fat} = 220 MPa).

The fracture surface of a typical coupon scale fretting fatigue experiment is shown in Fig. 7. The fracture surface can be divided in three areas. On the right hand side of Fig.7. is a large area of fatigue crack propagation seen. At the left hand side is a small crack propagation area seen. In between is a typical residual tensile fracture observed. The major crack propagated from a line contact at the right hand edge of the specimen. The crack initiated as a few small cracks which conglomerated and propagated as one major fatigue crack. At the right hand side of the specimen the crack covers the complete width of the specimen (= 4 mm). The crack is visible at both edges. More towards the middle of the specimen grows the crack only at the centre of the specimen, and is the crack tip not visible at the sides of the specimen. The crack shape is semi elliptical and grows more in depth than through width because of the triaxial stress state (Brickstad, 2000). In addition to the major crack propagation area is also a small crack propagation area observed, see Fig.7 left. The fracture pattern is similar for the virgin samples and the samples where residual compressive stress is applied at the surface.
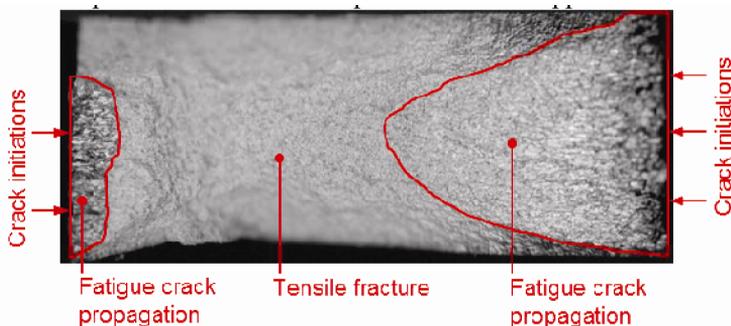

Figure 7. Typical fracture surface after fretting fatigue failure
of a dogbone specimen.

Table 1. Experimental data of the coupon scale fretting fatigue experiments

Surface	Max force F_{fat} [kN]	Max. stress [MPa]	F_N [N]	F_T [N]	Lifetime [-]	Remark
Virgin	8.8	220	543	267.2	99607	
Virgin	8.8	220	543	317.8	86647	
Virgin	8.2	205	543	269.1	114645	
Virgin	7.6	190	543	241.5	141890	
Virgin	7.6	190	543	220.4	113699	
Virgin	7.0	175	543	195.1	186050	
Virgin	6.4	160	543	193.7	245690	
Virgin	5.4	135	543	223.7	358082	
Virgin	5.4	135	543	195.6	419919	
Virgin	4.6	115	543	186.3	1105245	
Virgin	4.0	100	543	155.2	1407257	
Deep rolled	8.8	220	543	271.9	165370	
Deep rolled	8.8	220	543	257.5	135700	
Deep rolled	8.2	205	543	237.0	164023	
Deep rolled	6.4	160	543	201.1	595484	
Deep rolled	5.4	135	543	168.8	597897	
Deep rolled	4.6	115	543	155.4	3000000	Not failed

Conclusions

In this paper, the influence of residual compressive stresses on the fretting fatigue
lifetime is studied. Eleven fretting fatigue experiments are performed on
specimens with a virgin surface. Six fretting fatigue experiments are performed
with a residual compressive stress. The post mortem damage pattern is similar for
both types of samples. However, a notable and significant difference is found in
the measured high cycle fatigue lifetime. The deep rolled specimens have a higher
lifetime compared to the virgin specimens. The degree of improvement increases
with increasing number of cycles to failure. At the lowest applied fatigue stress
($\sigma_{fat} = 115$ MPa) is the improvement more than a factor 2.7. Optimising the
magnitude and profile of the residual compressive stress at the surface is beyond
the scope of this work but might further improve the fretting fatigue lifetime.

Nomenclature

F   Force   N

Greek letters
σ   stress   MPa
Subscripts
N   Normal
T   Tangential
fat   Fatigue
UTS   Ultimate tensile stress
y   Yield

Acknowledgements

References

[1] Chakherlou, T.N (2009), Experimental and numerical investigations into the effect of an interference fit on the fatigue life of double shear lap joints, Engineering Failure Analysis, Vol. 16(7), pp. 2066-80
[2] Kermanpur, A. (2008), Failure analysis of Ti6Al4V gas turbine compressor blades, Engineering Failure Analysis. Vol. 15(8), pp. 1052-64.2008
[3] Madge, J.J. (2008), Numerical Modelling of the Effect of Fretting Wear on Fretting Fatigue, Nottingham
[4] Großmann, C. (2007), Fretting Fatigue of Shape Optimised Polygon-Shaft-Hub Connections, Berlin
[5] Brickstad, B.r. (2000), Crack shape developments for LBB applications. Engineering Fracture Mechanics. Vol. 67(6): pp. 625-46

E-maintenance - a new trend in
industrial maintenance

Nicolae UNGUREANU, Claudiu LUNG, Radu COTEȚIU

Faculty of Engineering, North Universitary Center of Baia Mare
Technical University of Cluj Napoca

Abstract

In this paper we present a series of theoretical concepts needed to implement a new system of industrial maintenance, the e-maintenance system. It is presented the positioning of the new system compared to conventional maintenance systems and what brings new the e-maintenance system. It also presents a series of equipment needed to implement this system. Finally the paper presents the advantages and disadvantages of the e-maintenance system.

Keywords

e-maintenance, monitoring, sensors

1. Introduction

The maintenance is one of the oldest human activities. In theory the maintenance is defined as the actions necessary for retaining or restoring a piece of equipment, machine, or system to the specified operable condition to achieve its maximum useful life, when the maintenance actions are performed in logistic conditions defined. For maximum efficiency the maintenance actions and the related logistics support are structured in maintenance systems.

The main scopes of the maintenance systems is to keeping the machine functionality at the required level, maximizing the machine capacity and enhancing the machine live-time. The maintenance systems are based on the logical organization of the works according to several criteria:
- criterion of the resources used;
- criterion of the use of the means for automatic data processing;
- criterion of the cost reduction for maintenance, repairs and storage;
- criterion of the necessity of eliminating the accidental stoppage by preventing some damages, mistuning, permanent wear, etc.

At this time the Romanian industry, and not only, use some maintenance systems that can be illustrated as in figure 1 and time evolution of the maintenance system is shown in figure 2.

Each of the mentioned maintenance systems have advantages or disadvantages that make them preferred for each industrial enterprise. It is also

possible the use of different maintenance systems, simultaneous, in a single enterprise, in order to get the full benefits of different maintenance systems.
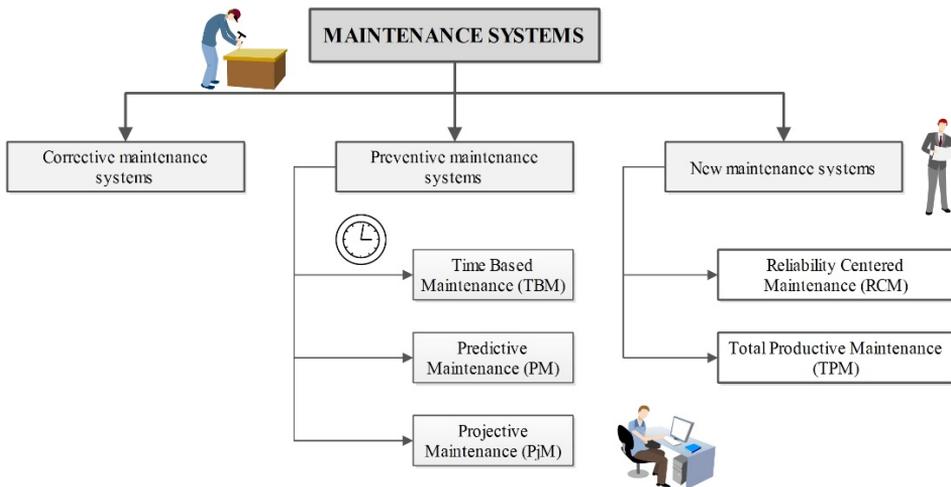
Figure 1. Maintenance systems used in industry
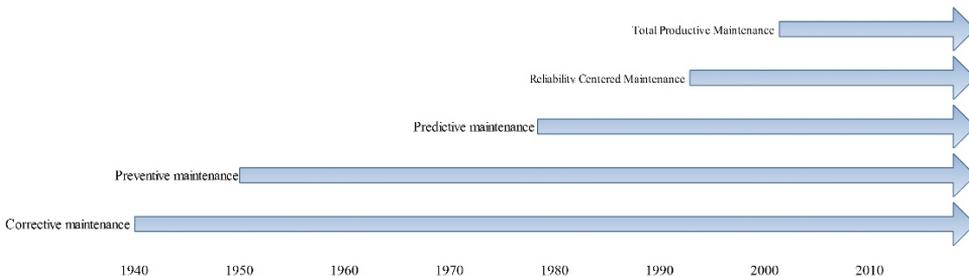
Figure 2. Evolution of maintenance systems

2. Prerequisites for implementation of e-maintenance

The e-maintenance system is from category of modern maintenance systems that are based on the use of new technologies. Unlike other maintenance systems, the e-maintenance system implementation requires a number of preconditions. The fewest preconditions are for new plants or technology or new equipment lines who are already prepared for this step and refers specifically to the training of personnel involved. In contrast for industrial companies that have already implemented other maintenance systems the transition to e-maintenance is more difficult and involves the preparatory stages.

For example a precondition for implementing the e-maintenance is to implement before a system of monitoring the equipment and machines. Monitoring is the activity of surveillance of machines and tools, periodic or

permanent, in order to control the operation, to avoid failures, to analyze the systems and, in the end, to draw up a diagnosis of the system. In its turn, the diagnosis will help to draw up the maintenance strategy, to establish the deadlines, to establish the places of intervention and the size of the intervention. The aims of the monitoring can be structured as follows:
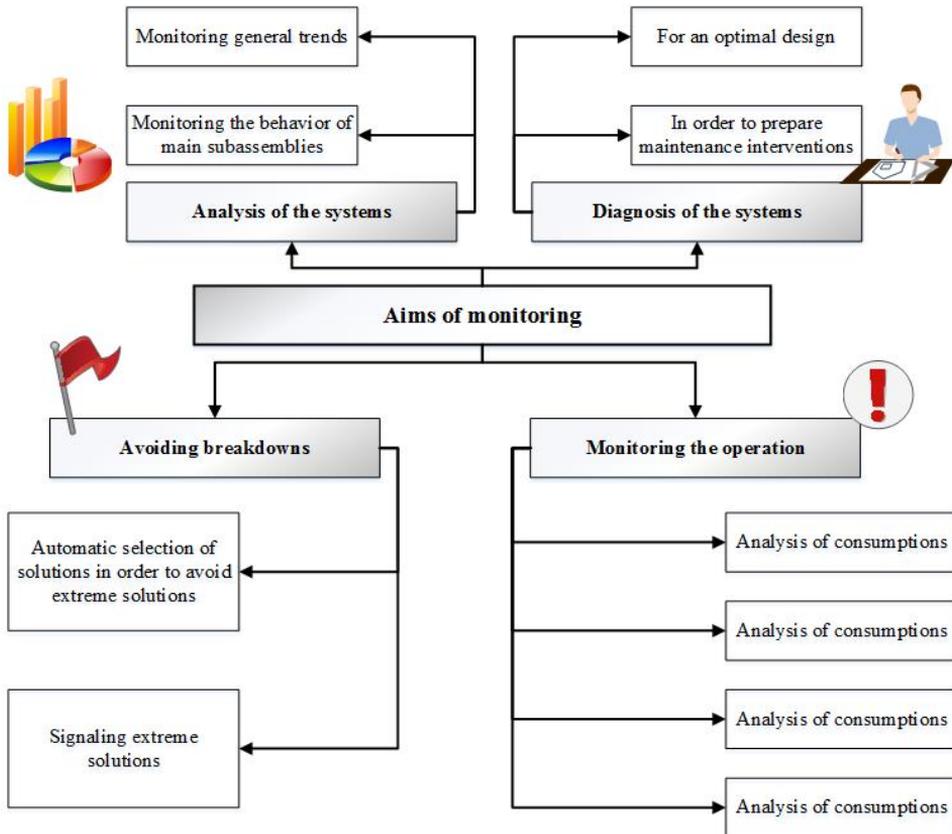
Figure 3. Aims of monitoring

Fault detection and localization of fault of machines and equipment using continuous monitoring method is essentially based on the existence of a number of sensors and transducers to monitor parameters that describe the system.

Each of these sensors or transducers compares the received signal with a threshold signal (upper or lower) for parameter monitored. All overruns are reported to a human operator or are sent to a block decision.

The advantage of the method is that of the permanent control over the system. The main disadvantage consists in the great number of sensors and transducers, a number which increases exponentially with the linear increase of the parameters monitored.

The method of fault detection and localization using the method of periodical monitoring is based on the existence of multiple possibilities of mounting some portable transducers and sensors within the system.

Whichever method of monitoring, continuously or periodically, the system relies on sensors.

A second phase is to implement a predictive maintenance system, the system shown in figure 4.
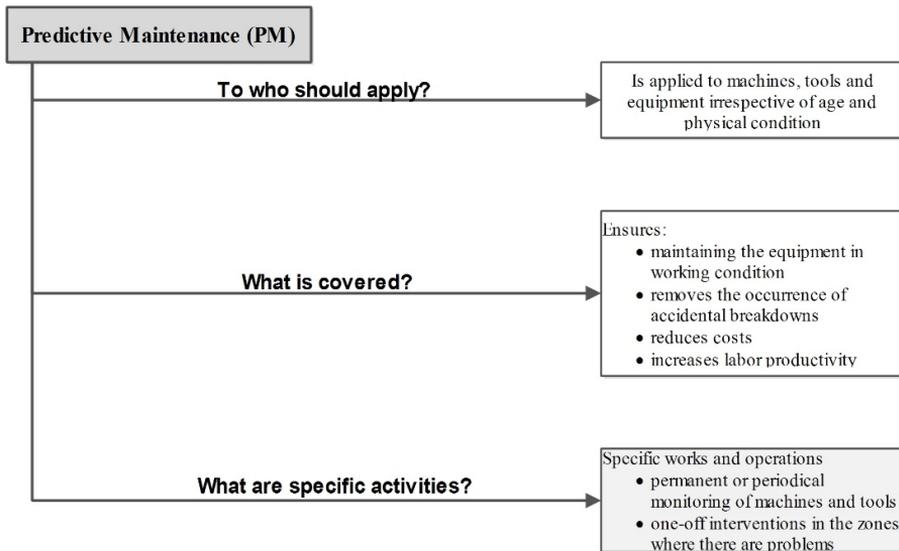

Figure 4. The predictive maintenance system

3. The e-maintenance system

E-maintenance system can be considered as a development in maintenance area of the concept of aided computer. Main goal to the development of computer assisted maintenance activities is to select the most appropriate automated system, the sensors and to implement the most suitable control algorithm. The designing of an error-free maintenance system needs to have an appreciation for the functional limits of the equipment and the ability of sensors to provide usable information's in a wide conditions area, since these parameters will constrain the range of possible systems configurations designs. These values, provided by sensors, must be compatible with the equipment and the control systems and it's recommended to be appropriate for the particular factory.

A detection system for automated manufacturing lines must be considered regarding to the manufacturing strategy, as part of this strategy. The process of development of an intelligent, flexible automatic production line, must to be able to combine the automated diagnostics systems with a network of sensors, in order to handle machinery maintenance and process control functions.

Automated diagnostics systems relies on „a priori" and „posteriori" information's. „A priori" information is considered any previously relationship or fact that the system can use to make a diagnosis. The information regarding the problem for which diagnosis will be made is considered „posteriori" information. The first stage in the collecting data process is to use sensors and transducers to convert physicals sizes into electrical signals. Electrical signal will be processed in an appropriate form suitable for analysis, including connections and correlation with other information and trending. Resulting information's can be used in a deductive process witch lead to the fault diagnosis.

Starting from the idea that an automated diagnostics system is necessary, the required sensors must be mounted at their monitoring place, permanently. In some cases, if many sites must be monitored and data are not required in a continuous flux, it may be possible to use these sensors or transducers in many locations, sequentially. An automatic diagnostics robot is the most eloquent example, well-suited to collect data from many points, using a limited numbers of sensors. This new feature extend the applications domain of robots, from a simply work pieces movers used only for production into a robot capable to perform production activities combined with diagnostic inspection.

Sensors and transducers are used in various applications, starting from data collecting to complex data acquisition and process control systems. They are classified in two major categories: active sensors and passive sensors. A passive sensor does not require power supply, all the energy that he delivers to the next stage is taken from the measured circuit. An active sensor acts as a modulator and can deliver to the next stage more energy compared with a passive sensor. If the sensor use a DC power supply, the output is modulated at same frequency by measured and if the sensors use an AC power supply, the output is a signal with the carrier frequency with sidebands.

Another sensors classification is in accordance with the physical phenomenon that must be detected and measured. Some common examples are: voltage, current, pressure or displacement. Many sensors are developed for some specific applications with specific requirements.

One of the most measured parameter in automated diagnostics systems is temperature, because a large numbers of functional and physical parameters are closely related to the temperature variation. Some examples of temperature sensors are: thermistors, thermocouples, integrated circuit temperature sensors (AD590, AD592) or radiation sensors. Thermistors are resistors with thermally sensitive properties that are able to exhibit a large, predictable and precise change in electrical resistance when are changes in his body temperature. Negative Temperature Coefficient (NTC) thermistors decrease in electrical resistance when the temperature increase and Positive Temperature Coefficient (PTC) thermistors increase their electrical resistance when the temperature increase. A thermocouple is a device containing two dissimilar conductors or semiconductors connected in one ore multiple points. This sensor produces a voltage when the temperature differs in contact point, this process is known as

the thermoelectric effect. Thermocouples are a widely used as temperature sensor in various applications.

Another parameter that is frequently measured is the pressure. The pressure can be defined as a force applied per a unit area that a fluid exerts on its surroundings. The pressure measurement can be done in a static or dynamic way. The pressure measured where no motion is occurring is associated as static pressure. When the motion of a fluid changes the force applied to its surroundings, measurement is known as dynamic pressure measurement.

An accelerometer is a device that can measure the proper acceleration. Accelerometers are used in multiple industrial applications and science. Some applications for highly sensitive accelerometers are in inertial navigation systems for aircraft or missiles. Some accelerometers are used in projects that aim to detect vibration in rotating machinery. Also the accelerometers are more and more used in phones, tablet computers and digital cameras. Single and multi-axis accelerometers permits to detect the magnitude and direction of the proper acceleration, as a vector quantity, and therefore they can be used to sense orientation, vibration, coordinate acceleration, shock or falling.

Data collected from sensors are in generally used for further processing and they must be stored. In some application they are stored locally on data acquisition system, known as data logger. A data logger is an electronic device that is able to records data along a time period from a sensor or via external instruments and sensors. The new technology are based on a digital processor with internal memory for data storage, therefor they are small, battery powered and portable. Some data loggers can be interfaced with a personal computer witch can be used to activate the data logger module and process, view and analyze the collected data, while others are equipped with a local interface device and can be used as a stand-alone portable device. In figure 5 is presented a data logger implemented by using an Arduino microcontroller development board.
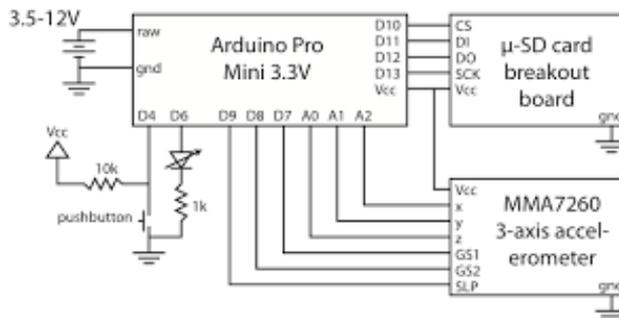

Figure 5. Arduino data logger

The new data transmission technology provides the infrastructure for a large amount of data transfer to a dedicated server, using LAN or WiFi connections.

Data stored on these servers can be accessed by using o local interface or via a WEB interface. In figure 6 is presented the data view in a local interface.

Figure 6. Local interface for data view

Figure 7 represent the possibility to generate some reports based on stored data and to view the results on a WEB page.
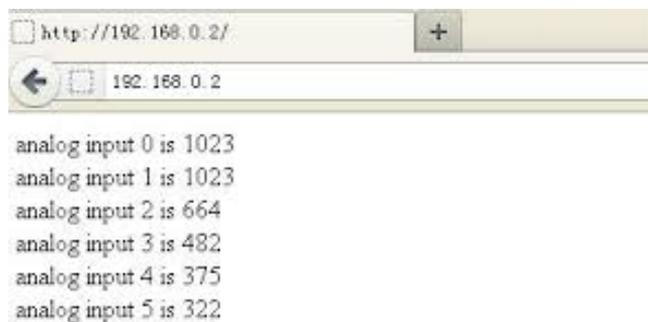
Figure 7. WEB page interface for data view

The difference between e-maintenance system and predictive system begins to manifest at this time. In predictive system the human factor decides the following actions and the maintenance actions are implemented by maintenance personnel. In e-maintenance system the actions are automatically selected by specialized software and the maintenance actions are carried out by automated systems designed and made together with manufacturing equipment.

Conclusion

At the moment e-maintenance system is still in its early stage. Implementation encounters a series of difficulties related primarily to the high cost of sensors,

the lack of complete and complex diagnostic software, the need to complement
the production functions of equipment's and machines with automatic
adjustment functions and repair itself. Besides these difficulties should be
referred the difficulties with lack of qualified personnel and even difficulties
referred to mentality. But the obvious more advantages, some of them proven by
predictive maintenance system, will eventually lead to system expansion and its
widespread application, taking advantage of the favorable factors such as
expansion of WiFi or LAN.

Some of these advantages can be mentioned:
- eliminating accidental malfunctions;
- decrease maintenance costs by eliminating the defects Grade II;
- lower personnel costs;
- reducing intervention time;

References

[1] H. Rosemary Taykor, Data acquisition for sensor systems, Chapman & Hall,
ISBN: 0-412-78560-9, 1997
[2] Holger Karl, Andreas Willig, Protocoale si arhitecturi pentru retele de
senzori wireless, Matrix Rom, Bucuresti,ISBN:978-973-755-802-2, 2012
[3] Ryoji Ohba, Intelligent sensor technology, John Wiley & Sons, ISBN0-471-
93423-2,
[4] Sebrie Soloman, Sensors handbooks, McGraw-Hill Handbooks, ISBN: 0-07-
059630-1, 1998
[5] Ungureanu N. S., Duval P., Mocan M., Tăucean I., (2004), Logistica
activităților de mentenanță, Editura Universității de Nord Baia Mare, ISBN
978-606-536-074-7
[6] Ungureanu N., Ungureanu M., System of Predictive Maintenance,
International Multidisciplinary Conference, 11th edition, 19-21 may, 2015,
Baia Mare – Nyiregyhaza, Romania – Hungary
[7] Ungureanu, M., A model for product inovation project, 2014 International
Conference On Production Research - Regional Conference Africa, Europe
And The Middle East And 3rd International Conference On Quality And
Innovation In Engineering And Management (ICPR-AEM 2014) Pages: 489-
492 Published: 2014,

NPIII and cold atmospheric plasma surface modification of polymers

Gábor KALÁCSKA[1], Zoltán KÁROLY[2], Szilvia KLÉBERT[2],
Róbert KERESZTES[1]

[1]Institute for Mechanical Engineering Technology, Szent István University, Gödöllő,
[2]Institute of Materials and Environmental Chemistry,
Research Centre for Natural Sciences, HAS

Abstract

Formerly we have tested two different engineering polymers (PETP and PA6) plasma immersion ion implantation (PIII or PI3, called also plasma-based ion implantation). We found for the N PIII-treated PETP a gradual formation of amorphous hydrogenated carbon-nitride, increased surface wettability, decreased dry friction coefficient at a very low Pv factor (0.0075 MPa m s-1), but increased friction coefficients at higher Pv factors (about 0.1 MPa m s-1), suggesting an increased adhesion component of friction. Very similar results were discovered for PA6 as it was already published. Concerning the industrial interests of modified polymer surfaces e.g. adhesive bonding of plastic machine elements, a new research project – OTKA K 113039 – was launched to examine the effect of cold atmospheric plasma treatment on various polymer surfaces. This article gives a brief comparison about the two different plasma technologies.

Keywords

plasmas, NPIII, atmospheric, cold plasma, DBD

1 Introduction, plasmas

Plasmas are chemically active media. Depending on the way they are activated and their working power, they can generate low or very high „temperatures" and are referred correspondingly as cold or thermal plasmas. This wide temperature range enables various applications for plasma technologies: surface coatings, waste destruction, gas treatments, chemical synthesis, machining [1].

Plasma is a more or less ionized gas. It is the fourth state of matter and constitutes more than 99% of the universe. It consists of electrons, ions and neutrals which are in fundamental and excited states. From a macroscopic point of view, plasma is electrically neutral. However, it contains free charge carriers and is electrically conductive [2, 3]. The ionization degree can vary from 100% (fully ionized gases) to very low values (e.g. 10-4–10-6; partially ionized gases). The plasma state is often referred to as the fourth state of matter. [4] Much of the

visible matter in the universe is in the plasma state. This is true because stars, as well as all visible interstellar matter, are in the plasma state. Besides the astroplasmas, which are omnipresent in the universe, we can also distinguish two main groups of laboratory plasmas, i.e. the high-temperature or fusion plasmas, and the so-called low-temperature plasmas or gas discharges [5].

In general [1], a subdivision can be made between plasmas which are in thermal equilibrium and those which are not in thermal equilibrium. Thermal equilibrium implies that the temperature of all species (electrons, ions, neutral species) is the same. This is, for example, true for stars, as well as for fusion plasmas. High temperatures are required to form these equilibrium plasmas, typically ranging from 4.000 K (for easy-to-ionize elements, such as cesium) to 20.000 K (for hard to-ionize elements, like helium).

Often, the term 'local thermal equilibrium' (LTE) is used, which implies that the temperatures of all plasma species are the same in localized areas in the plasma. On the other hand, interstellar plasma matter is typically not in thermal equilibrium, also called 'non-LTE' [2]. This means that the temperatures of the different plasma species are not the same; more precisely, that the electrons are characterized by much higher temperatures than the heavy particles (ions, atoms, molecules). The subdivision (LTE and non-LTE plasmas) is typically related to the pressure in the plasma. Indeed, a high gas pressure implies many collisions in the plasma (i.e. a short collision mean free path, compared to the discharge length), leading to an efficient energy exchange between the plasma species, and hence, equal temperatures. A low gas pressure, on the other hand, results in only a few collisions in the plasma (i.e. a long collision mean free path compared to the discharge length), and consequently, different temperatures of the plasma species due to inefficient energy transfer. There are some exceptions to this rule, e.g. dielectric barrier discharges or atmospheric pressure glow discharges.

2. PIII (Plasma-immersion ion implantation) Treatment of polymer surfaces

The process of ion implantation causes the injection of an energetic ion beam into a material, changing herewith the atomic composition and structure, and hence the properties, of the material surface layer (fig.1).

Conventional ion implantation is carried out in a vacuum chamber, where an ion source is used to create an intense ion beam of the species to be implanted. The ion beam has to be focused and accelerated by a potential difference of several tens to hundreds of kV, which makes this technique mechanically complex and expensive [1]

In plasma-immersion ion implantation (PIII), also called plasma source ion implantation (PSII), a number of steps required in the conventional method can be removed, such as beam extraction, focussing and scanning over the target material. Instead, the target material is 'immersed' in a plasma, and the ions are directly extracted from the plasma and accelerated toward the target by a number of negative high voltage pulses.
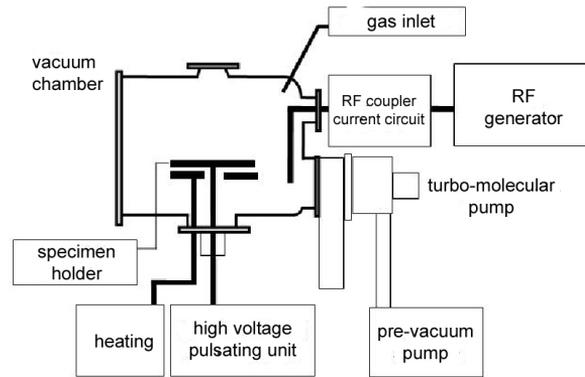
Figure 1. Schematic of PIII process [6, 7]

PIII has become a routine process in the semiconductor industry, mainly for doping of the targets. In order to obtain high implantation fluxes at low pressure, ECR sources are mostly used (typically at 2.45 GHz and a pressure of 0.1 Pa or lower). Moreover, this technology is also gaining increasing interest in the metallurgical industry, to make new surface alloys with enhanced hardness as well as corrosion and wear resistance.

A large number of scientific papers appeared on PIII-treated polymers during the last 15 years [8, 9, 10, 11, 12]. The research in this area focused mainly on the chemical, mechanical and morphological properties of PIII-treated polymer surfaces, but properties including wettability and medical applicability were also investigated [13].

In our previous research we paid special attention of surface chemical changes, surface energy and tribological behaviour of nitrogen plasma immersion ion implantation (NPIII). As earlier we published the detailed research [13, 14] results, our main conclusions were as follow:

PA6 measurements
The effect of N PIII of PA6 on its sliding properties against low carbon structural steel S235 was studied. The surface changes were characterised by XPS, contact angle measurements and optical microscopy, while alterations in the sliding properties including friction coefficient, wear and temperature close to contact were studied by a pin-on-disc tribometer under dry and variously lubricated conditions.
- The N-content of the surface layer increased, while those of C and O decreased upon N PIII treatment.
- The contact angles decreased and the total surface energy and its polar and dispersive components increased significantly.
- Under dry sliding in the low Pv regime, the friction coefficient of the treated sample started from a value lower than that of the untreated version and the corresponding specific wear rate was also smaller.

– Under dry sliding, the increased surface energy caused increased adhesion of the treated PA6, associated with the formation of a transfer layer on the steel disc (fig.2).

– Water lubrication was more efficient – in accordance with the increased polar component of surface energy – for the treated PA6 than found earlier for PETP.

– For the treated PA6, a decreased friction was observed upon run-out type lubrication test with gearbox oil, due to increased retention of oil on the treated surface characterised by an increased dispersive component of the surface free energy.
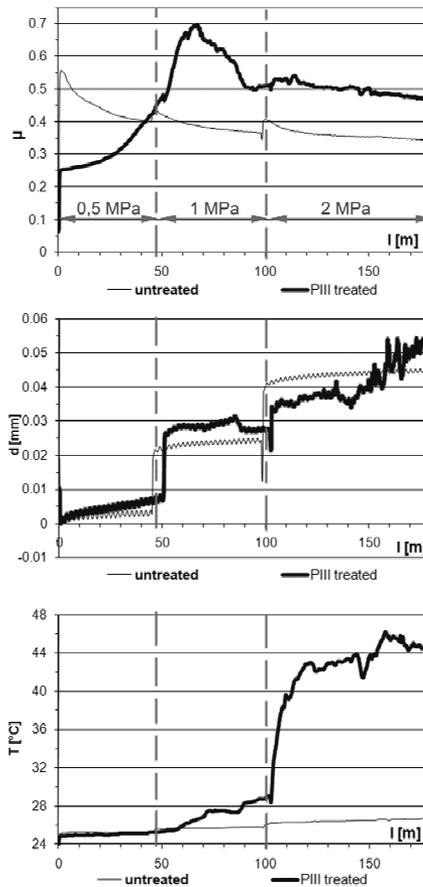

Figure 2. Results of comparative pin-on-disc test, performed under dry conditions (v=0.05 m s^{-1}). [13] (Top: friction coefficient - μ, middle: wear plus deformation - d, bottom: contact temperature - T)

PETP measurements

– XPS results suggested the evolution of surface composition and bonding towards those of amorphous hydrogenated carbon-nitride.

– Water contact-angle decreased implying increased surface wettability.
– At a very low *Pv* factor (0.0075 MPa m s^{-1}) for the nitrogen PIII-treated
   PETP the dry friction coefficient was smaller (fig3.) than, while the
   lubricated friction coefficient was similar to the corresponding value of
   the untreated variant.
– At higher *Pv* factors (near 0.1 MPa m s^{-1}), however, both the dry and
   lubricated friction coefficients were higher for the treated sample than
   for the untreated variant, suggesting an increased adhesion component of
   friction for the nitrogen PIII-treated PETP in this region.
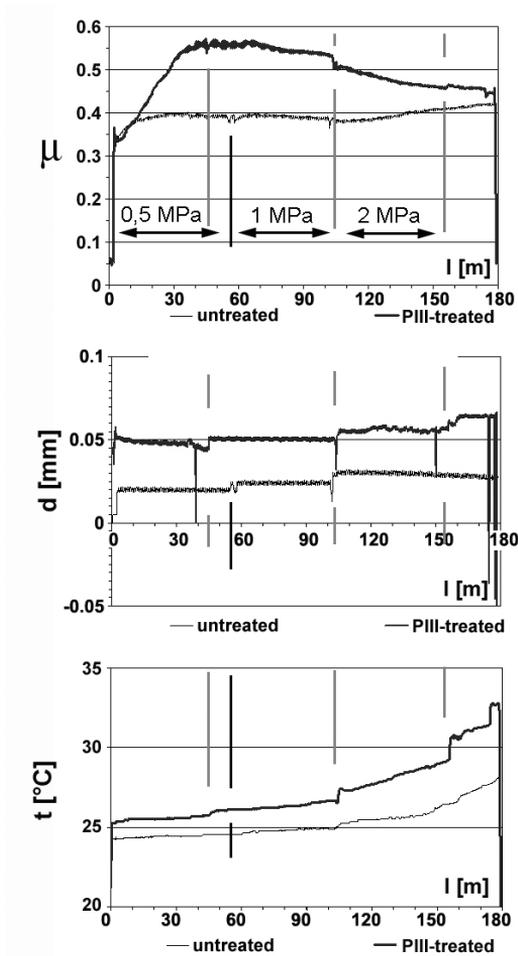

Figure 3. Tribological properties of dry untreated and PIII-treated PETP
as a function of sliding distance (P=0.5, 1 and 2 MPa, v=0.05 m s-1) [14]

Taking those valuable results into account we have decided to examine the
surface effects of atmospheric cold plasma on numerous polymeric surfaces. The
presently targeted material groups:

- UHMW-PE HD 1000, PP, PTFE
- PA6, PETP, POM C, PEEK

Those engineering plastics have different applications regarding the two groups. While the first materials are involved in packaging and sealing applications the latter ones are subjected of severe load and tribological conditions.

3. Atmospheric cold plasma for polymer surface treatment

Atmospheric pressure gas discharge plasmas, especially those operated at energy non-equilibrium (non-LTE) and low gas temperatures, have recently become a subject of great interest for a wide variety of technologies including surface treatment. [15] Depending on required applications, there are a wide variety of plasmas generated under different conditions. One of the most important characteristics is the gas pressure (fig.4)
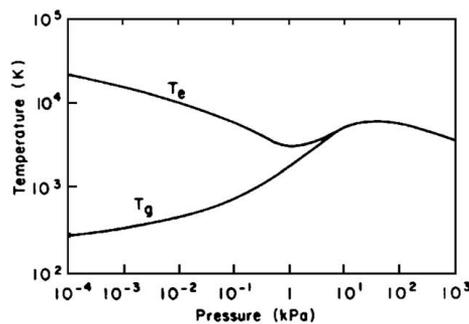
Figure 4. Plasma temperature and pressure [5]

A driving force for cold plasma developments is the avoidance of expensive equipment required for competing vacuum-based plasma technologies, like the mentioned NPIII. Although there are many applications where non-equilibrium (cold) plasma at atmospheric and higher pressures represents a substantial advantage, there are also a number of applications where low-pressure plasmas simply cannot be replaced.

Gas discharge plasma
When a sufficiently high potential difference is applied between two electrodes placed in a gas, the latter will break down into positive ions and electrons, giving rise to a gas discharge. The mechanism of the gas breakdown can be explained as follows: a few electrons are emitted from the electrodes due to the omnipresent cosmic radiation. Without applying a potential difference, the electrons emitted from the cathode are not able to sustain the discharge. However, when a potential difference is applied, the electrons are accelerated by the electric field in front of the cathode and collide with the gas atoms. The most

important collisions are the inelastic collisions, leading to excitation and ionization. The excitation collisions, followed by de-excitations with the emission of radiation, are responsible for the characteristic name of the 'glow' discharge. The ionization collisions create new electrons and ions. The ions are accelerated by the electric field toward the cathode, where they release new electrons by ion induced secondary electron emission. The electrons give rise to new ionization collisions, creating new ions and electrons. These processes of electron emission at the cathode and ionization in the plasma make the glow discharge a self-sustaining plasma.

As it can be seen in fig.5. when a potential difference is applied between two electrodes, the gas (e.g. argon) will break down into electrons and positive ions. The latter can cause secondary electron emission at the cathode. The emitted electrons give rise to collisions in the plasma, e.g. excitation (which is often followed by de-excitation with emission of radiation; hence explaining the name of the 'glow' discharge) and ionization (which creates new electrons and ions, and therefore makes the glow discharge a self-sustaining plasma). Besides, the argon ions, as well as fast argon atoms bombarding the cathode, can also give rise to sputtering, which is important for several applications (e.g. in analytical spectrochemistry, and for sputter-deposition of thin films). The method shown in fig3. is also called glow discharge.
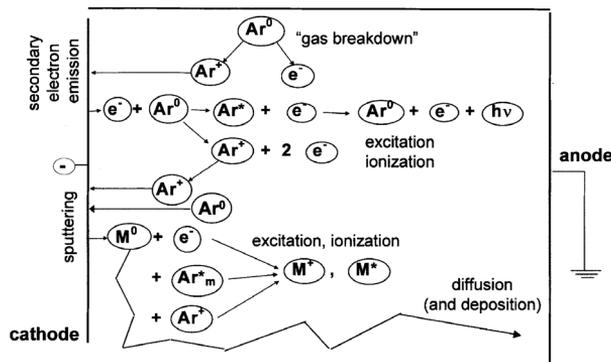
Figure 5. Schematic of the basic plasma processes [1]

Dielectric Barrier Discharge (DBD) source
The most popular cold atmospheric plasma sources are based on DBD [16, 17]. A dielectric barrier at one or both electrodes can suppress and, in combination with high frequency power, prevent streamers. There are a large number of different designs, constructions, electrode shapes, and dielectric barriers used in DBD sources for different applications. Some of these systems are schematically shown in fig. 6. A simple corona (not a DBD) arrangement with streamers is shown in fig. 6a for comparison with DBD arrangements in fig. 6b. DBD systems for treatments of moving planar substrates are displayed in fig. 6c and d. For large-area treatments, a multiple DBD arrangement can be used with a pair

of grid-shaped electrodes covered by an alumina barrier, fig. 6e [18]. In all DBD systems, the accumulated surface charges on dielectric barriers must be neutralized, e.g. by bipolar pulsed DC power in either static or flowing gas regimes. [15]

Figure 7, 8, 9 shows the cold plasma equipment used for the just started research. That DBD equipment is typically for flat surfaces.

The advantages:
– no vacuum is needed,
– small contact times,
– continuous in-line technology.

Typical cold atmospheric plasmas are suitable for rapid production of reactive radicals and for plasma-activated reactions based on radical chemistry.
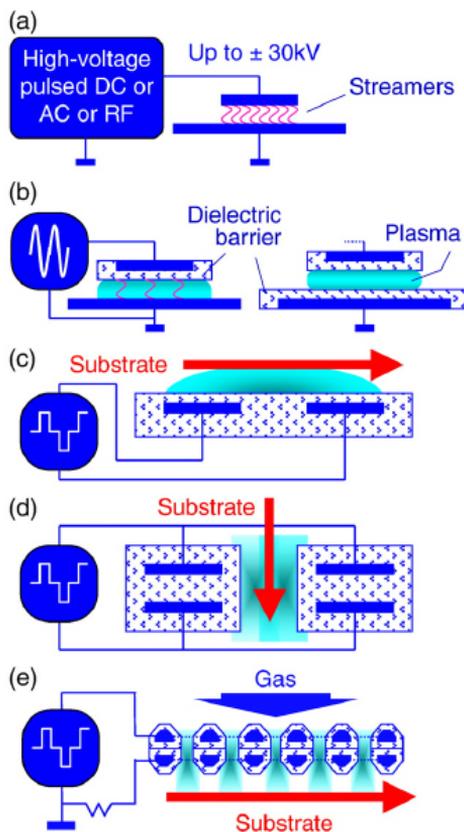
Figure 6. Corona and dielectric barrier discharge (DBD) arrangements.
(a) Corona with streamers; (b) dielectric barriers on electrodes;
(c) DBD arrangement for treatment of large-area planar substrates;
(d) DBD arrangement for two-sided treatments; and
(e) multiple grid-type DBD arrangement (200 μm×200 μm windows).
The arrows in (c), (d), and (e) indicate the direction
of substrate motion. [15]
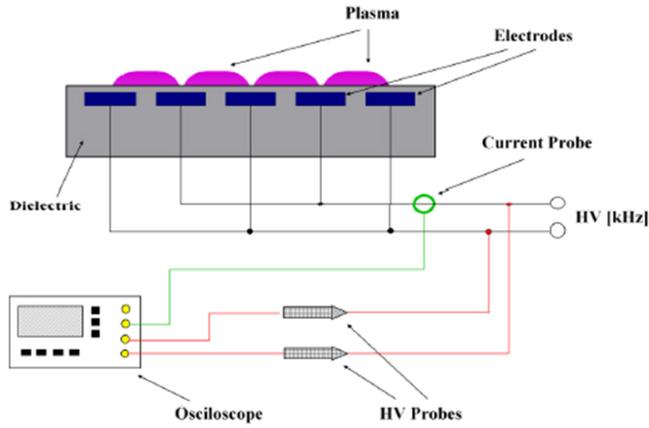
Figure 7. Scheme of DBD reactor [19]
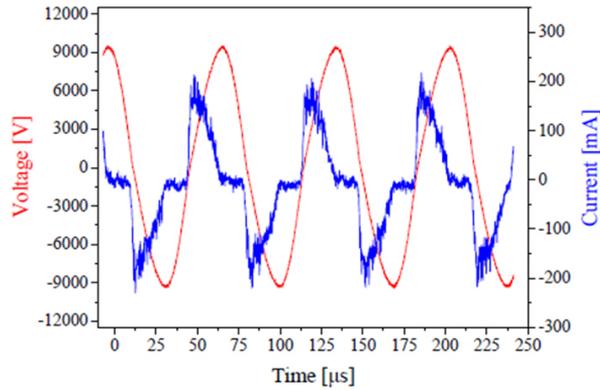
Figure 8. Curves of voltage and current of DBD reactor. [19]

Figure 9. DBD laboratory test equipment used
for polymer surfaces. [19]
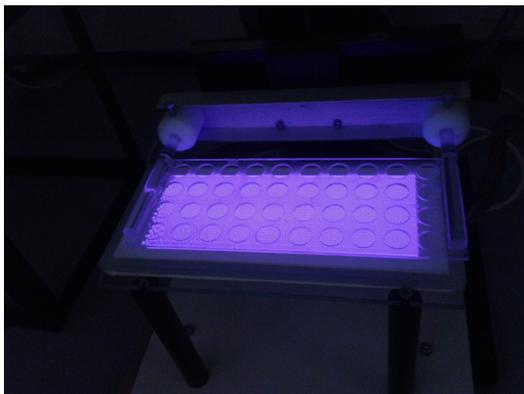
Figure 10. Acting atmospheric cold plasma with
specimen holder above it

Summary

As it is introduced more in depth in the literature [1], when a plasma is brought into contact with polymers, this can give rise to chemical and physical modifications at the surface, e.g. producing more reactive sites, or changes in cross-linking or molecular weight [20, 21, 22, 23, 24, 25,26]. In this way, materials with desired properties can be obtained, such as wettability, adhesion, barrier protection, material selectivity and even biocompatibility [27, 28].
Those results encouraged us to extend our NPIII research towards to cold plasma measurements focusing on the tribological properties and
adhesive bonding possibilities of engineering polymers.

Acknowledgement

References

[1] A. Bogaerts, E. Neyts, R. Gijbels, J.Mullen (2002): Gas discharge plasmas and their applications. Review Spectrochimica Acta. Elsevier. Pp 609 – 658
[2] M.A. Lieberman, A.J. Lichtenberg, (1994): Principles of Plasma Discharges and Materials Processing, Wiley, New York.
[3] B. Chapman (1980): Glow Discharge Processes, Wiley, NewYork.
[4] H. Conrads, M. Schmidt (2000): Plasma generation and plasma sources, Plasma Sources Sci. Technol. 9 pp 441–454.
[5] C. Tendero, C. Tixier, P. Tristant, J. Desmaison, P. Leprince (2006): Atmospheric pressure plasmas: A review. Spectrochemica Acta. Elsevire. Part B. pp 2 – 30.

[6] Bertóti I. (2003): A felületmódosítás korszerű módszerei, In: Műszaki felülettudomány és orvosbiológiai alkalmazásai. (Bertóti, I., Marosi Gy., Tóth, A., szerk.), B+V Lap és Könyvkiadó Kft,

[7] Kalácska G. (2012): Polimer gépelem anyagok tribológiai jellemzése. MTA doktori értekezés.

[8] Tóth A. (1994): Polimerek felületmódosítása és felületi kémiai szerkezetük jellemzése röntgenfotoelektron-spektroszkópiával. Kandidátusi értekezés, MTA SZKKL.

[9] Tóth A. (2003): Ortopédiai anyagok. In: „Műszaki felülettudomány és orvosbiológiai alkalmazásai. (Bertóti, I., Marosi G., Tóth, A., szerk.), B+V Lap- és Könyvkiadó Kft, pp 278-289.

[10] Tóth A., Mohai M., Ujvári T., Bertóti I. (2006): Hydrogen plasma immersion ion implantation of ultra-high molecular weight polyethylene. Surface and Interface Analysis, 38, pp 898-902.

[11] Tóth A., Mohai M., Ujvári T., Bertóti I. (2006): Advanced surface modification of ultra-high molecular weight poly(ethylene) by helium plasma immersion ion implantation. Polymers for Advanced Technologies, 17, pp 898-901.

[12] Tóth A., Kereszturi K., Mohai M., Bertóti I. (2007): Plasma based ion implantation of engineering polymers. Surface and Coatings Technology, 204, pp 2898-2908.

[13] Kalácska G., Zsidai L., Keresztes R., Tóth A., Mohai M., Szépvölgyi J. (2012): Effect of nitrogen plasma immersion ion implantation of polyamide-6 on its sliding properties against steel surface. Wear, 290-291, pp 66-73.

[14] Kalácska G., Zsidai L., Kereszturi K., Mohai M., Tóth A. (2009): Sliding tribological properties of untreated and PIII-treated PETP. Applied Surface Science, 255, pp 5847-5850.

[15] L. Bárdos, H. Baránková (2010): Cold atmospheric plasma: Sources, processes and applications. Thin Solid Films. Elsevier. Pp 6705 – 6713.

[16] U. Kogelschatz (2003): Plasma Chem. Plasma Proc. 23, 1.

[17] R.R. Roth, J. Rahel, X. Dai, D.M. Sherman (2005): J.Phys D:Appl.Phys. 38, 555.

[18] O. Sakai, Y. Kishimoto, K. Tachibana (2005): J.Phys.D:Appl.Phys. 38, 431.

[19] Z. Károly, Sz. Klébert (2015): Atmospheric cold plasma treatment for plastic surfaces. Workshop presentation. MTA TTK.

[20] J.R. Conrad, J.L. Radtke, R.A. Dodd, F.J. Worzala, N.C. (1987): Tran, Plasma source ion implantation technique for surface modification of materials, J. Appl. Phys. 62 4591–4596.

[21] H.K. Yasuda (Ed.), (1990): Plasma Polymerization and Plasma Interactions with Polymeric Materials, Wiley, New York,

[22] H.K. Yasuda, (1985): Plasma Polymerization, Academic Press, New York,

[23] W. Kern, J.L. Vossen (Eds.), (1978): Thin Film Processes, Academic Press, New York,

[24] M. Shen, A.T. Bell (Eds.), (1979): Plasma Polymerization, ACS Symposium Series, vol. 108,

[25] S. Veprek, M. Venugopalan (Eds.), (1980): Topics in Current Chemistry, Plasma Chemistry III, Springer-Verlag, Berlin,

[26] R. d'Agostino (Ed.), (1990): Deposition, Treatment and Etching of Polymers, Academic Press, New York, 1990.

[27] H. Biederman, Y. Osada, (1990): Plasma chemistry of polymers, in: H. Biederman (Ed.), Polymer Physics, Springer-Verlag, Berlin, pp. 57–109.

[28] O. Goossens, E. Dekempeneer, D. Vangeneugden, R. Van de Leest, C. Leys, (2001): Application of atmospheric pressure dielectric barrier discharges in deposition, cleaning and activation, Surf. Coat. Technol. 142–144, 474–481.

[29] H.K. Yasuda (Ed.), (1990): Plasma Polymerization and Plasma Interactions with Polymeric Materials, Wiley, New York,

Sliding friction and wear of polyoxymethlyene polymer

Yusuf ŞAHIN [1], Jan DE PAUW [2], Jacob SUKUMARAN [2],
Patrick DE BAETS [2]

[1] Department of Manufacturing Engineering, Gazi University, Ankara, Turkey
[2] Department Mechanical Construction and Production, Gent University, Belgium
[3] Department Mechanical Construction and Production, Gent University, Belgium
[4] Department Mechanical Construction and Production, Gent University, Belgium

Abstract

Polyoxymethlyen (POM) as a high performance engineering polymer is widely used in sliding components such as gears, cams, bearings and rollers in conveyors due to its self-lubrication properties and low moisture. Sliding wear tests were carried out under dry wear using on a conventional Plint type of tribometer with a polymer cylinder against a hardened smooth steel counter face. Friction coefficients and wear rates were determined at fixed speed under two different loads. The experimental results showed that static and dynamic coefficients of friction under 100 N nominal load varied between 0.43 and 0.27, respectively. In addition, the coefficient of friction and specific volumetric wear rate decreased with increasing the load.

Keywords

Polymer, POM, Dry sliding, Load, Wear, Friction

1. Introduction

Polyoxymethylene (POM) is a commonly used an engineering thermoplastic due to its high stiffness and strength, excellent chemical resistance, good fatigue and creep resistance. Among a range of thermoplastic polymers like PA, PTFE, PET, POM has also higher crystallisation ability due to their molecular structure and a very good dimensional stability, so better tribological performances was obtained (Zsidai et al., 2002). Thus, polymers can be chosen as a solution in certain applications of machine construction to be used as wear resistance materials such as bearing, guide, gear and other sliding parts. They are frequently used for replacement of bronze, brass, aluminium alloy and steels due to its cheaper and lighter (Kar and Bahadur, 1978). In most cases, however, it is of primary concern to develop polymeric materials that possess low friction and low wear properties under dry sliding conditions against smooth metallic counterparts (Franklin, 2001; Schwartz and Bahadur, 2001). The transferred of polymer materials may detreated or improve the service characteristics of a

system due to adhesion between the contacting surfaces by directly taking part in a sliding operation. The transfer always occurs from a polymer with a low cohesive energy density to one of higher cohesive energy density (Jain and Bahadir, 1978).

Small-scale tests are used because of their cost- and time-effectiveness with the ease of handling small samples and little sample preparation. They provide fundamental information about friction and wear mechanisms, consequently used for development of new materials or surface treatments (Ziemiankski and Capanidis, 1982; Kalácska, 2013). Lancaster (1990) investigated the friction in semi-crystalline polymers such as Nylon 66 and Polypropylene. The deformation mechanism involved dissipation of energy in the contact area and the adhesion component of friction of polymer results from the breakage of bonds between the polymer and mating surfaces. Friedrich et al.,(1995) studied the friction and wear properties of high temperature resistant polymers, particularly polyetheretherketone (PEEK) under various testing conditions against smooth steel counterpart. It is reported that the coefficient of friction value increased with increase in load. Tanaka (1982) investigated the wear properties of Polytetrafluoroethylene (PTFE), High density polyethylene (HDPE), Low density polyethylene (LDPE), and Nylon 6 at various sliding velocities and loads. It is concluded that PTFE exhibited higher constant wear rate throughout the wear process irrespective of the sliding velocities and loads. All polymers except PTFE exhibited lower wear rates when sliding on the transferred layer. Watanabe (1986) investigated the friction and wear properties of polyamide (N6) and reported that the sliding velocity and load influenced the frictional heating thereby increasing the wear rate due to increase in temperature. Wang and Li (1999) found that the sliding velocity influenced the sliding wear of UHMWPE polymer to a greater extent than the applied load (Unal et al., 2004). It is reported that the wear rates of POM and UHMWPE could decrease with increasing sliding speed when the roughness of the mating surface was low (Franklin, 2001). However, Bohm et al,.(1990) revealed that HDMWPE clearly outperformed all of other polymers tested while PEEK indicated the poor wear performance. Seabra and Baptisa (2002) found that UHMWPE-green was found to be the lowest frictional coefficient and good wear resistance among the food grade polymers like PTFE, UHMWPE, HMW-PE, PA 6, POM-C and PETP under sugar interface dry sliding conditions. The friction coefficients changed with counter face roughness, an optimal surface roughness of PETP/PTFE and POM-H which were lower than that of PA (Zsidai et al., 2012). The wear rates were higher on rougher surfaces for PA. Samyn and De Baets (2005) studied the friction of a commercial polyoxymethylene homopolymer (POM-H) to evaluate macroscopic parameters that allowed for extrapolation. No transfer was observed for small-scale tests, while a stable transfer film was developed under large-scale sliding with identical flash temperatures. Samyn et al.,(2006) reported that PET/PTFE sliding against the stainless steel developing the transfer layer on to the steel surface, which led to reduction in friction coefficient. There was no wear debris found for UHMWPE/carbon against stainless steel (Samyn and De Baets, 2005). SEM examination indicated that polymer transfer of POM-C was initiated by mechanical interlocking of metal asperities into the polymer.

The resulting wear debris particles were smeared into the roughness valleys and, finally the most of the metal surface was covered by the polymer (Mergler and Schaake, 2004). The wear behaviour of some polymers such as UHMWPE, PA-6/UHMWPE and PA-6 analysed by a statistical analysis (Liu et al.,2001; Sahin 2015a,b; Sagbas et al.,2009).

The above literature reviews have demonstrated that dry sliding wear resistances of polymers have been studied in terms of experimental base. There are limited numbers of studies on the sliding wear results of POMs based polymers using the effect of surface roughness of the counter face disc and higher loads (Marcus and Allen, 1994; and Zsidia et al., 2002; Ziemiankski, 1982; Samyan and De Baets, 2005; Mergler and Schaake, 2004; Franklin, 2001 and Sendra and Batisa, 2002). Therefore, aim of this work is to study the sliding wear behaviour of POM by experimentally at fixed speed under two different loads with dry conditions.

2. Experimental

Materials and Apparatus

The POM used in this present study, which is commercially available from Ertacetal Company. The characteristics of the POM-C (Ertacetal-C, white) thermoplastic wear samples. This POM indicates a linear decreasing strength between 80 and 110°C and keeps its favourable mechanical properties up to 92°C. The experimental apparatus is a pin-on-flat wear-testing machine with a reciprocating motion. A pin specimen is fixed to a reciprocating stage or to a pin specimen holder by setting screws. The diameter of the pin specimen is 8 mm with 15 mm in length. The pin is then mounted in a steel holder in the wear machine so that it is held firmly perpendicular to that of the flat surface of the rotating counter disc. The normal load is applied through a spring and lever system that pulls down a transverse bridge structure over the polymer specimen. The latter is mounted into a moving arm, which is connected to an eccentric system for conversion of the continuous rotating motion of an electromotor into a linear reciprocating motion. Friction force is measured with a strain-gauge detector installed on the wear-testing machine. The real wear or material loss of wear testing samples is calculated from weight loss of the polymer. It is compared to thickness reduction measured with a micrometer. The wear is on-line measured as the displacement of the transverse bridge structure on top of the polymer sample (LVDT).

POM is slid in a reciprocating motion against cold rolled steel AISI 42CrMo4 grinded to an average surface roughness, Ra = 0.20 µm perpendicular to the sliding direction. For the tests, a polymer cylinder is positioned into a moving head and is slid on its side (line contact) against a fixed steel counter face plate. The steel counter face is fixed to a base plate. The steel mating plate sizes of 58 x 38 x 4 mm, which is heat-treated to give a surface hardness of 59-62 RC. This is ground to a surface finish of approximately 0.15 µm centre-line average. The

sliding velocity is 0.3 m/s over a sliding stroke of 15 mm. The total sliding distance of 2160 and 4320 m ensures steady-state conditions. The wear pin is cleaned in acetone prior to and after the wear tests, and then weighed on a microbalance with 0.1 mg sensitiveness. The wear rate is calculated by measuring the mass loss, density and known sliding distance and load. The specific wear rate (K_s) is then expressed on volume loss basis.

3. Results and discussion

Friction Coefficient
The applied normal force and the concomitant tangential friction force of pin-on-flat for polymers against the smooth steel were measured in real time using a load cell. Typical and representative plots of the coefficient of friction including static and dynamic as a function of the sliding times for POM under 100 N contact load and a fixed speed are envisaged in Fig.1 and 2, respectively. The friction coefficient of the studied POM/steel tribo-pairs was measured to be in the range 0.42-0.44 and 0.21-0.31 for static and dynamic component, respectively. In addition, the static and dynamic friction coefficients appeared to vary similarly as a function sliding distance or time, but the dynamic friction coefficient exhibited lower values than the static component. Average coefficients of friction for POMs are also given in Table 2. After starting the test, the friction coefficient increased, where the running-in period was because the contact zone was reformed and restructured. During this period, a polymeric transfer film formed on the micro-topography of the steel surface. The maximum friction coefficient was obtained at 0.4×10^4 cycle and it took more than 60 min to reach the steady-state of friction coefficient. That's to say, the running-in time exceeded about 60 min, corresponding to $\approx 4 \times 10^4$ cycle.

The static and dynamic friction coefficient is plotted as a function of time in Fig.2 under 200 N load. At the initial start and reversals of the sliding direction, static friction was higher. The static friction decreased at higher normal load, which was the same trend for the dynamic friction because the time to establish a steady-state friction shortened. This might be due to a reduced contribution of ploughing component and frictional heat for the polymer, which increased the surface temperature, inducing the adhesive wear and plastic deformation. On the other hand, the transfer films formed by POM/steel combinations were discontinuous and formed the large debris particles, leading to large variations during the dry sliding wear. In addition, the friction coefficient increased rapidly throughout the first meters of sliding and subsequently decreased. After the initial stage, the less fluctuation occurred in the static friction due to a polishing process during wear because the wear tracks became a more smoother, thus, the friction coefficient fixed on a steady level, as shown in Fig.2. The friction evaluations indicated that it depended on the load. For example, the friction coefficient of the studied POM under 200 N applied load was measured to be in the range 0.28-0.29 and 0.23-0.24 for static and dynamic component, respectively.
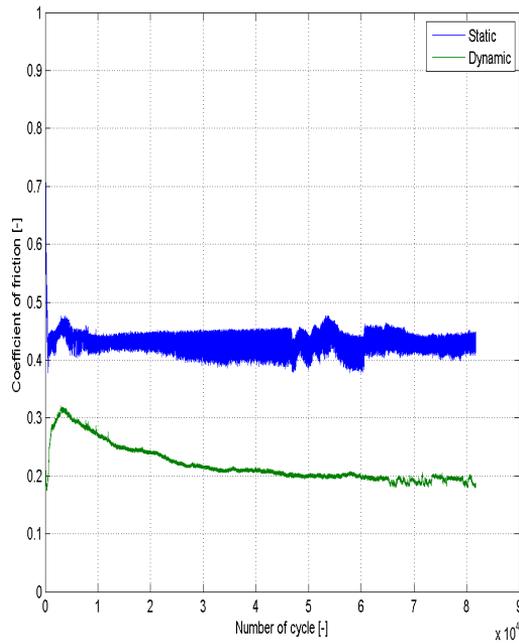
Figure 1. Static and dynamic coefficient of friction as a function of sliding time
for POM sliding at 0.3 m/s under a 100 N load against the smooth steel.
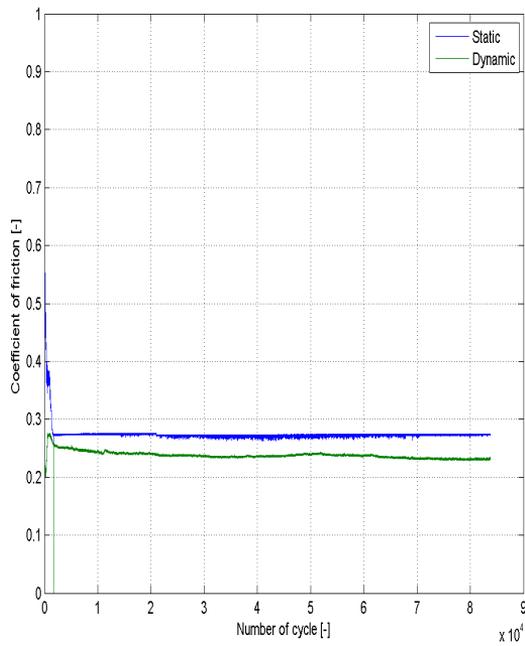

Figure 2. Static and dynamic coefficient of friction as a function of sliding time
for POM sliding at 0.3 m/s under a 200 N load against the smooth steel.

The literature indicated that transfer of POM to the metal counter face led to an increase in the COF (Mergler et al., 2004). The ultimate COF after 1000 m sliding of POM-C sliding against AISI 304 steel and 100Cr6 steel at 0.1 m/s was about 0.59 and 0.51, respectively. However, it decreased to 0.42 against 100Cr6 with decreasing the sliding speed to 0.05 m/s. The dynamic coefficient of friction of UHMWPE and POM at a reciprocating motion with polished steel slider was about 0.35 and 0.32 for UHMWPE and POM, respectively. It was found that the experimental materials were damaged rapidly when changed the sliding velocity from 0.42 to 0.84 m/s (Hu, 1998-30). Therefore, the sliding velocity had a more obvious influence on the wear behaviour of POM-H than the nominal load.

Wear

The experimental results of the adhesive wear of polymers at different conditions are shown in Table 2. The tests relevant to this table were carried out at a fixed speed, but indicated loads. Vertical displacement curves resulting from POM pins penetrating the steel counter samples were recorded using the inductive displacement transducers. Typical and representative wear data, obtained throughout reciprocate sliding experiments for POM/steel combinations, are plotted as a function of the sliding time in Fig.3. The normal displacement appeared to be vary a linearly after two hours testing time. This might be due to a continuous breaking and regeneration of micro-junctions. The wear mechanism of abrasion was dominated because abrasive furrows were discerned in the wear surface, parallel to the reciprocating sliding movement of the wear surface. After a running-in stage, the normal displacement and the wear volume ascended, and changed the trends and reached at a steady-state (Fig.3).
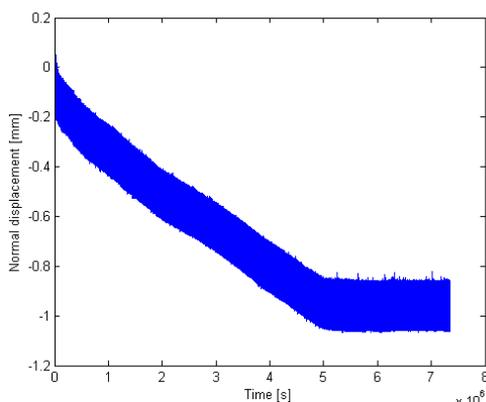

Figure 3. Normal displacement as a function of sliding time for POM sliding
at 0.3 m/s under a 100 N load against the smooth steel.

Fig. 4 shows the normal displacement as a function of sliding time for POM sliding at 0.3 m/s under a 200 N load against the steel. It is observed that the normal displacement or depth of deformation on the samples decreased as a

function of time and, the slightly lower wear volume was obtained for the samples tested at higher load because adhesion component became a more effective due to thermal effects. A higher strain could be associated with actual contact area. The temperature at the frictional surfaces increased with increasing the load and the frictional heat on POM cannot be distributed in time due to the poor ability of heat transfer. In the running-in phase, the asperity summits became blunt and the spaces between asperities were filled. This resulted in lower wear in the steady-state phase. The duration of the running-in phase was dependent on the test condition. The volumetric wear rate was calculated both from weight loss and thickness reduction. The volumetric wear rate obtained from thickness was lower than the weight loss. It is evident from the figure that the volumetric wear rate slightly decreased with increasing applied load, which could be explained with the fact that the wear rate is determined by the pv–value, where p stands for the load and v for the velocity. The velocity is lower for this case, but the specific wear decreased with increasing the load. The wear rates of the tested samples at loads of 100 N and 200 N varied from 1.323×10^{-6} and 0.6102×10^{-6} mm^3 / N.m. Samyn et al.(2007) showed that wear rates was ranged from 6×10^{-7} to 4×10^{-4} mm^3 / N.m. Typical wear coefficients obtained from pin-on-disc tests with POM pins against rotating steel disc were found to be around 2×10^{-6} to 4×10^{-6} mm^3 / N.m in the available literature (Franklin, 2001; Unal et al., 2004; and Mens et al., 1991).
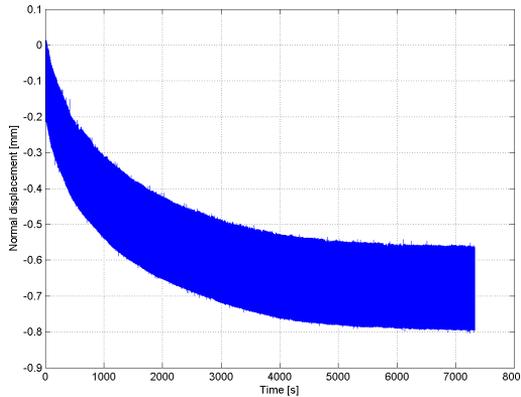
Figure 4. Normal displacement as a function of sliding time for POM sliding
at 0.3 m/s under a 200 N load against the smooth steel.

Table 2. The experimental results of the dry wear of POMs under two different conditions

Load	Weight loss,gr	Density, gr/cm^3	Volume loss, mm^3	Specific wear rate (mm^3/N.m) (10^{-6})	Volume loss, mm^3	Wear rate by LVDT	Static COF	Dynamic COF
100	0.04030	1.41	0.028582	1.323241	22.049	1.020	0.42-0.44	0.21-0.31
200	0.03717	1.41	0.026362	0.610231	16.549	0.383	0.27-0.28	0.23-0.25

When the pin starts moving again, the static coefficient of friction applies. The measured friction forces drops in the endpoints since the plate rests on leaf springs. The static coefficient friction is plotted as a function of time in Fig.5 and Fig.6 for 8 cycles under 100 N and 200 N loads, respectively. There are left endpoints and right endpoints in these graphs. When the polymer pin started moving again, the friction force increased rapidly. The difference in roughness of the parts of the samples underpins the difference in strength between the go and return. The static friction decreased at higher normal loads, which was the same trend for the dynamic friction. Samyn De Baets (2005) indicated that the tendency of stick-slip for POM-H reduced at higher loads for large-scale tests under high loads and low sliding velocity than for small scale tests, which might be due to the more favourable edge to contact area ratio. Later work by the same authors (2007) indicated the dynamic friction coefficients of POM-H at different conditions were about 0.78 and 0.60 at a fixed speed 0.3 m/s for 100 N and 200 N, respectively. However, they measured the dynamic friction of about 0.33 under 200 N load with 1.2 m/s speed. Yamaguchi (1990) obtained the static friction of POM/steel in the range of 0.1-0.5 N and found a constant value independent of nominal load. The coefficient of static friction was not affected as much as the coefficient of dynamic friction, which is not the case for the present results. Kalacska (2013) measured that the dynamic coefficient of frictions for POM-C, PEEK and PA6G using pin-on-disc configuration (pv = 2 MPa.m/s) were about 0.20, 0.29 and 0.33, respectively.
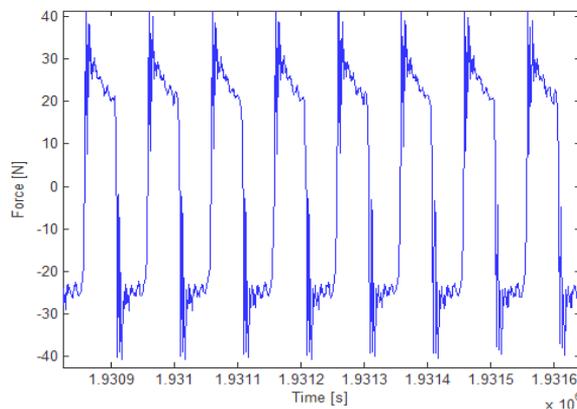
Figure 5. Variations of static and dynamic friction force at 100 N load during reversal of the sliding motion during dry wear testing.

The transfer of material from polymer to metal surface initiates because of adhesion between the two materials, which during sliding contributes to shear in the subsurface region of the contact. Different mechanisms for adhesion can be Coulomb electrostatic forces, van der Waals forces, and bonding from chemical reactions. Tanaka et al.,(1982) suggested that transfer film was formed because

of the destruction of the banded structure of PTFE due to its low activation energy (7 kcal/mol) of slippage between the crystalline slices. Kar and Bahadir (1978) point out that the slippage of crystalline slices interspersed with amorphous material contributed to the interlamellar shear.
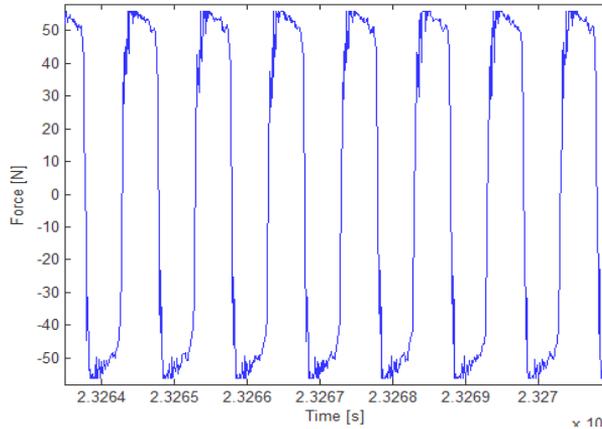
*Figure 6.* Variations of static and dynamic friction force at 200 N load during reversal of the sliding motion during dry wear testing.

Conclusions

The following conclusions were drawn in terms of the experimental results for wear of POM polymer-steel combinations.

1. The experimental results showed that the weight loss/volume loss of the samples was not influenced highly by load, but the specific wear rate decreased considerably with increasing the load. The wear rates of the tested samples under the specified loads varied from 1.3232×10^{-6} and 0.6102×10^{-6} mm^3/N.m.

2. The friction coefficient of POM/steel tribo-pairs when tested at 100N load was measured to be in the range 0.42-0.44 and 0.21-0.31 for static and dynamic component, respectively. The coefficient of friction also decreased with increasing the load.

References

[1] Bahadir S.,(2000), `The development of transfer layers and their role in polymer tribology`, Wear 245, pp. 92-99.

[2] Bohm H., Betz S., Ball A., (1990), `The wear resistance of polymers`, Tribol. Inter.23 (6), 399-406.

[3] Cai H.C., Yan F.Y., (2003), `Investigation of tribological properties of Al2O3-polyamide nanocomposites', Polym.Test., 22, pp. 875-882.

[4] Dowson D., Challen J.M., Holmes K., Atkinson J.R., (1978), `The wear of non-metallic materials`, proc.3rd Leeds-Layon Symp.on Tribology, Institute of Mechanical Engineers, MEP, London, pp. 99-112

[5] Friedrich K., Lu Z., Mager A.M.,(1995), Recent advances in polymer composites Tribology, Wear 190, pp.139–144.

[6] Franklin S.E.,(2001), `Wear experiments with selected engineering polymers and polymer composites under dry reciprocating sliding conditions`, Wear 251, pp.1591–1598.

[7] Hu X., (1998), `Tribological behaviour of modified polyacetal against MC nylon without lubrication`, Tribology Letters 5, pp. 313-317.

[8] Jain V.K., Bahadir S.,(1978), `Material transfer in polymer-polymer sliding`, Wear 46, pp. 177-188.

[9] Kalácska G., (2013), `An engineering approach to dry friction behaviour of numerous engineering plastics with respect to the mechanical properties`, eXPRESS Polymer Letters, 7 (2), pp. 199–210.

[10] Kar M.K., Bahadur S.,(1978), `Micro mechanism of wear at polymer–metal sliding interface`, Wear 46, pp. 189.-192.

[11] Kurukawa M., Uchiyama Y., Iwai T., Nagai S., (2003), `Tribological properties of Polyoxymethylene composites against aluminium`, Journal of Tribology 25, pp. 661-669.

[12] Lancaster J.K., (1990), `Material-specific wear mechanisms relevance to wear modelling`, Wear 141, pp.159– 183.

[13] Liu C.Z., Ren L.Q., Tong, J., Joyce T.J., Green S.M., Arnell R.D.,(2001), `Statistical wear analysis of PA- 6/UHMWPE alloy, UHMWPE and PA-6, Wear 249, pp.31–36.

[14] Luıs C. Seabra., Antonio M. Baptista.,(2002), `Tribological behaviour of food grade polymers against stainless steel in dry sliding and with sugar`, Wear 253, pp.394–402.

[15] Marcus K., Allen C., (1998), `The sliding wear of ultrahigh molecular weight polyethylene in an aqueous environment`, Wear 178, pp. 17-28.

[16] Mens J.W.M., de Gee A.W.J., (1991), `Friction and wear behaviour of 18 polymers in contact with steel in environments of air and water`, Wear 149, pp.255-268.

[17] Mergler Y.J., Schaake R.P., Huis in't Veld A.J., (2004), Material transfer of POM in sliding contact, Wear 256, pp.294–301.

[18] Şahin Y. (2015), 'Wear analysis of polyamide based on a statistical approach`, Int. J. of Materials and Product Technology (IJMPT), 2015 (in press).

[19] Şahin Y. (2015). 'Analysis of abrasive wear behaviour of PTFE composite using Taguchi's technique', Cogent Engineering 2, pp. 1-15.

[20] Sagbas A., Kahraman F., Esme U., (2009), `Modelling and predicting abrasive wear behaviour of POM using responds surface methodology and neural networks`, Metabk 48 (2), pp. 117-120.

[21] Samyn P. and De Baets P., (2005), `Friction of polyoxymethylene homopolymer in highly loaded applications extrapolated from small-scale testing`, Tribology Letters 19 (3), pp. 177-189.

[22] Samyn P. and De Baets P.,(2005), `Wear transition and stability of polyoxymethylene homopolymer in highly loaded applications compared to small-scale testing`, Tribol. Inter. 40, pp. 819-833.

[23] Samyn P., De Baets P., Schoukens G., Van Peteghem A.P., (2006), `Large-scale tests on friction and wear of engineering polymers for material selection in highly loaded sliding systems`, Mater. Des. 27, pp.35–555.

[24] Samyn P., De Baets P., (2005), `Friction and wear of acetal: A matter of scale`, Wear 259, pp.697-702.

[25] Schwartz C.S., Bahadur S.,(2000), `Studies on the tribological behaviour and transfer film counter face bond strength for polyphenlyene sulphide filled with nanoscale alumina particles`, Wear 237, pp. 261-273.

[26] Sun L.H., Yang Z.G., Li X.H., (2008), `Study of the friction and wear behaviour of POM/Al2O3 nano composites`, Wear 264, pp. 693-700.

[27] Tanaka K., (1982), `Transfer of semi crystalline polymers sliding against smooth steel surface`, Wear 27, pp.183–199.

[28] Unal H., Sen U., Mimaroglu A., (2004), `Dry sliding wear characteristics of some industrial polymers against steel counter face`, Tribology International 37, pp.727–732.

[29] Yamaguchi Y.,(1990), `Tribology of plastic materials`, Elsevier Tribology Series 16, ISBN 0-444-87445-3.

[30] Ziemiankski K., Capanidis D.,(1982), `The mechanism of dry friction of polyoxymethylene against steel`, Wear 82, pp. 317.

[31] Zsidai L., De Baets P., Samyn P., Kalacska G., Van Peteghem A.P., Van Parys F., (2002), `The tribological behaviour of engineering plastics during sliding friction investigated with small-scale specimens`, Wear 253, pp. 673–688.

[32] Wang Y.Q., Li J., (1999), `Sliding wear behaviour and mechanism of ultra-high molecular weight polyethylene`, Mater Science Engineering, A 266, pp. 155–160.

[33] Watanabe M., (1986), `The friction and wear properties of nylon`, Wear 110, pp.379–188.

Diffusion bonding of plasma facing components of fusion reactor (ITER)

Tétény BAROSS[1], László JÁNOSI[2], Gábor KALÁCSKA[2], Gábor VERES[1]

[1]WIGNER RCP, RMKI, PO Box 91, H-1521 Budapest,
[2]Institute for Mechanical Engineering Technology

Abstract

The actuality of the topic comes from the ITER (International Thermonuclear Experimental Reactor) fusion tokamak which is under construction. It aims to demonstrate the scientific and technical feasibility of fusion as an energy source. A fusion reactor faces the engineers with several manufacturing problems. One of that is the fabrication of first wall elements. It needs to withstand serious heat and neutronic load during the ITER lifetime. The main issues come from the welding of dissimilar materials with different physical properties. This paper is going to summarize the latest results of related manufacturing technology called hot isostatic pressure (HIP) welding.

Keywords

Hot isostatic pressure (HIP) welding, diffusion, ITER first wall

1. Introduction

The ITER (International Thermonuclear Experimental Reactor) fusion reactor called tokamak is aiming to demonstrate the scientific and technical feasibility of fusion as an energy source. It can help to develop a new type of power plant in the world. According to the present plans ITER is the latest step before the first fusion power plant, called DEMO, as „demonstration" power plant.

In the history bigger and bigger fusion reactors were built to increase the gained energy from the fusion reactions of deuterium and tritium. Until recent days the fusion power did not reach the heating power.

Energy gain: Q = Fusion Power/Heating Power.

One of the dedicated goals of ITER is to reach the Q=10 energy gain. It involves much larger nuclear and heat load on the surface elements and involves several engineering problems compared to the present tokamaks. One of that is when flat surfaces have to be welded together for vacuum boundary or for heat transfer. An example can be the welding of cooling manifolds with milled cooling grooves on the surfaces of thick stainless steel materials. Another challenge is welding dissimilar materials with different physical properties like

different thermal expansions, melting points etc. The diffusion bonding is a type of solid-state welding, when at an elevated temperature without melting the original materials and under pressure the dissimilar particles diffuse together. The HIP (hot isostatic pressure welding) is the candidate welding procedure at the critical ITER first wall.

The literature of HIP welding has more important aspects. One is the anisotropy of the material after the manufacturing procedure. (for example the manufacturing of pipes and plates results anisotropy) (Zhao S.X., 2014), (Huang B., 2011). Second problem is the usage of proper films / interlayers that shall be put between the welded materials compensating the different material properties and it may influence the formation of the intermetallic layers (Park J.Y. et.al. 2013). Third significant topic is the thermal cyclic fatigue tests, which is needed to validate a welded connection. In a fusion reactor the thermal periods will be repeated more thousand times. For the continuous monitoring of the welding connection Jun Li, (2011) gives a good experimental solution.

2. Diffusion HIP welding procedure

In this section the parameters of diffusion bonding and the procedure of welding will be summarized. The HIP welding for ITER first wall elements was decided to carry out under vacuum conditions, against the shielding gas. The welding under vacuum demands more complex equipment, but it results more clean welded surface without inclusions. The welding temperature has to be chosen to reach the recrystallization temperature of material. It is chosen for the material with lower melting point: 70-80 % of the melting temperature. In order to close the surfaces against surface roughness a continuous static pressure is needed. It highly depends on the welded material hardness or the used intermetallic layer material properties. So the range can be 5 MPa until 200 MPa. For adequate diffusion the holding time is around 60-120 min. These parameters are summarized in Table 1.

Table 1. Range of diffusion welding parameters

Medium of welding is vacuum	$10^{-2} – 10^{-4}$ [Pa]
Temperature during welding process	$700 – 1050$ [°C]
Static pressure	5, 100, 150, 200 [MPa]
Duration of welding	60-120 [min]

For example a diffusion bonding between W and EUROFER97 using V interlayer setup can be seen on Figure 1. Interlayers shall compensate during the joining of the large mismatch of their CTE (coefficient of thermal expansion, 4.5 x 10-6 [K] for W and 12.7 x 10 -6 [K] for EUROFER97 at room temperature

(RT)) that can cause otherwise a high thermally induced residual stresses along the bond interface, particularly when the bonded specimens are cooled down rapidly from an elevated process temperature to RT. (W.W. Basuki, 2012)

On Figure 1. the W and EUROFER97 (stainless steel) specimen with a diameter of 18 mm and a length of 22 mm were machined. The vanadium interlayer was cut from a 1 mm thick commercial plate. Between two Al2O3 ceramic plates were placed this specimen. The process was performed at 1050 [C°] applying uniaxial compression stress that was determined for a bonding duration 1 h, when the secondary creep strain on the EUROFER97 side was limited to 5%. After that the specimen was cooled down to 200 [C°]. Afterwards a heat treatment was conducted similar to HIP process on 760 [C°] for 90 min, before the bonded sample was cooled down to room temperature. (W.W. Basuki, 2012)
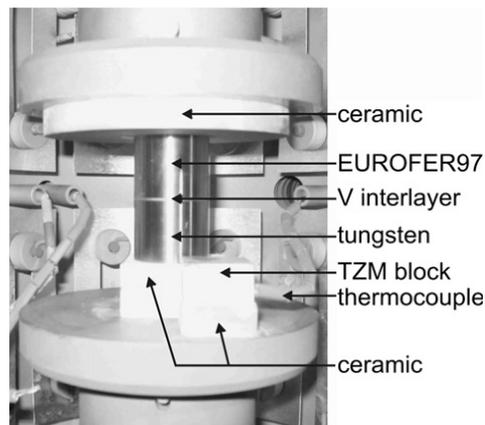

Figure 1. Experimental setup for the uniaxial diffusion
bonding (W.W. Basuki, 2012)

This bonding process is a good overview from the fusion literature, that gives similar bonding processes and subsequent mechanical and microscopic examinations.

3. Anisotropy of hot radial pressure welded components

On Figure 2 the schematic of hot radial pressing (HRP) technology can be seen. The major different between HRP technology and HIP welding is the static pressure for welding that is ensured by high gas pressure at HRP. Figure 3. shows a test mock-up for ITER first wall. Similar wolfram monoblocks units welded on CuCrZr cooling tubes will cover the ITER inner wall.
Zhao S.X. (2014) attracts attention to the anisotropy of materials from manufacturing procedure may cause bonding flaws at CuCrZr/Cu interfaces using the HRP technology.
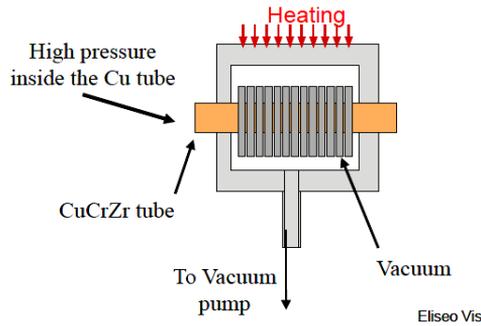
Figure 2. Schematic of Hot Radial Pressure welding (Visca E., 2010)
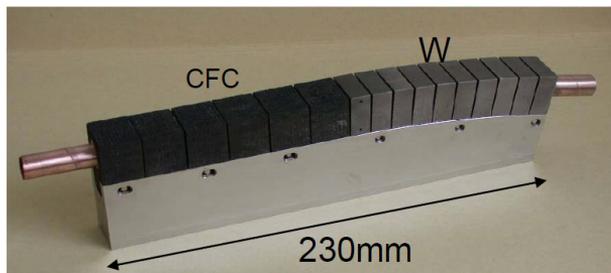
Figure 3. Test mock-up for ITER first wall (Visca E., 2010)

At CuCrZr tubes cracking and denting, were observed during the manufacturing of ITER-like mono-block W/Cu components employing hot isostatic pressing(HIP). Microscopic investigations indicate that the occurrence of axial strain localization correlates to the heavily deformed Cu grains and elongated Cr-rich precipitates.

Figure 4 optical microscope photos is depicting CuCrZr/Cu interfacial defects (highlighted by black cycles) caused by moderate (a) and severe (b) denting. Summarizing, Zhao S.X. (2014) demonstrated in his article that testing only the axial mechanical properties is not enough for manufacturers who use hot radial pressing technology.
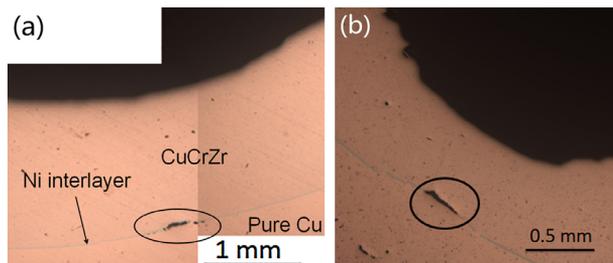
Figure 4. Interfacial defects caused by moderate (a) and severe
(b) denting (Zhao S.X. 2014)

4. Using interlayers between HIPed surfaces

During direct welding of different materials various problems occurs that in many cases deny the direct welding. The design of plasma facing components involves various combinations of joints like Be / Cu, W / Cu, SS316 / Cu alloy, W / FMS (ferritic martensitic steel), SS / SS. In these cases an interlayer material is required. Before interpretation of interlayer it is worthy to summarize after G. Kalinin (2001) the characteristics of these joints:

Characteristics of Be/Cu joints
„The main problem of bonding Be to Cu alloys is that Be reacts with almost all metals at moderate and high temperatures and forms brittle intermetallic phases that are detrimental for the joint reliability and the fatigue lifetime." (G. Kalinin 2001)
    These solutions were examined this issue:
– Use of filler materials between Be and Cu alloy which do not form intermetallic layers.
– Use of interlayers as diffusion barrier with less affinity for formation of beryllide.
– Direct binding at a lower temperature.

Characteristics of W/Cu joints
The main problem is the large difference of the coefficient in thermal expansion (CTE) and of elastic modulus.
    These solutions were examined this issue:
– An engineering solution can be the welding of blocks with thinner jointed surfaces.
– On the surface of Cu a W coating preparation with CVD (Chemical Vapour Deposition)

Characteristics of SS/Cu joints
Plasma facing components in ITER will include several joints: copper plates with steel cooling tubes and plates for the first wall, copper structures with steel plate and/or copper. During examinations a good bonding of both CuCrZr and CuAl25 alloys to SS was achieved.
    In the following articles the using of interlayers with coatings were examined. (Park J.-Y., 2013), (Jung Y.-I., 2013).
    Tungsten (W) was joined successfully to ferritic/martensitic steels (FMSs) by HIP with interlayers consisting of Ti(2 μm) or Cr (2 μm) coatings and inserted Ti(50 μm) and Cu(10 μm) films. (Park J.-Y., 2013) The joining strength of the W/FMS joint was measured by a standard shear test. The interface microstructure was observed by scanning electron microscopy (SEM) and the the element distribution in the interface was analysed.
    The examination gave the Ti films with higher shear strength than those with Cu films. The effect of coating material was not large on the joining strength. No

cracking was observed in the interface after HIP joining each interlayer type. On Figure 5 a specimen with W / Cr coated / Ti interlayer / FMS combination can be seen by HIP at 1173 K and 100 MPa for 1.5 h.
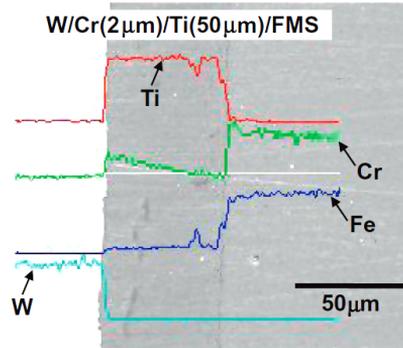
Figure 5. Interface microstructures and element distributions
of W/FMS joined with Ti(2 μm)/Ti(50 μm) interlayers by HIP
(Park J.-Y., 2013)

On Figure 6 the SEM image of the interface microstructure is visible, that Cu forms many intermetallic diffusion layer. It is worth to note that the complicated interface led to a decrease in the joining strength.
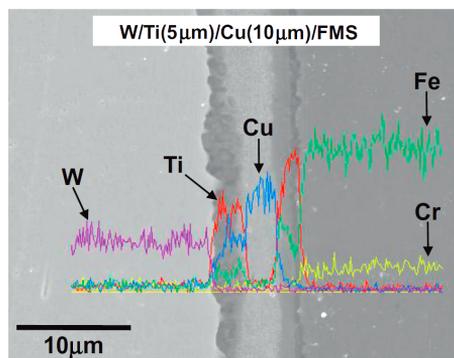
Figure 6. Interface microstructure and element distributions
of W/FMS joined with Ti(5 μm)/Cu(10 μm) interlayer by HIP
at 1173 K and 100 MPa for 1.5 h. (Park J.-Y., 2013))

Jung Y.-I., (2013) perform similar HIP welding. He reports the details of the changings of microstructure near to the interlayers. Conclude the diffusion welding with interlayers: using of interlayers involve the complex microstructure observations beyond the standard mechanical test like shear or bend, or tensile tests. Another interesting problem is the changing of microstructures during the ITER lifetime.

5. Thermal fatigue test of diffusion bonded specimens

During the ITER lifetime the plasma facing components have to survive heavy thermal cyclic load. Following this the fatigue properties of welded materials became serious. Similar to the ITER tokamak's loads in the EAST tokamak a significant heat load up to 7-10 MW/m2 in steady state can reach the wall. For this two actively cooled mock-ups with 5 mm thick tungsten armour, joined to CuCrZr alloy were successfully developed by diffusion bonding technique with Ti or Ni interlayer. Its thermal fatigue properties were investigated with active cooling. In East tokamak maximum (Jun Li, 2011) Figure 7 shows the mock-up of heat load experiment.
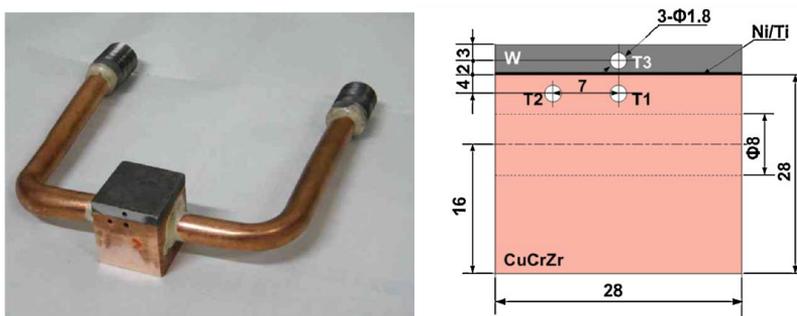
Figure 7. Mock-up for heat load experiment (Jun Li, 2011)

The simulation results indicated and measurements shew Ti has better thermal contact capability then Ni. See Figure 8 the comparison of simulated and tested results. Mock-up with Ti had good agreement with simulation compared to Ni. It demonstrates the initial bonding defect of Ni, however the SEM image of microstructure did not indicate cracks or failures. Only a discontinuous reacted layer was determined by EDS as Ni4W and TiCu at the other mock-up.
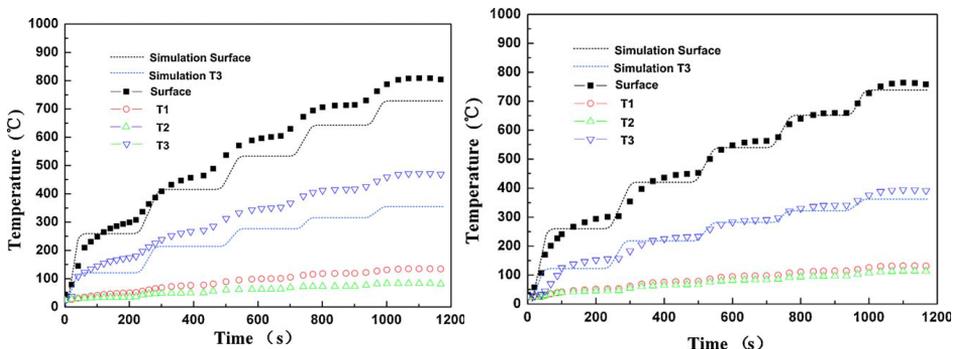
Figure 8. Simulation and tested results of to heat flux from 0 MW/m^2 to 10MW/m^2 using of Ni and Ti interlayers (Jun Li, 2011)

Fatigue test were conducted with heat flux 10 MW/m2 Surface temperatures did not change until 98 Ni / 129 Ti thermal cycles. Possible reason is the reduction of heat transfer capability at interlayers are the cracks, failures. (Jun Li, 2011)

Microstructure analyses indicated that cracks or failures were produced due to cyclic thermal stresses by thermal fatigue test. Cracks and failures arose near to the interlayers in tungsten due to the brittleness of tungsten. It was similar in Ni and Ti case.

Conclusion

This article aims to give an overview about the ITER plasma facing components in view of the diffusion welding technology. The procedure of the HIP welding was introduced with the main parameters. Than an example for welded failures occurred by anisotropic material was introduced. After that welding with interlayers were presented. Finally the results of a fatigue thermal test on two mock-up were presented.

For the complexity of HIP bonding is characteristic the several type of examination methods. Namely the tensile test, shear test, Charpy impact test, microscopic observations (OM, SEM, TEM, EDS, XRD), micro-Vickers hardness tests, FEM analysis, investigation of thermal transfer capability.

The investigation of HIP welding has several aspects as welding technological, mechanical properties, microstructural changes or material science. This requires a synthetic work.

Nomenclature

EUROFER 97 - RAFM (Reduced-activation ferritic martensitic), structural steel for the next generation of fusion reactors, melting point: 1536°C, CTE: 12.7 x 10 ^(-6) K^(-1)

Acknowledgement

References

[1] Jun Li, Jian-Feng Yang, Jun-Ling Chen (2011), High heat load properties of actively cooled W/CuCrZr mock-ups by diffusion bonding with Ni or Ti

interlayer, Fusion Engineering and Design, Volume 86, Issue 12, Pages 2874-2878, ISSN 0920-3796,

[2] G. Kalinin, V. Barabash, S. Fabritsiev, H. Kawamura, I. Mazul, M. Ulrickson, C.Wu, S. Zinkle (2001) ITER R&D: Vacuum Vessel and In-Vessel Components: Materials Development and Test

[3] Eliseo Visca (2010), MANUFACTURING PROCESSES FOR HIGH HEAT FLUX COMPONENTS, 4th Karlsruhe International Summer School, Karlsruhe Institute of Technology

[4] Widodo Widjaja Basuki, Jarir Aktaa (2012), Diffusion bonding between W and EUROFER97 using V interlayer, Journal of Nuclear Materials, Volume 429, Issues 1–3, Pages 335-340, ISSN 0022-3115,
 http://dx.doi.org/10.1016/j.jnucmat.2012.05.049.

[5] S.X. Zhao, L.J. Peng, Q. Li, W.J. Wang, R. Wei, S.G. Qin, Y.L. Shi, S.P. Chang, Y. Xu, G.H. Liu, T.J. Wang, G.-N. Luo (2014), Axial strain localization of CuCrZr tubes during manufacturing of ITER-like mono-block W/Cu components using HIP, Fusion Engineering and Design, ISSN 0920-3796,

Towards the understanding of variable amplitude fatigue

Nahuel MICONE, Wim DE WAELE, Saosometh CHHITH

Department of mechanical, Construction and Production, Belgium

Abstract

Fatigue life estimation is of high importance during the design stage of a machine or component. Basic fatigue calculations are made based on the use of an S-N curve. As far as constant amplitude loads are applied, this approach works well. However, most part of components in service are subjected to a variable amplitude load spectrum. In this case, linear approaches for fatigue life estimation can lead to over conservative results, which in other words means a heavier and more expensive machine. To further investigate the effect of (complex) service spectra (measured or statistically calculated), simpler load variations must be studied. This paper aims to show the general trend of these events and suggest the underlying physical phenomena behind load and interaction effects. As it will be highlighted, overloads are frequent in a spectrum and they are believed to be responsible for retardation effects. The plasticity induced crack closure mechanism is the most profound explanation for them to occur.

Keywords

Variable Amplitude; Overload; Underload; Fatigue; Steel

1. Introduction

In almost every situation that involves fatigue, the nature of the loads to which a component is subjected, is time varying. The study of different "in service" time histograms has allowed engineers to statically describe them through loading spectrums. With the need for optimum light-weight design, originally the aircraft industry was the main driver for these efforts [1]. For the agricultural industry the transmission and drive axle seems to be of major concern, since most part of the actual literature focuses on these components. For this particular application, plowing speed and soil condition are some of the parameters of importance. These factors are combined and a linear damage rule (Miner's rule) is normally used to calculate fatigue life. However, this approach has been reported to be (in certain situations) over or under conservative [2], which means that the variable amplitude loads could lead to a non-linear fatigue behaviour of the structure. The main reasons for this to occur are the load and interaction effects and are explained in the following.

Fatigue life is divided in three stages named, nucleation, initiation and crack propagation. These phases are loading dependent and therefore a change in the load level also means a change in the damage factor (D) which characterize the reduction (or extension) of the fatigue life. This is known as the load effect or load dependency. Fatigue damage variations are also dependent on the fatigue damage condition of the material as caused by previous cycles. In other words how the crack has grown from its initiation until its actual dimension. These effects are called interaction effects.
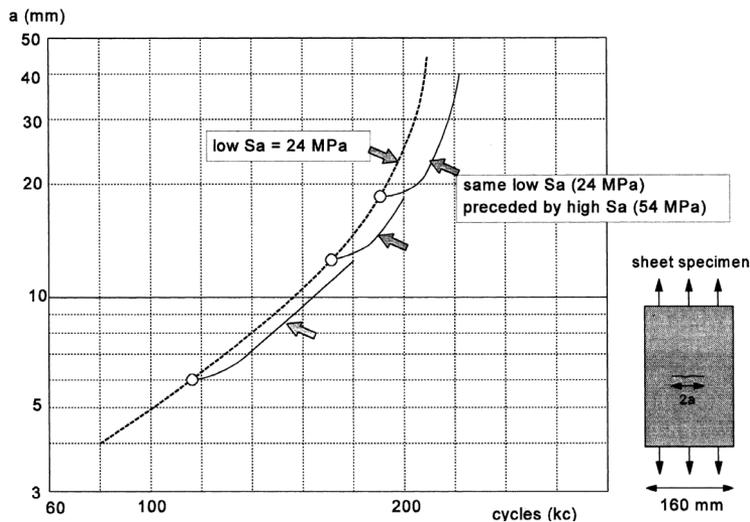
Figure 1. Crack growth retardation after transitions
from a higher to a lower amplitude level [4]

An example of load dependency can be seen in Fig. 2, where the comparison of the crack growth in a constant amplitude test and the introduction at three different moments of a secondary load block with a higher load range is displayed. After a number of cycles the first stress amplitude was restituted. Following the transition of a higher to a lower amplitude, the crack growth was retarded. After a certain amount of cycles, both curves were parallel to the original one and the crack growth rate was not delayed again.

2. Description and sequence type

The simulation of spectrums derived from real structures appeared as a requirement to obtain realistic results. However their complexity encouraged researchers to create test programs that are as representative of the reality as possible but with high repeatability and a relatively simple mathematical description. Soon the results of these simplified programs showed a high variety

of results depending on the load sequence. To better understand these differences, simplified sequences of loads have been defined (see table 1). These sequences can be splited up in three main categories: random/load-service, simple VA load and block load [3]. Table 1 graphically shows the difference between these. Furthermore they are briefly described below.

Table 1. Overview of VA loading histories

Loading type	Sequence type	Representation	Effect	Reported Materials	References
Random loading	Spectrum		Undefined	Ti and Al alloys	[4-6]
Simple loading	Single OL		Retardation	Ti and Al alloy, SS, structural and vessels steels	[9-14, 18, 20]
	Sequence of OL's		Retardation (higher than OL)	Al alloy, structural and vessels steels	[9, 12, 16, 22]
	Periodic sequence of OL's		Retardation or acceleration	AL alloy, structural and vessels steels	[22, 23, 36]
	Single UL		Acceleration	AL alloy, structural and vessels steels	[20, 24]
	Sequence of UL's		Retardation	Low carbon steel, Ti and Al alloys	[24]
	Periodic sequence of UL's		Acceleration	AL alloy, structural and vessels steels	[23, 27]
	OL-UL		Retardation	Ni-Cr and low carbon steel	[16, 29]
	UL-OL				
	Periodic OL-UL		Retardation	Low carbon steel	[16]
	Periodic UL-OL				
Block loading	Low-high		Retardation or acceleration	Ti and Al alloys, Structural steel	[12, 22, 30]
	High-low			Stainless steel, Al alloy, structural and vessels steels	[10, 11, 18, 22, 30]
	Low-high-low			Al alloy	[9]

3. Random loading

In the next sections, the term spectrum is used as a generalisation for the power spectral density (PSD).

The PSD describes how the power of a signal or time series is distributed over the different frequencies. The power is defined as the squared value of the signal. The integral of the PSD over a given frequency band computes the average power in the signal over that frequency band. In order to describe a function uniquely in the frequency domain, the amplitude and the phase versus the frequency are needed. By using only the PSD, the information of the phase is lost. A given time history has a unique power spectral density.

On the other hand, a given power spectral density does not have a unique time history. The reason is that the phase angles are discarded in the power spectral density calculation. However in fatigue analysis, the phase of the signal is not of importance. Therefore, the PSD is a good and compact way to describe a certain characteristic load signal.

Service spectra in different sectors

A lot of research has been performed towards the simplifications that might be done to complex measured spectrums, without affecting the experimentally predicted fatigue life. Several standardised spectra have been developed or proposed for different industrial sectors. Schijve [5-6] has done extensive research to the effect of a change in a flight-simulation load spectrum on the fatigue crack growth rate (FCGR). In these studies, the gust dominated spectrum TWIST and the manoeuvre-dominated spectrum FALSTAFF have been investigated.

Additionally it has been found that the sequence of loads in a spectrum has only a small effect on the FCGR.

Another standardised load spectrum called CARLOS describes the loadtime history for several automotive parts. FELIX is a standard used for the load spectrum of helicopter blades. FELIX/28 serves the same purpose, but the spectrum has been reduced for a more beneficial testing time. WISPER has been designed to describe the load spectrum of wind turbine blades. TRANSMISSION and AGRICULT. TRACTOR evaluate the torque and the bending and torsion moment in the tractor transmission and drive axle respectively. A summary of standardised spectra for multiple purposes can be found in [1]. Load spectra are often counted by different methods, such as the level crossing counting method or the rainflow method [7, 8] to evaluate linear damage accumulation. With this end, Miner's rule is applied. However a linear estimation is not always accurate since it does not consider load or interaction effects. For the better understanding of these non-linear effects, simpler loading events must be studied.

4. Simple loading

Single OL

A single overload is reported to cause a retardation (or even arrest) of the crack growth. The description of this process can be characterized by the following parameters (see Fig. 2):
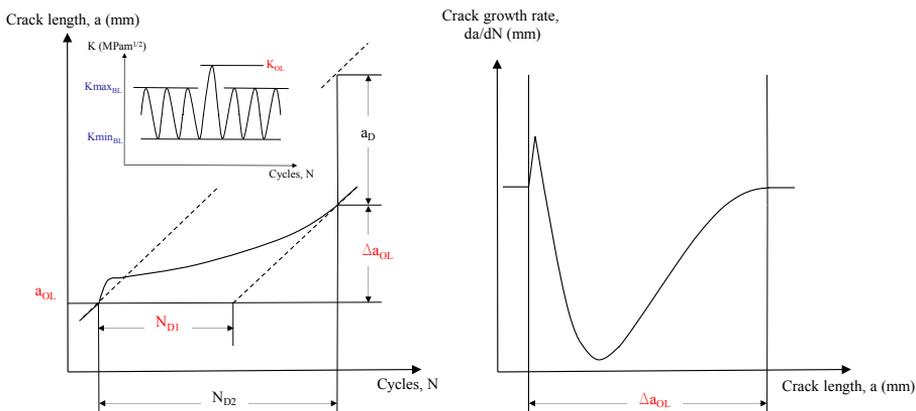

Figure 2. Schematic of delayed retardation of crack growth following a single OL in a K-controlled test, [2]

– N_D: delayed number of cycles. It can be divided into N_{D1} and N_{D2} (real
   and total number of cycles respectively)
– a_D: delayed distance (mm)
– Δa_{OL}: OL-affected crack growth increment (mm)

The main parameter influencing the FCGR (or da/dN) is the Over Load Ratio
(OLR) defined as:

$$ORL = \frac{K_{OL} - K_{\min BL}}{\Delta K_{BL}} \tag{1}$$

Increasing the OLR value will result in an increment of previous defined
parameters, and in a lower minimum da/dN level as reported in [2, 9- 21]. A
second parameter influencing the FCGR is the R-ratio. When the R-ratio is
increased, the retardation effect will diminish [2, 9-17]. Sander [9] investigated
more deeply the effect of the base-line loading. He discovered that with an
increasing baseline-level loading the retardation effect decreased.

The effect of most of the different parameters for a single OL event is
summarised on the diagram represented in Fig. 3.

When the baseline-level loading drops below ΔKth, no crack growth is
observed. An unstable crack growth occurs when the OL exceeds the fracture
toughness K_{IC} leading to overload failure. Depending on the R-ratio and the
OLR, either crack arrest (crack stops growing) or retarded crack growth (crack
growth rate is lower than predicted for the CA case) is observed. The curve
which separates these two regions is strongly influenced by R-ratio.
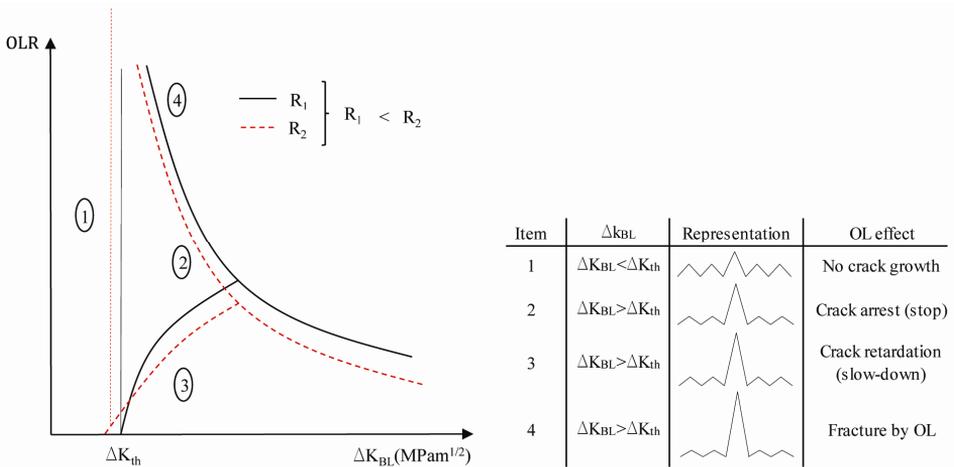

Figure 3. Influence of single overloads on the crack growth rate [modified from 9]

In general it can be stated that the retardation effect due to an overload is a
beneficial effect regarding the lifetime of components. This has also been proven

by more recent studies [9, 11, 13-17]. The retardation effect occurs in three stages as can be seen in Fig. 2. First, there is a small acceleration in fatigue crack growth rate. This acceleration is however swiftly followed by the main effect, the retardation. After the minimum crack growth rate has been obtained, thus the maximum retardation, the crack growth rate starts to accelerate again and becomes equal to the rate which would have been obtained if no overload would have been present.

Sequence of OLs
The difference between a sequence of OLs and block loading is the amount of OLs. In a sequence, only a few OLs are present, whereas in a block loading the amount of OLs is so large that they are in a regime. The retardation effect is more pronounced for a sequence of OLs than for a single overload [2, 12, 22]. Just as with a single OL, the retardation becomes more severe when increasing the OLR value [2]. An increase in the amount of OLs within the sequence will increase the retardation effect. However, the Δa_{OL} remains the same as for a single OL [2, 18]. The higher the R-ratio, the less the retardation [2, 9] which is also observed for a single OL.

Periodic sequence of OLs
For this sequence, there is not a common agreement. The result seems to depend on the combination of the number of overloads and base load cycles. If periodic single OLs are applied frequently, an accelerated fatigue crack growth might been observed for structural steels [2]. This is opposite to the observations for a single OL and a sequence of OLs. There are also several studies where the observations are in line with the ones of single OL and sequence of OLs [2, 23]. Here the main parameter controlling the retardation is the number of base cycles between the OLs. A longer interval between OLs results in a more extreme retardation [2, 22, 23].

Single UL
When applying a single UL, several authors agree that an acceleration in the FCGR takes place [2, 15, 16, 20, 24] but the rate at which the acceleration occurs is highly scattered [2]. From all analysed literature on this topic it has been concluded that overloads have more influence in the retardation effect than underloads in the acceleration effect.

Sequence of UL
Not much information is available for this load combination. According to [25], a loading change from a sequence of ULs to a base line block causes a retardation transient.

Periodic Sequence UL
It has been observed by [2, 15, 26] that the FCGR under periodic ULs goes significantly faster than the results obtained from a CA test. Yet for single

periodic ULs there is some disagreement whether or not the acceleration factor reaches a maximum or not when plotted in function of NBL [23].

An important tool to measure the effect of ULs sequences is the acceleration factor defined as:

$$AF = \frac{(\frac{da}{dN})_{VA}}{(\frac{da}{dN})_{CA}}$$
(2)

Where:
- $(da/dN)_{VA}$: measured crack growth rate per sequence
- $(da/dN)_{CA}$: the predicted growth rate per sequence by a linear summation

The Under Load Ratio (ULR) is defined as:

$$N_H \qquad N_L$$

$$R = \frac{K_{maxBL} -}{\Delta K_{BL}}$$
(3)

The FCGR response to single periodic ULs depends on the material and is strongly affected by the R-ratio [2, 27]. The ULR value however has no effect at all [2]. Whilst mostly the acceleration effect of the FCGR has been noted for periodic UL sequences, some researchers found some interaction effects [26, 28] and even retardation induced by the UL [2].

Combined overload/underload events

OL-UL or UL-OL
There is in both cases (OL followed by UL and UL followed by OL) a retardation effect. When an UL is applied immediately after an OL, it reduces the post-OL retardation more significantly than when an UL immediately precedes an OL. The retardation effect increases with increasing length of the OL sequence. Yet it has a smaller retardation effect than a pure OL sequence. The difference in effect of the UL compared to an OL-UL and OL-UL block is very small [2, 16].

In more recent studies [29], it has also been concluded that the retardation effect of an OL is very sensitive to the subsequent UL. When the UL becomes bigger, the number of delay cycles N_D decrease. The crack length affected by the delay is not dependent on the magnitude of the UL. The minimum crack length associated to the minimum FCGR varies with the UL. When the UL becomes bigger, the minimum FCGR occurs later [29]. In [16] it has been concluded that the influence of an UL can make the retardation effect due to an OL go away.

Periodic OL-UL or Periodic UL-OL
A periodic behaviour of an OL immediately followed by an UL or vice versa will most likely cause a retardation in crack growth rate. There exists a maximum in retardation for a certain period of applied BLs and the effect of

change in FCGR eventually disappears when the period becomes very large [16].

5. Block loading

In general, block loadings can be categorised in low-high, high-low or combinations of these sequences.

The main parameters to define the blocks are (see Fig. 4a):

- R
- ΔK
- Kmin
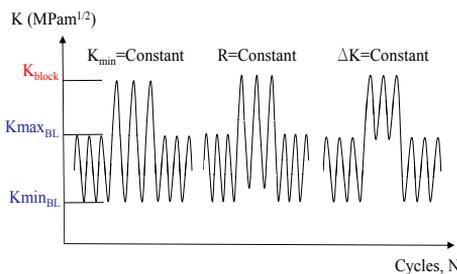
Figure 4a. Characteristic parameters in a L-H-L block loading system [9]
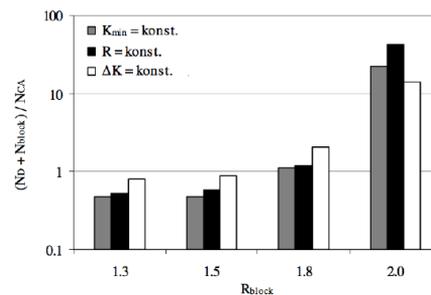
Figure 4b. Total lifetime vs. block loading ratio for 3 different loading configurations [9]

In Fig. 4b the lifetime normalized to the CA fatigue life is illustrated depending on the block loading ratio and the block loading category is defined. The CA reference fatigue loading corresponds to the base loading. The lifetime due to high-low block loading increases exponentially with increasing block loading ratio [9].

In [30], high-low and low-high blocks were tested with constant ΔK. The effect of a high-low block has the same trend as a single OL (see Fig. 1). However, for a high-low load block, the retardation always occurs immediate and is not preceded by the acceleration phase [10, 18]. The effect of crack retardation is much higher for the high-low block than for an equivalent single tensile overload [11, 22, 30]. The low-high block results in an acceleration of FCGR. This behaviour is identical to that generally observed following an UL [2, 12, 22]. Also the effect of the R-ratio has been investigated by Borrego [30]. A significant reduction in delay cycles when R is increased has been observed. This is a similar behaviour as in single OL [10, 11, 14].

6. Overview of crack propagation mechanisms

Notwithstanding retardation and acceleration effects have been mentioned, nothing about the physics behind these effect has been said.

Crack tip blunting is one of the phenomena to explain the retardation [3]. Due to an overload, the crack tip is blunted, creating a new initiation site. Before the crack can propagate further at a normal ratio, it has to be reinitiated which causes retardation.

According to [3], an OL induces compressive residual stresses ahead of the crack tip. By superimposing these stresses on the applied stresses, the local stress ratio reduces. Thus the compressive residual stresses induced by an OL can also be seen as a reason for FCGR retardation due to an OL. Elber [31] identified the phenomenon of plasticity-induced crack closure (PICC) and was able to fully explain all stages of retardation. Due to the OL, large tensile deformations are induced in the material ahead of the crack tip. This zone affected by the OL, is called the OL plastic zone.

An increase in residual wake of plastic deformation is left on the crack flanks when the crack advances through this zone. This increase causes the crack to stop at high tensile loads. The PICC models predict delayed retardation. If the OL caused direct crack branching, immediate retardation is to be expected.

However when the crack after the OL first starts to grow in a normal way and branches afterwards, delayed retardation occurs. This study was later confirmed by [16]. Jones [32] made a suggestion that the high plastic strains induced by the OL harden the region ahead of the crack tip and cause the retardation. In general, the PICC phenomenon has been most prominent to account for crack retardation in a single OL. It has been confirmed by several researchers [33-35, 22] and numerical analysis [10, 36]. Also the effect of the OLR and the R-ratio are in accordance with the PICC arguments [10].

The residual stress concept has been used to prove the acceleration effect upon a single UL [3, 16, 33-35, 22] as the UL induces tensile residual stresses ahead of the crack tip. Also the PICC mechanism is able to prove the acceleration. An UL reduces the height of plastically deformed material in the area behind the crack by compressive yielding [3].

Table 2. Overview of crack propagation mechanisms

Mechanism	OL	UL
Crack tip blunting	x	
Compressive residual stresses	x	
Tensile residual stresses		x
PICC	x	x

Conclusions

There has been done a lot of research to describe load spectra of different applications. Notwithstanding numerous research efforts, the effects of VA loads

are still not fully understood. Most research has been done on the effect of a single OL. It can be concluded that an OL and all of its variations have a retardation of the crack growth as a consequence. ULs however have an acceleration of crack growth as a consequence. When an OL and an UL are applied after each other, retardation is most likely to occur, but the UL has a strong influence on the amount of retardation. For block loading, the effect highly depends on the parameters defining the shape of the block. The plasticity induced crack closure (PICC) mechanism has been proven useful to explain retardation and acceleration effects.

References

[1] P. Heuler, T. Bruder, H. Klatschke - Standardised load-time histories – a contribution to durability issues under spectrum loading – Mat.-wiss. U. Werkstofftech. 2005, 36, No. 11 – DOI: 10.1002/mawe.200500936.

[2] M. Skorupa, "Load interaction effects during fatigue crack growth under variable amplitude loading - a literature review. Part I: empirical trends," Fatigue & Fracture of Engineering Materials & Structures, vol. 21, no. 8, pp. 987–1006, 1998.

[3] M. Skorupa, "Load interaction effects during fatigue crack growth under variable amplitude loading - a literature review. Part II: qualitative interpretation," Fatigue & Fracture of Engineering Materials & Structures, vol. 22, no. 10, pp. 905–926, 1999.

[4] J. Schijve - Fatigue of structures and materials - ISBN-13:978-1-4020-6807-2 – 2003.

[5] J. Schijve, "The significance of flight simulation fatigue tests.," Durability and Damage Tolerance in Aircraft Design, Proc. 13th ICAF Symp., Pisa (Edited by A. Salvetti and G. Cavallini), EMAS,Warley, pp. 71 – 170, 1985.

[6] J. Siegl and J. J. Schijve, "Fractographic observations on fatigue crack growth under minitwist flight simulation-loading.," LR-631, Delft University of Technology, The Netherlands., 1990.

[7] J.P. Amzallag, C. Gerey, J.L. Robert, and J. Bahuaud, "Standardization of the rainflow counting method for fatigue analysis". Fatigue, vol. 16, pp. 287 – 293, 1994.

[8] A. K. Khosrovaneh, "Fatigue loading history reconstruction based on the rainflow technique". International Journal of Fatigue, vol. 12, pp. 99 – 106, 1990.

[9] M. Sander and H.A. Richard, "Fatigue crack growth under variable amplitude loading. part I: Experimental investigations.," Institute of Applied Mechanics (FAM), University of Paderborn, Pohlweg 47-49, D-33098 Paderborn, Germany, 2005.

[10] C. S. Shin and S. H. Hsu, "On the mechanisms and behaviour of overload retardation in AISI 304 stainless steel" Int. J. Fatigue, vol. 15, pp. 181– 192, 1993.

[11] L.P. Borrego, J.M. Ferreira, and J.M. Costa, "Evaluation of overload effects on fatigue crack growth and closure" Eng Fract Mech, vol. 70, pp. 1379–1397, 2003.

[12] C. M. Ward-Close, A. F. Blom, and R.O. Ritchie, "Mechanisms associated with transient fatigue crack growth under variable-amplitude loading: An experimental and numerical study," Engineering Fracture Mech. 32, pp. 613–638, 1989.

[13] L.P. Borrego, J.M. Ferreira, and J.M. Costa, "Fatigue crack growth and crack closure in an AlMgSi alloy" Fatigue Fract Eng Mater Struct, vol. 24, pp. 255 – 266, 2001.

[14] X.P. Huang, J.B Zhang, W.C. Cui, and J.X. Leng, "Fatigue crack growth with overload under spectrum loading" Theor Appl Mech, vol. 44, pp. 105 – 115, 2005.

[15] V. Tvergaard, "Effect of underloads or overloads in fatigue crack growth by crack tip blunting" Eng Fract Mech, vol. 73, pp. 869 – 879, 2006.

[16] F. Romeiro and M. de Freitas, "The effect of overloads and underloads on fatigue crack growth" Anales de Mecanica de la fractura, vol. 18, pp. 79 – 85, 2001.

[17] R. Seifi, M. Eshraghi, "Effects of mixed-mode overloading on the mixed-mode I+II fatigue crack growth", Arch. Appl. Mech., Vol. 83, pp. 987–1000, 2013.

[18] G. L. Chen and R. Roberts, "Delay effects in AISI 1035 steel" Engng Fracture Mech., vol. 22, pp. 201–212, 1985.

[19] R.L. Carlson, G.A. Kardomateas and P.R. Bates, "The effects of overloads in fatigue crack growth". International Journal of Fatigue, Vol. 13, No. 6, pp. 453 – 460, 1991.

[20] K. Sadananda, A.K. Vasudevan, R.L. Holtz and E.U. Lee, "Analysis of overload effects and related phenomena". International Journal of Fatigue, Vol. 21, pp. 233 – 246, 1999.

[21] B. B. Verma and R. K. Pandey, "The effects of loading variables on overload induced fatigue crack growth retardation parameters". Journal of material science, Vol. 34, pp. 4867– 4871, 1999.

[22] M. Skorupa, J. Schijve, A. Skorupa and T. Machniewicz, "Fatigue crack growth in a structural steel under single and multiple periodic overload cycles", Fatigue Fract Eng Mater Struct, Vol. 22, pp. 879 – 887, 1999.

[23] N. A. Fleck, "Fatigue crack growth due to periodic underloads and overloads". Acta Metall., vol. 33, pp. 1339 – 1354, 1985.

[24] F.S. Silva, "Fatigue crack propagation after overloading and underloading at negative stress ratios",
International Journal of Fatigue, vol. 29, pp. 1757 – 1771, 2007.

[25] D.J.T. Carter, "Estimation of wave spectra from wave height and period". Institution of oceanographic sciences, I.O.S. Report No. 135, 1982.

[26] R. L. Carlson and G. A. Kardomateas, "Effects of compressive load excursions on fatigue crack growth". Fatigue, vol. 16, pp. 141 – 146, 1994.

[27] T.H. Topper and M.T.Yu, "The effect of overloads on threshold and crack closure". Int. J. Fatigue, vol. 3, pp. 159 – 164, 1985.

[28] R. Yang, "Prediction of crack growth under complex loading cycles". Int. J. Fatigue, vol. 16, pp. 397 – 402, 1994.

[29] A. Bacila, X. Decoopman, G. Mesmacque, M. Voda, and V.A. Serban, "Study of underload effects on the delay induced by an overload in fatigue crack propagation". International Journal of Fatigue, vol. 29, pp. 1781 – 1787, 2007.

[30] L.P. Borrego, J.M. Ferreira, and J.M. Costa, "Partial crack closure under block loading". International Journal of Fatigue, vol. 30, pp. 1787 – 1796, 2008.

[31] W. Elber, "Fatigue crack closure under cyclic tension". Engineering Fracture Mechanics, vol. 2, pp. 37–45, 1970.

[32] R. E. Jones, "Fatigue crack growth retardation after single cycle peak overload in Ti6Al4v titanium alloy" Engng Fracture Mech., vol. 5, pp. 585 – 604, 1973.

[33] M. A. Meggiolaro and J. T. Pinho de Castro, "On the dominant role of crack closure on fatigue crack growth modeling". International Journal of Fatigue, Vol. 25, pp 843 – 854, 2003.

[34] P. Dai, S. Li and Z. Li, "The effects of overload on the fatigue crack growth in ductile materials predicted by plasticity-corrected stress intensity factor". Engineering fracture mechanics, Vol. 11, pp. 26 – 37, 2013.

[35] T. Manson, H. Öberg and F. Nilsson, "Closure effects on fatigue crack growth rates at constant and variable amplitude loading". Engineering fracture mechanics, Vol. 71, pp. 1273 – 1288, 2004.

[36] X. Zhang, A. S. L. Chan, and G. A. O. Davies, "Numerical simulation of fatigue crack growth under complex loading sequences". Engng Fracture Mech., vol. 42, pp. 305 – 321, 1992.

[37] M. Skorupa and A. Skorupa, "Experimental results and predictions on fatigue crack growth in structural steel", International Journal of Fatigue, vol. 27, pp. 1016 – 1028, 2005.

TRANS-TRIO SCIENCES
Gent •Gödöllő • Baia Mare

The effect of the position of pistons of piston's
circular top face onto the deformation
of the piston's wall

The effect of the position of pistons of piston's circular top face onto the deformation of the piston's wall

Ádám HORVÁTH[1], István OLDAL[2], Gábor KALÁCSKA[1],
Mátyás ANDÓ[3]

[1]Institute for Mechanical Engineering Technology, Szent István University,
[2]Institute for Mechanics and Machinery, Szent István University,
[3]Institute of Technology, Universty of West Hungary, Szombathely,

Abstract

In connection with vehicles several researches deal with different areas to increase the performance of the motor vehicle or more economical function can be reached. One of these areas is wheel drive where one of the most important parts is disc brake. The main parts of disc brake are the pistons so in this study piston's behavior was examined in the moment of car braking. Hydraulic pressure has an effect on piston's behavior and the piston's wall is deformed. The sealing ring has two positions in the brake system; one of them, when sealing ring is in caliper (SIC), the other when the sealing ring is in the piston (SIP). The effect of the piston's geometry on the deformation was examined where circular top face positon changed. Optimal construction was defined in two cases (SIC, SIP) where deformation of the critical direction (positive X direction) is in minimum. When the sealing ring is in the caliper the optimal position of circular top face is 5,7 mm from the top, meaning that optimal position is 19,5 % for the length of piston. When the sealing ring is in the piston the optimal position of the circular top face is 16 mm from the top, meaning that optimal position is 55 % for the length of piston. The piston's geometry effects the deformation of the wall, and the optimal geometry is different which is deal with the sealing ring position (SIC, SIP).

Keywords

FEM, brake piston, deformation, optimization

1. Introduction

One of the most dynamically expanding industry of our time is the motor industry where a number of areas are developed to give impetus to research The aim of the research is to devise how the performance and more economical function should

The effect of the position of pistons of piston's
circular top face onto the deformation
of the piston's wall

ISO ⚙ ⱷ   TRANS–TRIO SCIENCES
Gent •Gödöllő • Baia Mare

be increased. (Holmberg, et al., (2012). Several researchers examined the drive and performance of drive. (Duckhan, et al., (2014). The aim of these researches is to decrease the loss to direct the energy gained from the fuel to the drive of the motor vehicle. Researchers used different materials which friction on each other to find the optimal material (Rejowski, et al., (2014) and examined the lubricant to see the effectiveness. (Tasdemir, et al., (2014). In the interest of reduction of the losses and increase of the performance an efficient kinetic energy recovery system is applied to recycle the braking energy used in the city or acceleration. (Gu et al., (2013). Another area is the bodywork of vehicles where the aim of the research is reduced to the net weight of the motor vehicle. Several kinds of new material were used to reduce the mass that has little density and big solidity. (Feraboli, et al., (2004) One research direction is to increase the power-to-weight ration, the other is body shape where wind resistance factor is small, increasing the performance and reducing the fuel utilization. (Song, et al., (2012). In case of vehicles an important development area is the wheel drive and within this the development of the braking system. The performance of the car has an effect on the brake system's performance, because brakes should be suitable for stopping and slowing down the car. When brakes are at work high temperature is created between friction materials (Yaoqing, et al., 2014) that effects the brake's performance. The high temperature decreases the friction coefficient between brake pad and brake disc. (Neis, et al., 2011). Some researches examine which materials would be capable of keeping the value of the friction coefficient in specific value when temperature is growing. In this research we examine different components that influence the friction coefficient and keep its specific value. (El-Tayeb, Liew (2008). Wear is another important part of research where researchers measured and defined the wear when car was braking. (Neis, et al., (2014) The other frictional element is the brake disk, which creates the suitable brake torque when it is rubbed on the brake pad. The high temperature influences the brake disc, so some research examines different constructions to increase cooling or find optimal material which is less sensitive to temperature. (Yan, et al., (2015). The majority of the researches concerned with the braking systems are concentrated onto a friction element pair and the additional parts of the braking system are not examined. Hardly any research deals with the behavior of the calipers and the pistons in the caliper. (Horváth., et al., (2015)

The aim of this study is to examine the piston's behavior in the two cases where sealing ring position was changed. Optimal geometry was defined where circular top face position was changed. Deformation of the wall of the piston was defined to find the optimal construction for the sealing ring in the caliper and in the piston.

2. Materials and method

The material of the piston must be of little density because high performance caliper has 2, 4, 6, 8 pistons which weight increases the unsprang mass that

S ⚙ 囚 TRANS-TRIO SCIENCES
Gent • Gödöllő • Baia Mare

The effect of the position of pistons of piston's
circular top face onto the deformation
of the piston's wall

effects the maneuverability. The sufficient strength is important for pistons because hydraulic pressure deforms the pistons which do not work well. Because of these requirements aluminium alloy piston was used. 7075t6 aluminium has been used in several places, for example: airplane, racket, gear, etc. The properties of 7075t6 are shown in table 1. In this study piston and piston environment was examined where simplified model was used. In this model the brake pad was made of two parts, one is friction material, the other is steel plate. The friction material and disc brake makes the braking torque. Properties of brake pad are demonstrated in table 1. (Choi, Lee (2004), (Belhocine, Bouchetara,2012).

Table 1. Material's parameters

	Young modulus [GPa]	Poisson Ratio
Aluminium alloy piston (3.4335)	71	0,3
Steel plate (1.0039)	210	0,3
Friction material	1	0,25

The piston examination is in finite element program (Ansys Workbench V11). A simplified model was used to gain the result that was checked earlier (Horváth., et al., 2015). 2D axisymmetric model was used where brake pad and piston was modeled. (Figure 1/a). Deformation of the piston's wall was defined in 30 points which is outside of wall (figure 1/a). After that constraint was defined in the model. The displacement of point which is on the symmetry axis is 0 mm in X direction. The other constraint is in fiction surface, where brake pad is connected to the brake disc, displacement in y direction is 0 mm. Constrains used in the model is in figure 1/b. The study is set to find the optimal geometry (circular top face position was changed) where deformation of the wall is the smallest. The pistons diameter is 44 mm (radius 22 mm) and the piston's length is 29 mm.
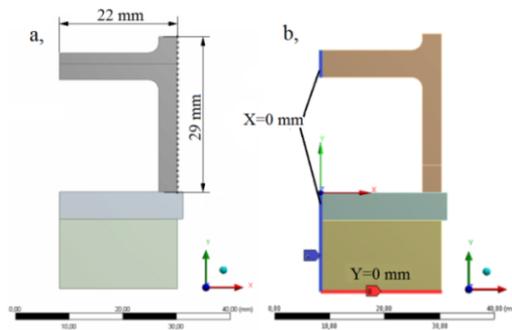

Figure 1. (a) Geometry of model and examined dots,
(b) Constrains

The effect of the position of pistons of piston's
circular top face onto the deformation
of the piston's wall

TRANS–TRIO SCIENCES
Gent •Gödöllő • Baia Mare

The circular top's face thickness is 5 mm, whose position was changed from top to bottom. (Figure 2) The position of circular top face effect was defined to the deformation of wall.


8 mm

16 mm

24 mm
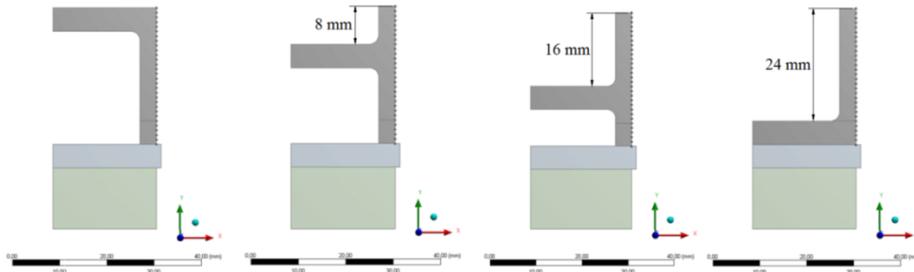
Figure 2. Piston's circular top face positon in different case

Sealing ring positon is different in caliper, two places were used in caliper. First, the sealing ring is within the caliper (SIC), where hydraulic pressure effect to the pistons wall. In the other case the sealing ring is in the piston. In this case the hydraulic pressure does not effect the piston's wall. Figure 3 shows how we defined the pressure in the model.


a,   P=15 MPa   b,   P=15 MPa
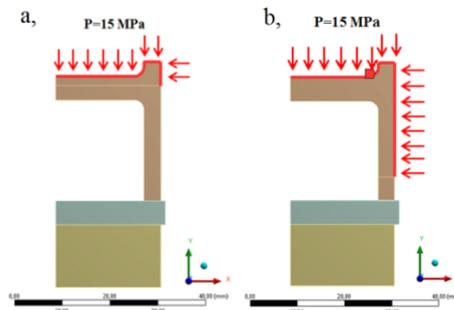
Figure 3. Pressure applied on a model in different case: (a) sealing ring in piston (SIP),
(b) Sealing ring in caliper (SIC)

Hexagonal element was used in all parts of the model, the size of the elements is 2 mm that gives suitable result when deformation was defined. Depending on the model the number of elements is 310 elements which gives 1100 nods.

3. Results

In the course of the examination of the circular top face of the piston in the two examined cases (SIP, SIC) the received results are different. Figure 4 shows the

The effect of the position of pistons of piston's
circular top face onto the deformation
of the piston's wall

deformation (in fivefold magnification) in the case of a given piston. In this case the circular top face is 8 mm to the top.
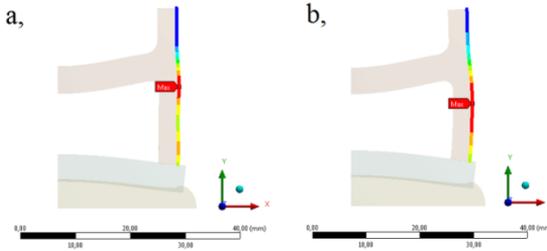

Figure 4. Wall of piston deformation when cirkular top face is 8 mm:
(a) Sealing ring in caliper (SIC), (b) Sealing ring in piston (SIP)

Deformation of wall was defined in all cases and the result was depicted in diagram. Figure 5 shows the deformation of piston's wall when the sealing ring is in the caliper. The distance of the examined dots is 1 mm and the first dot is in top and 29 dots are in bottom where piston is connected to brake pad. In the other case the sealing ring is in the piston and the deformation is in figure 6. Results show that deformation is different and higher than in the first case. All different model stresses were examined and concluded that stress does not exceed the yield point that is 280 MPa.
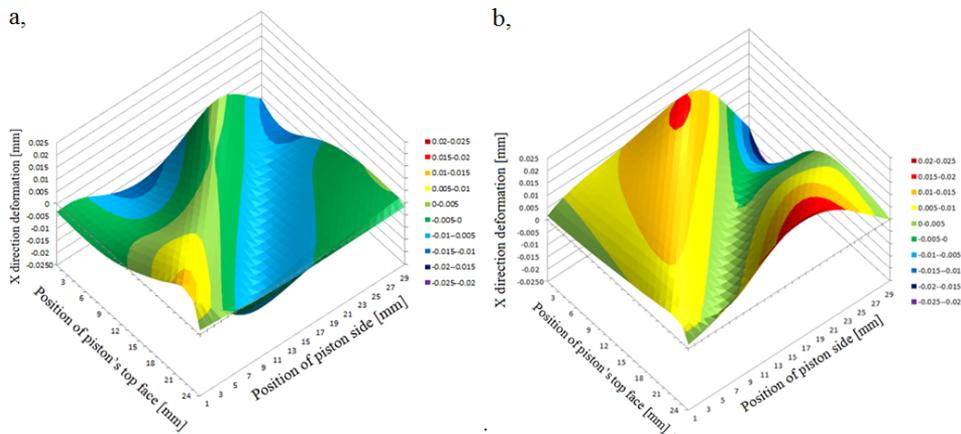

Figure 5. (a) Wall of piston deformation in the case of sealing ring being in caliper (SIC) (b) Deformation of the wall of piston in the case of sealing ring being in piston (SIP)

4. Discussion

Results show that piston's geometry and sealing ring position influence the piston's wall deformation and the measure of deformation. The result of the

The effect of the position of pistons of piston's
circular top face onto the deformation
of the piston's wall

change of the piston's geometry seems to be that deformation is different in all cases and the measure of deformation depends on the sealing ring's position. The optimal geometry (minimal deformation) results in brake system becoming safe, because pistons do not stuck into caliper. In the course of braking the place between caliper and piston decrease, in critical cases pistons connect cylinder of caliper and stuck into caliper. In two cases (SIC, SIP) piston's geometry has been optimized (smallest deformation in positive X direction). All geometry critical cross-section was defined where positive X direction deformation is largest and in which case that deformation is smallest. Figure 6 shows the deformation of the wall (absolute value) and positive X direction deformation when sealing ring is in the caliper. Deformation of positive X direction shows which construction is optimal. When circular top face is near the brake pad or full surface presses brake pad, the brake pad effects the deformation of wall. Figure 6/a shows that optimal construction is not this, so this model was not examined further. In this case, with sealing ring in caliper an optimal construction was defined. Figure 6/b shows that optimal position of circular top face is 5.7 mm to the top. Wall deformation in this construction is 0.000122 mm.
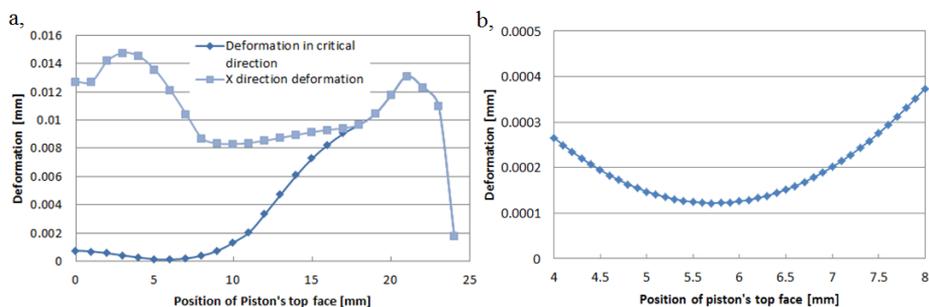

Figure 6. a,Wall of piston's deformation (deformation in an absolute value, deformation in critical direction) when sealing ring in the caliper; b, Minimum deformation of critical direction (SIC)
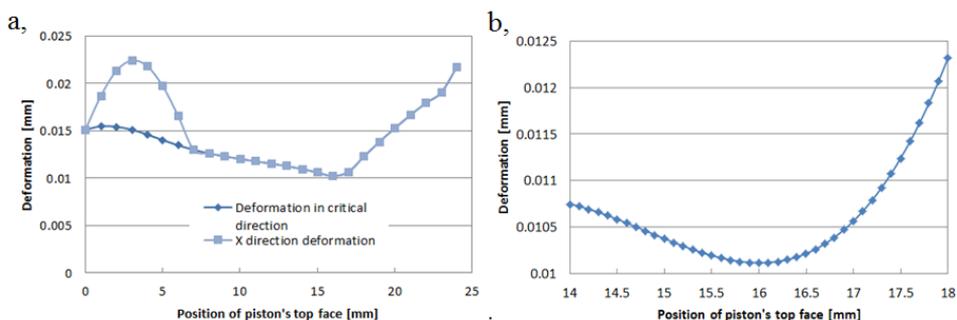

*Figure 7.*a, Wall of piston deformation (deformation in an absolute value, deformation in critical direction) when sealing ring in caliper; b, Minimum deformation of critical direction (SIP)

The effect of the position of pistons of piston's
circular top face onto the deformation
of the piston's wall

When sealing ring is in the piston (SIP) the value of deformation is higher (Figure 7/a), but in this case optimal construction was found where positive X direction deformation is smallest. The optimum point is near the middle of the piston's length, because circular top face decreases the measure of convex effect of piston. In this case, the optimal position of circular top face is 16 mm to top, where wall deformation is 0.0101 mm. Figure 7/b shows the optimum point and its environment.

Result suggests that the two cases where sealing ring positon was changed (SIC, SIP) the optimum point was found where positive X direction deformation is smallest. When sealing ring is in the caliper (SIC) it has a good effect, because hydraulic pressure presses piston's wall and decreases the positive X direction deformation. That means the pressure increases the place between the cylinder of caliper and the piston. In the other case (SIP), this good effect is not working, so circular top face position is near the middle of the piston's length, so it decreases harmful deformation. Comparing deformation in these two cases, the measure of deformation is smaller when sealing ring is in the caliper. Deformation in critical cross-section is a hundred times bigger when sealing ring is in the piston, because hydraulic pressure does not put pressure on the piston's wall in the center of the piston. As opposed to traditional forming (where circular top face is in top of piston), the deformation decreases 85% when sealing ring is in caliper, which means that piston is not stuck into the caliper.

This study demonstrates where the optimal position of circular top face is. When sealing ring is in the caliper the optimal position of top face is 19.5 % of piston's length (Figure 11/a). In the other case, when sealing ring is in the piston the optimal position of top face is 55 % of piston's length (Figure 11/b).
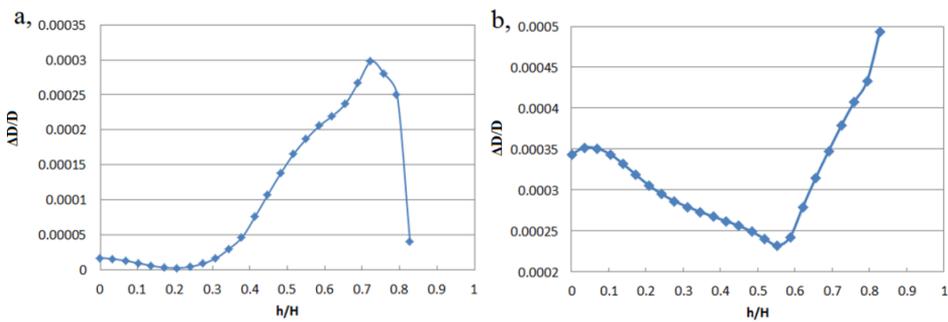
Figure 11. Optimal construction when (a) sealing ring in caliper (SIC),
(b) sealing ring in piston (SIP)

Summary

One of the most important research areas of vehicles is the braking system, especially the disk brakes. Several researches examine friction elements for example brake disc, brake pad etc. A few study examined the pistons in the

The effect of the position of pistons of piston's
circular top face onto the deformation
of the piston's wall

caliper, which press the brake pad to the disc. When a car is braking the hydraulic pressure presses the piston and causes deformation. High deformation is damaging, because the piston's diameter increases and critical case the piston stuck into caliper. In this study we suggested that the optimal geometry decreases the critical deformation measure. Two cases were examined: in one case the sealing ring is in caliper (SIC), in the other case sealing ring is in piston (SIP). In first case (SIC) the hydraulic pressure presses the wall of the piston which is increase the place between cylinder of caliper and piston. In second case (SIP) the hydraulic pressure does not effect the wall, deformation only presses the circular top face. This study shows how change deformation when circular top face position was changed. In both cases (SIC, SIP) the optimum point was defined where positive X direction (critical direction) deformation is smallest.

When sealing ring is in the caliper the optimal position of circular top face is 5.7 mm to the top, where critical direction deformation is 0.000122 mm. As opposed traditional forming (where circular top face is in top of piston), the deformation is decrease 85% when sealing ring is in the caliper. When sealing ring is in the piston the circular top face optimal position is 16 mm to the top, where deformation is 0.0101 mm. These results show that deformation is smaller when sealing ring is in the caliper. When sealing ring is in the caliper the optimal position of top face is 19.5 % of piston's length and 55 % of piston's length when sealing ring is in the piston.

References

[1] A. Belhocine, M. Bouchetara (2012) Thermomechanical modelling of dry contacts in automotive disc brake, International Journal of Thermal Sciences 60, 161-170

[2] Duckhan K., Seonghwan K., Sehun O., Soo-Young N., (2014), Engine performance and emission characteristics of hydrotreated vegetable oil in light duty diesel engines, Fuel 125, p. 36-43

[3] E. D. Rejowski, M. C. L. Oliveira, R. A. Antunes, M. F. Pillis, (2014), Structural Characterization and Corrosion Stability of a Si-Doped DLC Coating Applied on Cylinder Liner, Journal of Materials Engineering and Performance 23, p. 3926-3933

[4] H. A. Tasdemir, M. Wakayama, T. Tokoroyama, H. Kousaka, N. Umehara, Y. Mabuchi, T. Higuchi, (2014), The effect of oil temperature and additive concentration on the wear of non-hydrogenated DLC coating, Tribology International 77, p 65–71

[5] H.B. Yan, Q.C. Zhang, T.J. Lu, (2015), An X-type lattice cored ventilated brake disc with enhanced cooling performance, International Journal of Heat and Mass Transfer 80, p. 458–468

[6] Horváth Á., Oldal I., Kalácska G., (2015) Modelling possibilities of pistons in brake caliper, International Multidisciplinary Conference, pp.73-76

The effect of the position of pistons of piston's
circular top face onto the deformation
of the piston's wall

[7] J. Choi, I. Lee (2004) Finite element analysis of transient thermoelastic behaviors in disk brakes, Wear 257, 47-58

[8] J. Gu, M. Ouyang, D. Lu, J. Li, L. Lu, (2013) Energy efficiency optimization of electric vehicle driven by in-wheel motors, International Journal of Automotive Technology, Vol. 14, No. 5, pp. 763−772

[9] K. S. Song, S. O. Kang, S. O. Jun, H. I. Park, J. D. Kee, K. H. Kim, D. H. Lee, (2012), Aerodynamic design optimization of rear body shapes of a sedan for drag reduction, International Journal of Automotive Technology, Vol. 13, No. 6, pp. 905−914

[10] K. Holmberg, P. Andersson, A. Erdemir, Global energy consumption due to friction in passenger cars, Tribology International 2012 47 221–234.

[11] N.S.M. El-Tayeb, K.W. Liew, (2008),Effect of water spray on friction and wear behaviour of noncommercial and commercial brake pad materials, Journal of Materials Processing Technology 208, p. 135–144

[12] P. D. Neis, N. F. Ferreira, F. P. da Silva (2014), Comparison between methods for measuring wear in brake friction materials, Wear319, p. 191–199)

[13] P. Feraboli, A. Masini, (2004), Development of carbon/epoxy structural components for a high performance vehicle, Composites: Part B 35, p. 323–330

[14] P.D. Neis, N.F. Ferreira, F.J. Lorini, Contribution to perform high temperature tests (fading) on a laboratory-scale tribometer, Wear 271, (2011) p. 2660-2664

[15] Yaoqing W. • Hongyun J.,Yunlong L.,Zhengjia J., Shuen H., (2014), Simulation of Temperature Distribution in Disk Brake Considering a Real Brake Pad Wear, Tribol Lett 56, p. 205–21

Effect of the different loads onto the friction and stick-slip of polyamide composites

László ZSIDAI, Zoltán SZAKÁL

Szent István University, Faculty of Mechanical Engineering –
Institute for Mechanical Engineering Technology, Gödöllő

Abstract

Our present work is connected to a research project, which is based on PA6, POM, PET and PEEK polymer matrix and aimed at making a map of the features of tribology. Our work analyses the friction and connection with this, and the stick-slip behaviour of polyamide composites with different load relations. The friction tests are prepared in alternating (Reciprocating) cylinder/plane model system, developed in both the dynamic and the static friction force which is continuously measured. T**his special tribology test system** is extremely suitable to investigate among other things the stick-slip phenomenon also. You can find detailed presentation in our earlier articles. Expected results from our research may serve in a context the effect of the different loads have on a static and dynamic friction. Our research shows the effects of friction on different levels and susceptibility of the tested materials in this direction in the stick-slip PA6 and PA66 composites.

Keywords

friction, PA6, load, polymer, composites, stick-slip

1. Introduction

Our work is part of a larger research project that deals with the tribology behaviour of engineering polymer composites. The present paper shows the friction results of the different polyamide composites/steel pairs in connection with the different loads (50N and 150N). We used a reciprocating cylinder-on-plate test apparatus, no external lubricants were added to the tribological system. Our research shows an overview about the results (static and dynamic friction coefficients) and the effects of different loads in connection with their stick-slip behaviours also.

Base Principles
The tribological properties of polymers strongly depend on the sliding surface [Zsidai, Szakál (2014)] and the tests parameters (velocity, ambient temperature, humidity etc.) mainly on the load. Several studies on the tribological behaviour of common engineering plastics e.g. Uetz, Wiedemeyer (1985), Kalácska, et al.,

(1997), Yamaguchi (1990), Kalácska (2007, 2013) in contact with steel have been published and compared by, e.g., Tanaka (1982), and Evans (1982). We can find in the research character in connection with base polyamide, Byett (1992), De Velde, De Baets (1997), Keresztes (2010) Yamamoto et al. (2002) in sources also. The number of the articles dealing with the composites is growing nowadays, e.g., Friedrich et al. (1995), G. Kalácska, ed. (2007), Sumer et al. (2008) and Schroeder et al. (2013).

– The tribology examinations nowadays are mainly done with small-scale and large-scale tests which are available in literature to be referenced, e.g. G. Kalácska, et al. (1999), Sukumaran, et al. (2012), **Zsidai, et al. (2002).** These several benefits, e.g. simple test rig with low forces and power, reduced cost for preparing test specimens, easier to control the environment.

– From our earlier examinations: **Zsidai, Szakál (2014), Zsidai et all. (2014), Zsidai, Kalácska (2014), Zsidai et all.**(2015) it is clear already, that the alternating tribo examination system is very useful in examining the characteristics of the stick-slip, therefore we continue to use this system. We can find more publications about the role of the stick-slip tribology also e.g. Bruska at all (2006).

Among the examined materials from the engineering polymers, are there the several of the variant composites based on PA6 (polyamide 6), and one type of PA66 polymer matrix (with a charged lubricant and/or with thread strengthening), we used mating plates made of steel for this application.

I characterize the polymers with tribology examinations, taken into consideration a results of the friction (static and dynamic).

Goals:

The main objectives of the investigation is, the comparison of reciprocating friction of different polyamide composites in connection with the effect of different normal load and describe their stick-slip behaviours.

Further goals of the research are to determine the optimal operational conditions of the selected polymers, to help with the selection of a proper polymer for certain conditions, and to find out the causes of friction.

2. Test Rigs, Materials And Results

The present paper describes the linear sliding friction measurements of the different polymer/steel pairs using a reciprocating cylinder-on-plate test apparatus. No external lubricants were added to the tribological system.

The experimental tribo- model system as pictured in figure 1 is essentially a variant of the commercially available reciprocating tribotest.

Detailed description of the test system and evaluation of the test results can be found in my publication see. [Zsidai, Kalácska (2014), Zsidai, Szakál (2014)]
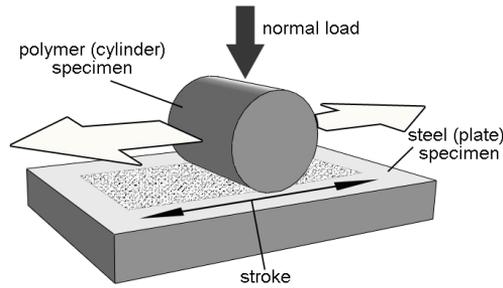
Figure 1. Reciprocating model system

Test conditions

All experiments are performed at ambient conditions of temperature and humidity (30 °C and 50% RH). The various conditions of the performed small-scale tests are gathered in Table 1.

Table 1. Parameters of tests

Parameters	Values
Surface of steel specimen, R_z [μm], (R_a [μm])	1,7 (0,16)
Running time, t (sec)	130
Normal load, F_N [N]	50 and 150
Frequency, f [Hz]	10
Velocity, v [m/s]	0,05
Stroke, s [mm]	6
Humidity, RH [%]	50
Ambient temperature, T (◦C)	30

Tests are conducted with normal load: 50 and 150 N. The running time (130 sec.) of the tests is chosen to observe the first (running in stage) period of the friction. For each test, the surface roughness's of the steel specimen that were used R_z 1,7. The tribological data described below result from an average of three runs with identical experimental parameters.

Materials and preparation of test specimens

The selection of the 5 tested polyamide composites was based on the database of polymer producers, end-users and expertizing companies in this field. The finally selected engineering polymers can be taken as generally used engineering materials in the industry in sliding systems. Some of these polyamides are well-known but some composites are just being introduced in the market.

The materials are PA composites group. One of them is PA66 (PA 66MH) and the other is with PA6 (PA 6E, PA 6GELS, PA 6MO, PA6GLIDE) base matrix are included in the experiments.

Material of the mating plate
The counter plates are made of widely used, C45 general purpose steel. The application area of C45 is a less demanding but wear-proof. The heat conduction: 46 W/(mK) and the standard is EN 10083. The plate dimensions are 200×100×12mm and grinding is used for the preparation of steel surfaces (R_a=0,11-0,18 μm ≈ R_z=1,4-1,7μm). The grinding grooves are made parallel to the sliding direction during the wear tests. Roughness is measured perpendicular to the sliding direction.

Materials of the polymer cylinders
– The polyamides PA 6E of the extruded type, were used as a reference material in the investigations. The PA 6E favourable combination provides the rigidity, toughness, mechanical damping ability and resistance wear of polyamide product „general purpose" type called.
– The PA 6G ELS is the conductive version of magnesium catalysed cast polyamide 6.
– The PA 6MO (PA 6E+MoS2) for molybdenum disulphide (MoS2) content greater strength and stiffness than the PA 6E. The heat and wear resistance are also improved, but the toughness and mechanical damping capacity worse.
– PA6 GLIDE is a hard semi-crystalline cast polyamide with good sliding properties, wear resistance, oil-, grease-, gasoline-, gas oil resistance and easy machinability.
– PA 66 MH shows good sliding properties, stiff, high resistance to oils, greases, petrol, gas oil, UV and weather resistance, electrical insulation and easy machinability. In shipping, packaging structures, electronic equipment, printers, and precision engineering are used.
  Table 2 gives an overview of the properties of the tested engineering plastics. Among these properties the E-modulus can be used to characterise the adhesion friction component, since it is correlated with the chain flexibility.

Table 2. Mechanical and physical properties of the tested polymers [1], [2]

Material code	colour	density [g/cm³]	Tensile strength at yield/ Modulus of Elasticity [MPa][1]
PA 6E	black	1,13	85/3000
PA 6G ELS	black	1,15	70-110/-
PA 6MO	black	1,14	82/3300
PA 6 GLIDE	green	1,13	76/3200
PA 66 MH	black	1,14	75/2500

[1] Values referring to material in equilibrium with the standard atmosphere 23 ∘C/50% RH

The polymer cylinder has a diameter of 8mm and length of 10mm and made by cutting. The figure 2 shows the tested polymers in original form.

Figure 2. Original forms, colours and dimensions of the tested polymers and composites.

The cylindrical specimens are in counter formal connection with the steel plate. The components of composites are homogenously spread in the bulk of polymers.

The test results
I reported on the results of the examinations made on the higher load (150N) in detail in my earlier work already [Zsidai, Kalácska (2014)], I disregard this now because of this. I present the summary diagram in the interest of the better comparability in the (discussion) chapter 3.

These examinations represent our present work, where we measured the polymers on a lower load (50N), like this the effect of the changing load direct we may have analysed it. Let's see these measurements in the next. One typical test is shown in the figure 3-7 from the repeated (three times) investigations in cases of all polymers.
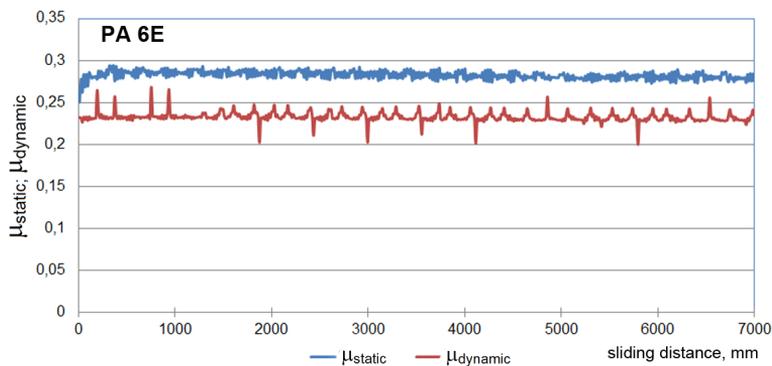

Figure 3. Static and dynamic friction coefficient of PA 6E
(sliding distance = 7m; load = 50 N; surface roughness R_z= 1,7μm)

The PA 6E started the tests silently, after it with slow strengthening his end I experienced medium (or big) noise. A measurement a mild vibration was sensible. A wear gap was not observable in one of the cases on the surface.
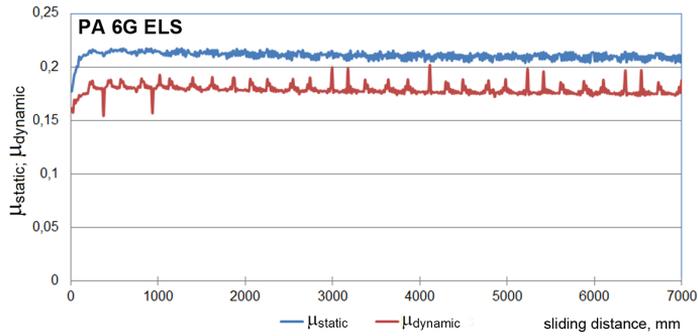
Figure 4. Static and dynamic friction coefficient of PA 6G ELS
(sliding distance = 7m; load = 50 N; surface roughness R_z = 1,7μm)
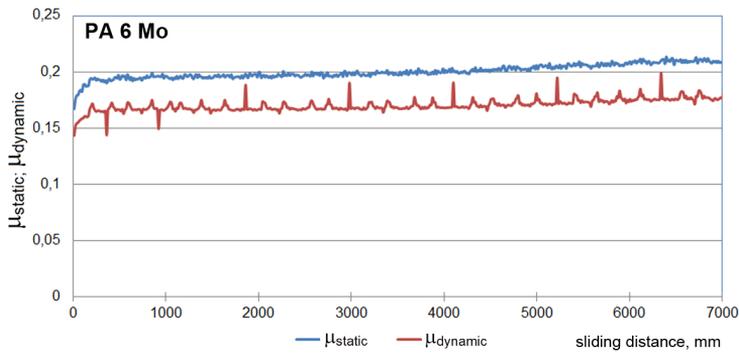
Figure 5. Static and dynamic friction coefficient of PA 6 Mo
(sliding distance = 7m; load = 50 N; surface roughness R_z = 1,7μm)
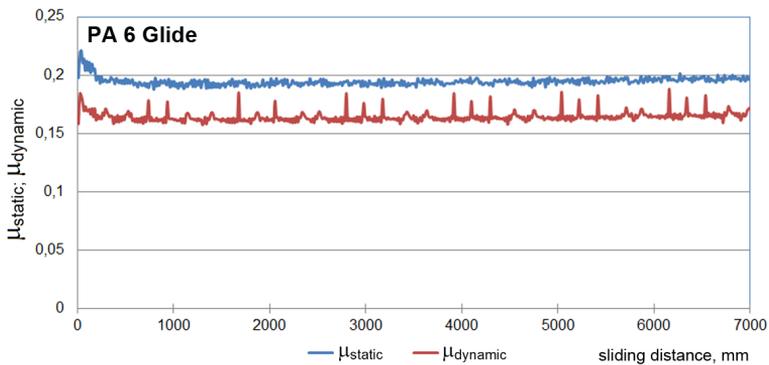
Figure 6. Static and dynamic friction coefficient of PA 6 Glide
(sliding distance = 7m; load = 50 N; surface roughness R_z = 1,7μm)

All of the examinations of the PA 6G ELS, PA 6 Mo and PA6 Glide were
quiet, a shake were free and a wear gap were not observable.
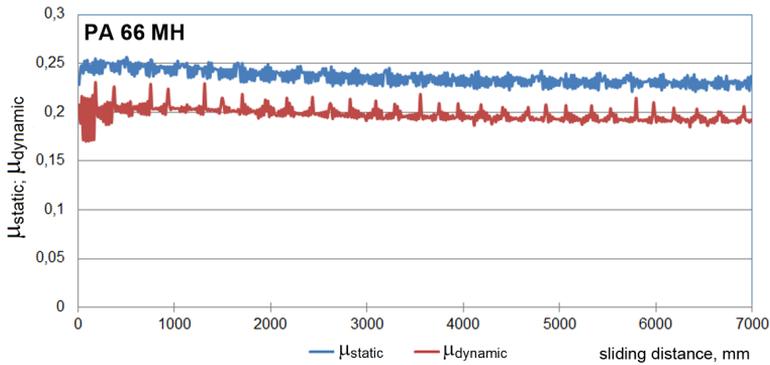
Figure 7. Static and dynamic friction coefficient of PA 66 MH
(sliding distance = 7m; load = 50 N; surface roughness R_z= 1,7μm)

During the examinations of the PA 66 MH, at the start period adhering a strong sound was a referrer can be experienced that later blunted one. Wear track was not possible observed.

3. Discussion

The dynamic friction coefficients are represented in Figure 8 and 9. For each material, the dark part of column refers to the regime value of dynamic friction coefficient and the lighter one refers to the maximum value of dynamic friction coefficient. All values are averaged from three test runs with identical parameters.

Let's see the figure 8, where the polymers were tested on higher load (150 N). Here are a similar friction coefficient (~0,18-0,21) in case of polyamides 6E, 6G ELS and 6MO. The lowest friction is present by polyamides 66 (PA66 MH). From the point of view of friction, PA6 GLIDE is more favourable than in case of other polyamides 6.
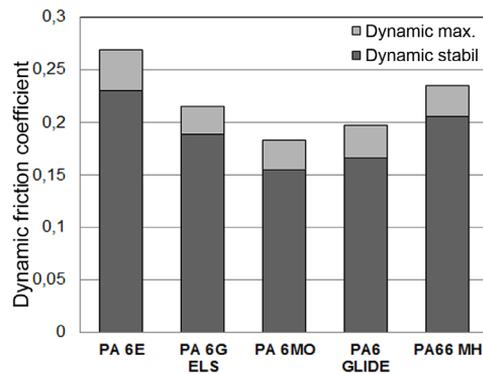

Figure 8. Dynamic friction coefficients of different PA composites
(sliding distance = 7m; load = 150 N; surface roughness R_z= 1,7μm)

The figure 9 shows other range between the same polymer composites with lower load (50 N). We can see a different friction towards the polymers. One of the lowest frictions is shown by PA6 GLIDE and one of the higher by PA6E, similar than it was in higher load category. However, there is just a little effect on the lower load on polyamides 6G ELS (and Pa6 GLIDE also). There are interesting results by PA6MO (lowest friction) and PA66MH (higher friction than in previous category).
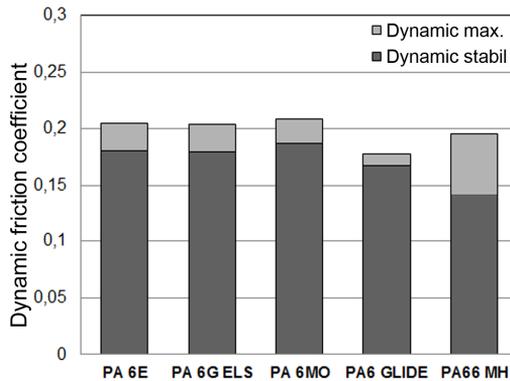

Figure 9. Dynamic friction coefficients of different PA composites
(sliding distance = 7m; load = 50 N; surface roughness R$_z$= 1,7μm)

Differences are visible on the figure 10 between the static and dynamic friction of the examinations published earlier (150 N load level).
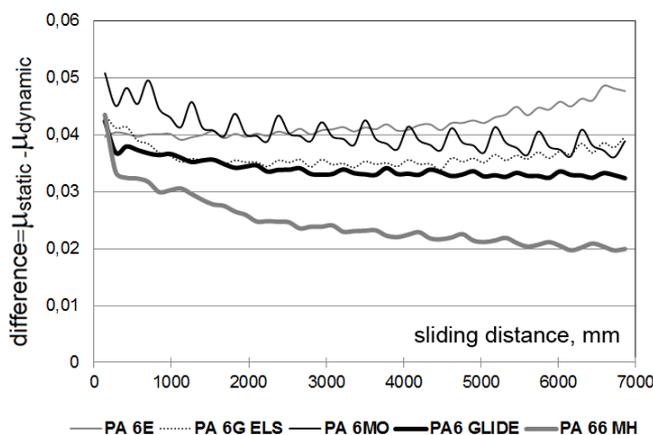

Figure 10. The difference between static and sliding friction for all tested
Polyamide with higher load
(sliding distance = 7m; load = 150 N; surface roughness R$_z$= 1,7μm)

138

During the examinations the following were observed:
- The creaking sound (with vibration) was getting stronger continually in the course of this PA 6E examination was observable. Polymer transfer layer and wear gaps were observable.
- The experiment showed a quiet, vibration-free running in case of the PA 6G ELS and PA 6MO.
- The initial strong noise weakens continuously until the end of the measurement in case of the PA66 MH.
- The differences between frictions (static and dynamic on 50N load level) which can be seen on the figure 11 are in good harmony with the single measurements (figures 3-7) as mentioned.
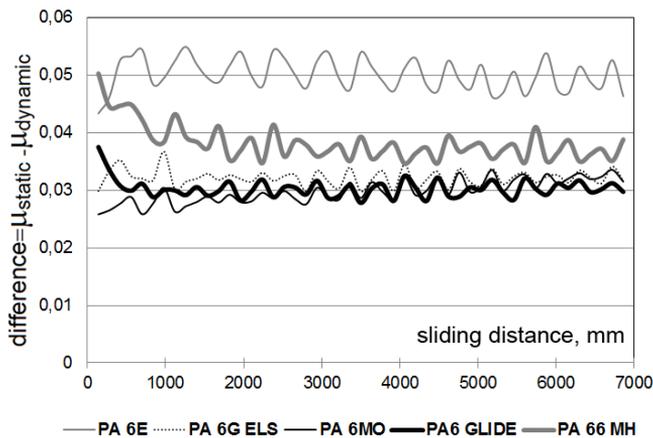

Figure 11. The difference between static and sliding friction for all tested Polyamide with lower load *(sliding distance = 7m; load = 50 N; surface roughness R_z= 1,7μm)*

During the examinations the following were observed:
- The highest difference belongs to the PA 6E curve. It correlates well with the continuous strong noise and vibrations.
- In the case of the PA 66 MH the initial friction noise was becoming blunt quickly. We can see it well on the figure, where the curve decreases step by step during the test.
- In case of the other polymers the tendencies and values are similar and the curves horizontal.

Conclusions

The reciprocating cylinder-on-plate test rig is not able to provide absolute data representative of actual applications. The tribological behaviour of different

polymers can be compared successfully and we can declare that most of their friction strongly depends on the load level.

The experimental friction data (figures 8 and 9) suggest the following conclusions:

- The higher load reduces the effect of the additive component significantly in case of the polyamide 6 base matrix. It is observable that the friction values on category of 150 N loads are identical. The PA66 differs from this tendency, but there the base material is not the same as PA6.
- The additive components receive an important role already on a lower load (50N), like the molybdenum disulphide is able to reduce the friction of PA6 MO.
- The load change has little effect on the friction of PA6 GLIDE and PA 6GELS. At the same time the lower elasticity modulus of PA66MH causes instability on the starting period of the friction on a lower load, the perceived halting friction noise (supposed stick-slip) supports this too.

We may consider the definition of the differences between the static and dynamic frictions and depicting it in a diagram (during the whole examination time) the most important results of our present work. We can call this difference the instability of friction. These diagrams are in good correlation with the friction noises and vibrations, experienced during the tribology tests.

In summary what can be established from the diagram of the friction instability (let's see the previous figures 10 and11):

- The PA6 GLIDE and the PA6G ELS each were observed along an identical straight and in a similar value on both load levels (similar as in the case of friction column diagram). This common character on lower load came true around a smaller value.
- The PA66 MH started with high friction instability, which decreased to the end of the test continuously, in case of both load levels (the initial strong frictional noise indicated this).
- The reference polymer PA6E indicated the worst instability in both cases, but in opposite with PA66 MH the increasing tendency is continuous during all tests.

It is clear from the results, that the difference between static and dynamic friction coefficient can characterize the stick-slip behaviour of polyamide composites. The results presented in the former tests show that we can create an index number to mark the stick-slip behaviours of the polymers, the role of our future work.

Acknowledgements

Special thanks go to QuattroPlast for the delivery of material specimens.

References

[1] Bruska Azhdar, Bengt Stenberg, Leif Kari (2006): Determination of dynamic and sliding friction, and observation of stick-slip phenomenon on compacted polymer powders during high-velocity compaction, Polymer Testing, Volume 25, Issue 8, December 2006, Pages 1069–1080)

[2] Evans, Dc; Senior, Gs (1982): Self-lubricating materials for plain-bearings, TRIBOLOGY INTERNATIONAL Volume: 15 Issue: 5 Pages: 243-248

[3] F. Van De Velde, P. De Baets, The friction and wear behaviour of polyamide 6 sliding against steel at low velocity under very high contact pressures, Wear 209 (1997) 106–114.

[4] Friedrich, K; Lu, Z; Hager, AM (1995): Recent advances in polymer composites' tribology ,WEAR Volume: 190 Issue: 2 Pages: 139-144

[5] G. Kalácska- L. Zsidai- M. Kozma- P. De Baets: Development of tribological test-rig for dynamic examination of plastic composites. Hungarian Agricultural Engineering. N.12/1999. Hungarian Academy of Sciences. p. 78-79.

[6] G. Kalácska, ed. (2007): Műszaki polimerek és kompozitok a gépészmérnöki gyakorlatban. 3C-Grafika Kft. p. 1-315. ISBN-10: 963-06-1566-5, ISBN 13: 978-963-06-1566-2

[7] G. Kalácska, et al., (1997): Műszaki műanyagok gépészeti alapjai (Mechanical Basics of Polymers), Minervasop Bt. Sopron,

[8] H. Uetz, J. Wiedemeyer, (1985): Tribologie der Polymere, Carl Hanser, Munich,

[9] J. Sukumaran, M. Ando, P. De Baets, V. Rodriguez, L. Szabadi, G. Kalacska, V. Paepegem (2012): Modelling gear contact with twin-disc setup, Tribology International 49 (2012) 1-7

[10] J.H. Byett, C. Allen (1992): Dry sliding wear behaviour of polyamide-66 and polycarbonate composites, Trib. Int. 25 (1992) 237, Pages: 237-246

[11] L. Zsidai, et al. (2002): The tribological behaviour of engineering plastics during sliding friction investigated with small-scale specimens. Wear, 253 673-688. p.

[12] L. Zsidai, G. Kalácska (2014): „Stick-slip" PA és PEEK kompozitok súrlódásánál, henger/sík modell vizsgálati rendszerben, Műanyag és Gumi 2014.51. Vol. 12.

[13] L. Zsidai, Z. Szakál (2013): Development of tribology model systems for research of PA6 and PEEK polymer composites, Mechanical Engineering Letters, Szent István University p.:130-139, HU ISSN 2060-3789

[14] L. Zsidai, Z. Szakál (2014) : Friction of PA6 and peek composites in the light of their surface characteristics Research & Development, Mechanical Engineering Letters, Szent István University 2014, p.:165-184, HU ISSN 2060-3789

[15] L. Zsidai, R. Keresztes, A. Eleőd (2015): A "stick-slip" jelentősége és tribológiai vizsgálatának lehetséges irányvonalai polimer gépelem alkalmazásokhoz, Polimerek P021 (in print)

[16] R. Keresztes, G. Kalácska (2010): Research of machining forces and technological features of cast PA6, POM C and UHMW-PE HD 1000. Sustainable Construction & Design. 2010. Vol.1. p. 136-144.

[17] Tanaka K. (1982): Transfer of semi-crystalline polymers sliding against a smooth steel surface WEAR   75

[18] Y. Yamaguchi (1990): Tribology of Plastic Materials, Tribology Series 16, Elsevier, Amsterdam DIN 50322, Kategorien der Verschleißpru¨ fung, Deutsche Norm 50322, Beuth Verlag, 1986.

[19] ENSINGER essentials. Technical know-how for plastic applications. www.plastic-metal.com

[20] www.quattroplast.hu/files/file/B_kategoria.pdf

In-situ surface monitoring technique for oil lubricated contact

Jacob SUKUMARAN[1], Maarten VANOVERBERGHE[1], Bavo DE MARE[1], Patric DANIEL NEIS[2] and Patrick DE BAETS[1]

[1]Laboratory Soete, Department of Mechanical Construction and Production, Ghent University

[2] Laboratory of Tribology, Universidade Federal do Rio Grande do Sul Porto Alegre, Brazil

Abstract

The present day techniques used in surface investigations of lubricated contacts are far from real contact condition. In fulfilling this need an *in-situ* system was developed for a twin-disc model. An optical system using telecentric lens was used in acquiring images of moving contact surface. In validating the monitoring system two tests with line and elliptical contact were performed. Images of contact surface at specific cycles clearly shows the progressive surface damage. It can be concluded that the developed *in-situ* system and the configuration is effective in observing surface change at micron scale in oil lubricated conditions.

Keywords

in-situ monitoring, wear, lubricated contact

1. Introduction

In traditional tribological practice post-mortem analysis of contact surface is often used for understanding the wear process. However, the surface may have significantly changed in the course of interaction. Thus the traditional approach does not allow us to precisely identify the dominating wear mechanism contributing to the wear process. Besides, in the conventional surface inspection only a small region of interest (ROI) is considered for investigation and may not fully represent condition of the whole surface. Phenomenon occurring during the test can be related with other signals such as friction, temperature etc., which may enable us to globally understand the wear process. Wear by itself is the progressive loss of material and it is in the best interest of scientist to understand the progression from the modified surface using *in-situ* vision system. However, due to poor access to the contact surface, expensive and complicated instrumentation hinders the *in-situ* monitoring of the tribological contact. Attempts were made to monitor the contact surface, however in most cases the

focus was on dry contacts see, (Glaeser et al 1981, Quintelier 2004). In a dry contact condition optical systems and scanning electron microscopes are used to trace the progressive loss of material. Beside the two dimensional image characteristics, the depth characteristics was acquired in real-time by means of interferometry see, (Tasan el al 2005). Most systems has its own limitation in terms of speed, depth of focus and processing capabilities.

The complexity in *in-situ* monitoring of contact surface increases further when a medium such as oil, water or emulsion is introduced in the contact. Attempts were made to study properties of lubricating film, however the contact conditions are far from real application where glass is used as a counterface material see, (Åström et al 1991). Conditions close to real applications was studied by (Kano et al 2005) where steel on steel under oil lubricated condition was studied using *in-situ* monitoring system. In their research a laser strobe system was used and moreover the lubrication system was introduced initially by coating the contact surface with lubricants. Their research also mainly focused on pure sliding condition. Besides pure sliding there are numerous applications where rolling contact condition are evidenced such as roller bearings, gears, cams etc. (Mens et al (1991); Xu et al (2014)) which may need advanced *in-situ* monitoring system. In contributing to such applications we have developed an *in-situ* monitoring system for rolling-sliding contacts under lubricated condition. The system continuously monitors moving contact surface using optical imaging technique. Tests were performed for adapting the contact geometry and also validating the capability of the *in-situ* monitoring system.

2. State of the art

in-situ monitoring is present in different areas of tribology such as tool wear (macro) and roughness change (micro) monitoring see, (Hoy et al (1991);Fadare and Oni (2009). The scale of investigation is primarily decided from the application area and also based on the interest of particular research topic. Techniques for imaging in liquid medium such as laser triangulation which is used in macro scale investigations (Roman et al 2010) can be adapted to the present tribological system but at a high cost. Considering the cost an optical system is much appreciated however, careful consideration is to be given for the selection of lens where limitations from depth of focus plays an important role. In the present research on developing an *in-situ* monitoring system, a methodical approach was followed where the system is divided into two modules which are (1) tribological system, and (2) imaging system.

Tribological System
Tribo-system contains two main parts which are the contacting bodies tribo-element 1 and 2 representing the two disc materials in a twin disc configuration see, (Sukumaran et al 2014). The tribological system used in the present research is a modification of an existing system see, (Sukumaran et al 2012) where forced

rolling-sliding is introduced by mechanical coupling of both the discs. However, in the present system free rolling of driven disc is implemented and the driver disc is coupled to an electric motor. In the modified system the rolling-sliding ratio is estimated from an existing relationship where difference in the contact velocity between two non-conformal contacts results in the rolling-sliding ratio (Schipper 1988). The expression for calculating the rolling-sliding ratio is given in equation 1.

$$Slip\ ratio\ s\,[\%] = \frac{(v_1 - v_2)}{(v_1 + v_2)} \times 200\% \qquad (1)$$

For estimatisng the rolling-sliding ratio, the twin-disc configuration is instrumented with hall-effect sensors to measure the rotational speed for both the driven and the driver discs. A schematic of the twin-disc is shown in *Figure 1*. A torque sensor (max 10 N-m) is coupled to the driver shaft where the friction torque from the bearings are estimated in a free run without contact and subtracted from the friction torque at load. In the event of wear the self-aligning bearing aids in maintaining the continuous contact and also facilitates the measurement of diametric loss from its displacement. The macro geometrical changes due to wear is monitored using a displacement transducer where the signals from the diametric change is studied online. All measurements are recorded online using NI 6036E DAQ (National instruments BNC 2100) in a LabVIEW platform. The data acquisition is coupled to the imaging system so that a time trigger initiates to acquire high frequency data for two revolutions. Beside data acquisition LabVIEW is also used to control the speed and to initialize the timed trigger.
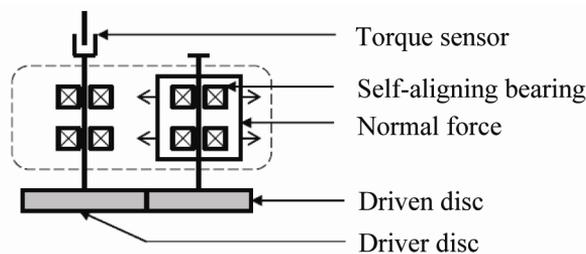

*Figure 1*. Schematic of the twin-disc configuration.

The tribo-contact is enclosed in an aluminum chamber so that the interfacial element (oil/water/emulsion) can be introduced in the contact. Separate circulation circuits are constructed for emulsion and oil. A closed loop system is used where the fluid is recirculated. In the course of recirculation it is evident that the generated wear particle may come in contact and thus changing the tribological nature. Hence to avoid the re-entry of wear particle to the contact,

powerful magnets are used at the exit of the lubrication circuit where the generated particles are extracted from the fluid system.

Imaging System

The imaging system is optical based system which contains three main components (i) camera (ii) lens and (iii) illumination. To have a better understanding of the phenomena it is necessary to monitor the contact surface with clear images from the beginning to the end of the test. Poor selection of lens may limit the test duration/sliding distance where investigations beyond the depth of focus is futile considering the blurring effect from defocusing. The selection of the camera sensor was carefully done using the EMVA1288 camera standard. Quantum efficiency, sensitivity, noise, saturation capacity and dynamic range were considered for sensor selection. Since the images will be acquired online a CMOS (Complementary metal–oxide–semiconductor) sensor dedicated to high speed capabilities was chosen. A 2/3" CMOSIS 2000 which has a resolution of 2048 x 1088 pixels, a field of view and a depth of view of 11 mm x 6 mm and 1.2 mm respectively was chosen. In regards to the lens a telecentric lens with a working distance of 65mm is found to be appropriate. The larger working distance enables us to monitor complex surfaces without any mechanical interference of moving parts. Moreover, the perspective error can be largely eliminated by using a telecentric lens. Thus the wear mechanisms and surface damage can be identified precisely from quantitative microscopy. A bright field near vertical illumination was selected based on the tribo-contact. High intensity LEDs were used to build the near vertical illumination where a pattern confirming to the uniform distribution was used in the arrangement of LEDs. *Figure 2* shows the twin-disc arrangement and the corresponding instrumentation. The imaging is performed using LabVIEW 13 and the NI vision assistant.
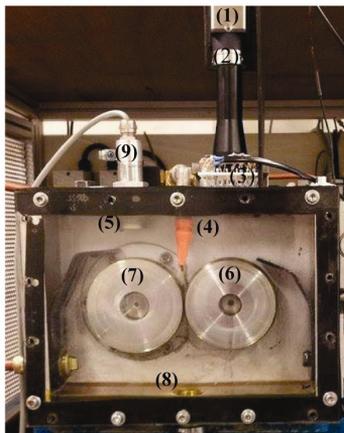
1 – CMOS sensor
2 – Telecentric lense
3 – Near vertical illumination
4 – Lubricant feed to contact surface
5 – Temperature sensor
6 – Driven disc
7 – Driver disc
8 – Magnet
9 – Temperature sensor

Figure 2. Twin-disc arrangement with in-situ monitoring system
(lubricated environment).

3. Materials and methods

Tests performed in the twin-disc configuration is aimed at studying components such as gears and rollers which are used in rolling tribological contacts. A rolling element frequently found in engineering application is the gears which operates in both pure rolling and partial sliding condition. The operating parameters are carefully chosen to experimentally simulate the rolling contact of the gears. Materials of choice is also selected based on the gear contact where both the driven and the driver disc are made from 42CrMo4 alloy steel. Two different configuration from the view point of contact model was used to validate the performance of the *in-situ* monitoring system. Hertzian contact pressure ranging from 0.5 to 2 GPa was used. Tests were performed in a lubricated environment where continuous flow of lubricant to the contact surface is maintained. OMALA S2 G 320 industrial gear oil which is typical for gear box lubrication is used as a lubricant in the present work. *Table 1* shows the operating parameters and the contact condition used in the testing. Two long duration tests were performed with a line and elliptical contact. Increasing the contact pressure is achieved by means of a curved surface.

Table 1. Contact conditions used in the testing

	Rotational speed (rpm)	Contact width	Max contact pressure (MPa)	Number of Cycles	Radius of curvature (mm)
Test 1	300	Line (6mm)	298	1082 400	0
Test 2	410	Elliptical	2070	2765200	12

4. Results and discussion

The online images from both tests are thoroughly studied for understanding the capability of the *in-situ* vision system. Two tests with line (Test 1) and elliptical (Test 2) contact were performed. Since the images were electronically triggered using the hall-effect sensor, the progression in the damage can be traced. Images were acquired for every 20 minutes time interval and forced triggering was also made. Sample images from Test 1 is shown in *Figure 3* where images of same ROI from two different cycles (approximately with a difference of 153000 cycles) are clearly seen. The region encircled shows the same surface defect in both the images and hence images are from the same region of interest (ROI). Hence it is evident that the system is capable of tracking the progressive damage of the surface. The effects of illumination is also clearly seen as rectangular white segment pointed out in the image. In the image acquisition sequence the rotational speed is reduced to a minimum of 50 rpm, subsequently the continuous lighting is initiated further to which the trigger is made for activating the camera. A frame rate of 20 fps was used for imaging and the sequence is

followed to avoid motion blur. However, this also leads to condition where the slow speed retains the oil on the contact surface (see Figure 4). A thin layer of oil still present in the contact surface can be identified from yellow coloration. Also it is evident that there is a delay in the trigger while comparing Figure 3 (a and b).
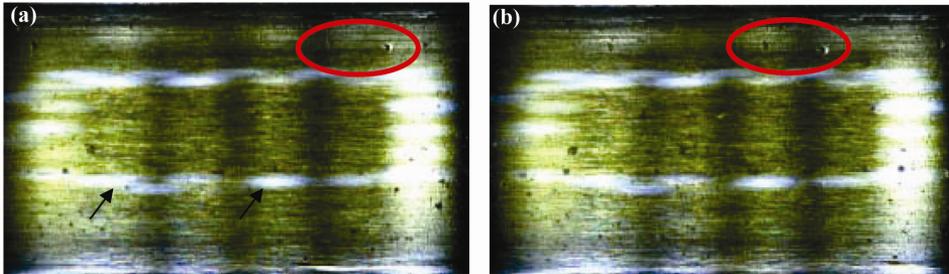

Figure 3. Online image of driven disc contact surface (Test 1) (a) 55,000 (b) 2008000 (FOV: 6 mm x 11 mm).

By introducing a curvature on the contact surface the stagnation of oil removed. Hence, in the driven disc a curvature (radius 12 mm) perpendicular to the disc axis was made on the contact surface. The imaging from the worn contact surface shows that there is a significant amount of advantage in obtaining an oil free surface. In case of loading the contact pressure will be significantly increased for the same load and thereby accelerating the condition. Development of abrasion scars (marked with arrow) over a period of time is clearly seen from the *Figure 4*.
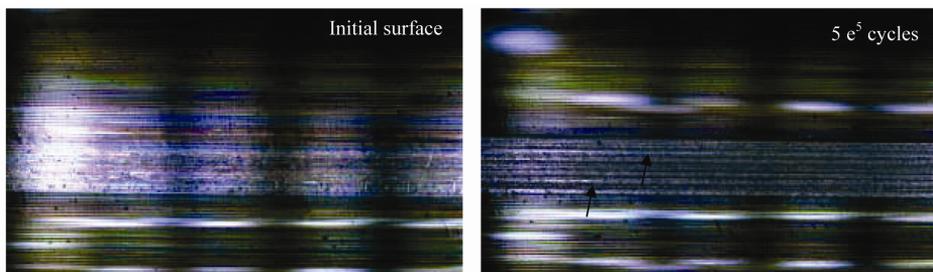

Figure 4. Contact surface of driven disc during the initial period of testing and after 500000 (FOV: 6 mm x 10 mm).

Images from the same location were tracked and the progressive loss was clearly monitored (*Figure 5*). Sample images as seen in *Figure 5* are taken during different stages of testing shows that the initially found machine marks are removed by partial abrasion. Images from the same ROI at selected cycle

148

shows that the surface has changed significantly. Nevertheless, the conventional tribological analysis merely considers the images from the post-mortem analysis to understand the wear mechanisms. Hence this test equipment stands effective in tracking down the timely change in wear mechanism as a function of sliding distance under lubricated environment. This image data can be quantified for the change in appearance and thereby compared with other sensor data produced from the tribological testing such as temperature, diametric loss, friction etc.
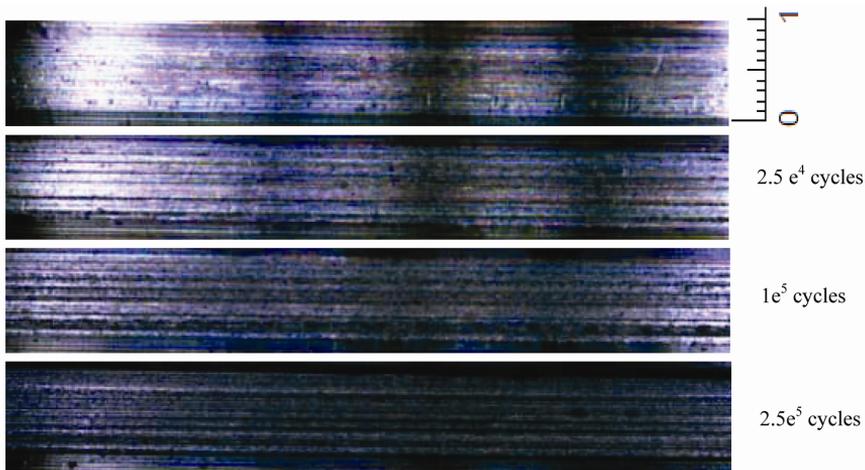

*Figure 5.* Driven disc initial surface for damage evolution. (FOV: 6 mm x 10 mm).
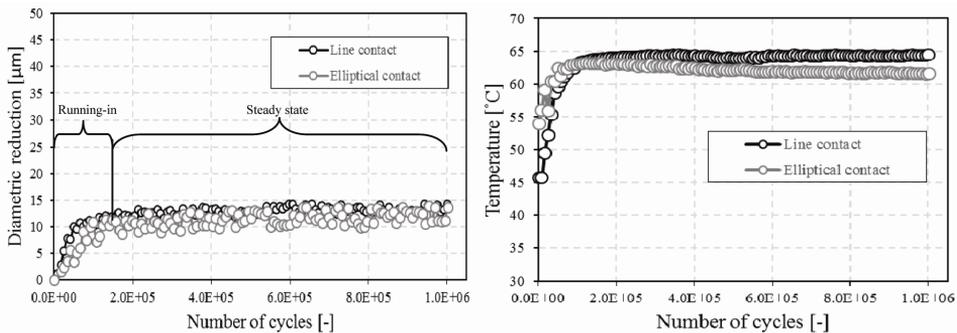
Figure 6. (a) Diametric loss (b) Temperature profile.

Besides the image data, the temperature and the diametric change were also acquired at a sampling rate of 720 Hz. *Figure 6* shows the diametric change and the temperature trend for 10 e^5 cycles. The sampling interval followed the same as that of the image acquisition. It is evident from *Figure 6*a that two regions, running-in and steady state are present for both contact condition. Although the contact pressure was increased by ten folds the wear trend followed the same.

The limited wear in test 2 when compared with test 1 may be associated to the difference in lubricating regime. However, the lubricating regime particularly in this configuration is to be studied in depth. Moreover, the temperature as seen from *Figure 6*b also follows a similar pattern for both line and elliptical contact. However this diametric change does not includes the influence of thermal expansion and hence its response on diametric loss should be studied further with varying temperature.

Conclusions

The present work dealt with developing a standalone test-rig for studying the progressive loss of material due to wear of lubricated contacts under rolling-sliding condition. Advantage in selecting the twin-disc system was evidenced in terms of visible contact surface after each cycle for imaging. The optical system, camera and illumination are carefully selected based on operating conditions (presence of lubricant and speed) and the scale of investigation. Test results concludes that the progressive damage can be monitored efficiently within the ROI. Moreover, the curvature introduced in the contact surface stays effective in removing oil from the contact surface to have a better view. The newly developed *in-situ* system stays effective for oil lubricated environment and represents the real condition.

Acknowledgements

References

[1] Glaeser, W.A. (1981), Wear experiments in the scanning electron microscope. Wear,. 73(2): p. 371-386.
[2] Quintelier, J. (2007), Online wear monitoring of polymer matrix composites with advanced measurement techniques, PhD dissertation, Ghent University.
[3] Tasan, Y.C., de Rooij, M.B., and Schipper, D. J. (2005), Measurement of wear on asperity level using image-processing techniques. Wear, 258(1-4): p. 83-91.
[4] Åström, H., O. Isaksson, and Höglund, E.. (1991), Video recordings of an EHD point contact lubricated with grease. Tribology International, 24(3): p. 179-184.

[5] Kano, S. Homma. H, Sasaki. S, and Shimura, H. (2008), In situ monitoring of friction surfaces and their sequence pattern analysis. Philos Trans A Math Phys Eng Sci, 366(1865): p. 665-71.

[6] Mens, J.W.M., Boose, C. A., and de Gee, A.W.J. (1991), A rolling ball test for establishing contact fatique behaviour of bulk materials, surface layers and coatings. Tribology International, 24(6): p. 351-356.

[7] Xu, L., Wei. S, Xing. J, and Long, R. (2014), Effects of carbon content and sliding ratio on wear behavior of high-vanadium high-speed steel (HVHSS) under high-stress rolling–sliding contact. Tribology International, 70(0): p. 34-41.

[8] Hoy, D.E.P. and Yu, F. (1991), Surface quality assessment using computer vision methods. Journal of Materials Processing Technology, 28(1–2): p. 265-274.

[9] Fadare, D. and Oni, A. (2009), Development and application of a machine vision system for measurement of tool wear. Journal of Engineering and Applied Sciences, 4: p. 30-37.

[10] Roman, C., Inglis. G, and Rutter, J., (2010). . Application of structured light imaging for high resolution mapping of underwater archaeological sites. OCEANSIEEE-Sydney. IEEE.

[11] Sukumaran, J., (2014) Vision assisted tribography of rolling-sliding contact of polymer-steel pairs. 2014, Ghent University.

[12] Sukumaran, J., Ando, M., De Baets, P., Rodriguez, V., Szabadi, L., Kalacska, G., Paepegem, V., . (2012), Modelling gear contact with twin-disc setup. Tribology International, 49(0): p. 1-7.

[13] Schipper, D.J. (1988), Transition in the lubrication of concentrated contacts, PhD Dissertation, Universiteit Twente